

COMPUTER SIMULATION OF HYDROGEN ADSORPTION IN METAL ORGANIC FRAMEWORKS

Anastasios I. Skoulidas(1), Giovanni Garberoglio(1), and J. Karl Johnson(1,2)

(1) National Energy and Technology Laboratory, US Department of Energy, Pittsburgh, PA 15236

(2) Department of Chemical and Petroleum Engineering, University of Pittsburgh, Pittsburgh, PA 15261

Introduction

The target set by the Department of Energy for on-board hydrogen storage for automotive applications is about 7 percent by weight based on the of the total mass of the storage system.

The existing hydrogen powered vehicles rely on high pressure vessels (~70 MPa) or cryogenic liquid storage of hydrogen. In order to avoid the use of such high pressures or cryogenic equipment other alternatives are being studied. Two active areas of research are metal hydrides, in which the hydrogen is stored and retrieved using chemical reactions, and physisorption on microporous materials, such as carbon nanotubes.

Metal Organic Frameworks (MOF) have recently received much attention as possible hydrogen sorbents(1). These structures are composed of metallic cluster units, connected by organic linkers; they can be easily synthesized, are comparatively light and durable, and present large pores, making them an interesting candidate for the storage of hydrogen (see **Figure 1** for a picture of such a structure).

Given the large variety in which these materials can be produced, being able to estimate their ability of store hydrogen using computer simulation would allow one to tailor them to the best extent possible.

In this work we present computer simulation results for the adsorption isotherms of hydrogen at 77 K and 298 K in a select number of MOF materials. We validate our model by comparing our results to the available experimental isotherms, and discuss the origin of some of the discrepancies that we have observed; we further present our prediction for the adsorption of hydrogen in new materials of the same class.

Since computer simulations allow access to the microscopic details of the adsorption mechanism, we identify the adsorption sites of hydrogen in MOFs and discuss possible ways to improve their hydrogen storage capability.

Methods

We have simulated the adsorption isotherms using the Grand Canonical Monte Carlo technique. We describe the MOF framework as a rigid structure, which has been obtained by X-ray scattering. The solid-fluid potential energy has been evaluated using the UFF(2) force field that gives Lennard-Jones parameters for almost all materials in the periodic table. We have used the spherical Buch potential for hydrogen ($\epsilon/k_B = 34.7$ K, $\sigma = 2.96$ Å) and the Lorentz-Berthelot mixing rules to calculate the solid-fluid potential. The ideal gas formula was used to relate chemical potential and pressure in our simulations.

Low temperature simulations. Since many of the results for adsorption are available at 77 K we have taken into account quantum mechanical diffraction effects using the Path Integral method(3). In this formulation a quantum particle is approximated by substituting it with a ring polymer, whose beads interact via a harmonic potential that depends on the Planck constant as well as the temperature and the mass of the molecule. The exact quantum mechanical result is recovered as the number of beads tends to infinity. In our simulations the asymptotic value was reached using 20 beads.

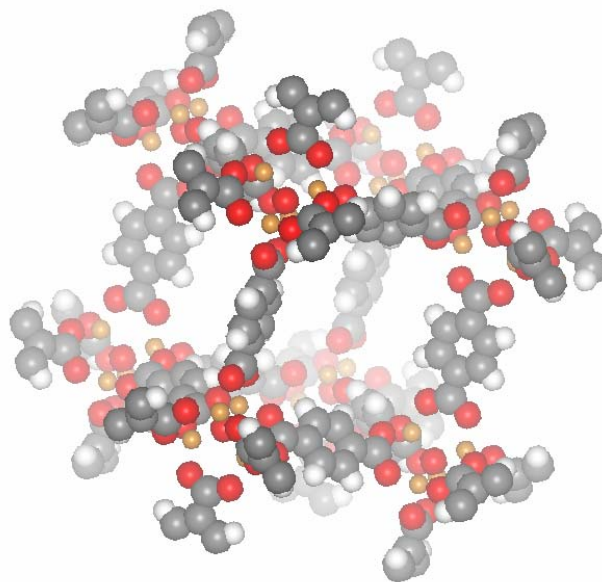


Figure 1. The structure of MOF-5. The metallic clusters are composed by Zn and O and the resulting unit cell has a cubic shape.

Results and discussion

We show in **Figure 2** the comparison between the experimental results by Rowsell et al.(4) and our computer simulation data for hydrogen at 77 K in MOF-5 (also called IRMOF-1), whose structure is shown in **Figure 1**. The agreement between the model and the experiment is excellent, especially when quantum corrections are taken into account. The classical simulation results in an overestimation of the adsorption by almost 10% at the highest experimental pressure around 1 bar.

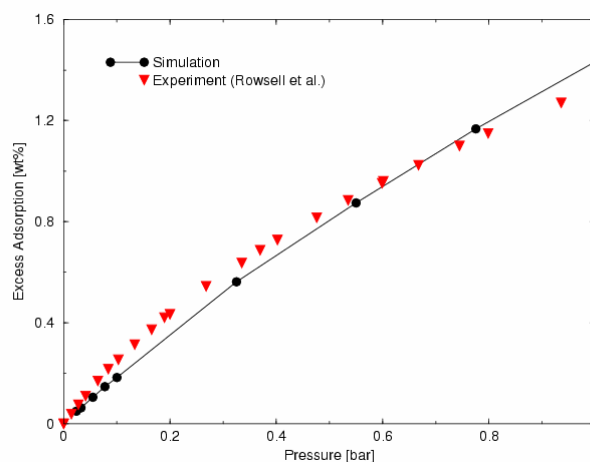


Figure 2. The isotherm of adsorption for hydrogen in MOF-5 at 77 K. Black circles: path integral Monte Carlo simulation, red triangles: experimental result by Rowsell et al.(4).

We have also compared our simulations with the results published by Rowsell et al.(4) regarding another material, called

IRMOF-8, and found a good agreement, although not as good as that shown in **Figure 2**. The computer simulation is within 5% of the experimental values around 1 bar, but underestimates the adsorption by a factor of almost two at intermediate pressures.

A different picture emerges from the comparison between simulations and experiments on MOF-5 at room temperature. We show the results we have obtained in **Figure 3** and compare them with the experiments performed by Rosi et al.(1). It is apparent that the computer simulation results underestimate the experimental data by almost a factor of three. The origin of this discrepancy is not clear, but in view of the excellent agreement obtained at cryogenic temperature we think that it is due to errors in the force field, but probably one or more other approximations. It is well known that the MOF structure is not rigid as we assume in our model and the enhancement in the adsorption may be due to a deformation of the structure.

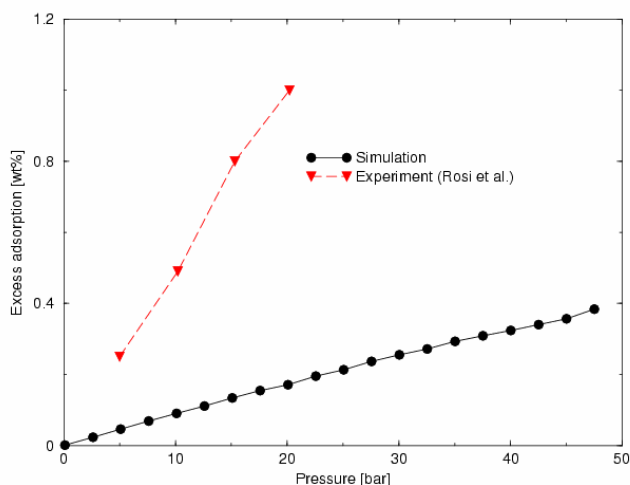


Figure 3. The adsorption isotherm of hydrogen on MOF-5 at 298 K. Black circles: our computer simulations; red triangles: the experimental result by Rosi et al.(1).

We present our prediction for the excess adsorption in various MOFs at room temperature in **Figure 4**. In light of the results shown in **Figure 3**, we might be underestimating the actual amount of hydrogen adsorbed. However, even taking into account a factor of three increase in the capacity over our predictions, one would fall short of the target of 7%. The best adsorbent within the ones we have investigated is IRMOF-14, which shows an excess adsorption of 0.6% at the pressure of 100 bar.

The reason for the poor adsorption properties of these materials lies in the fact that the most effective adsorption sites are not along the organic linker but rather in the proximity of the metallic cluster. An analysis of the potential energy surface shows that the absolute minimum of the potential energy inside the unit cell is near the corner occupied by the metals. The potential energy along the organic linker is separated from this minimum by at least 400 K, resulting in almost no occupation of these sites at room temperature.

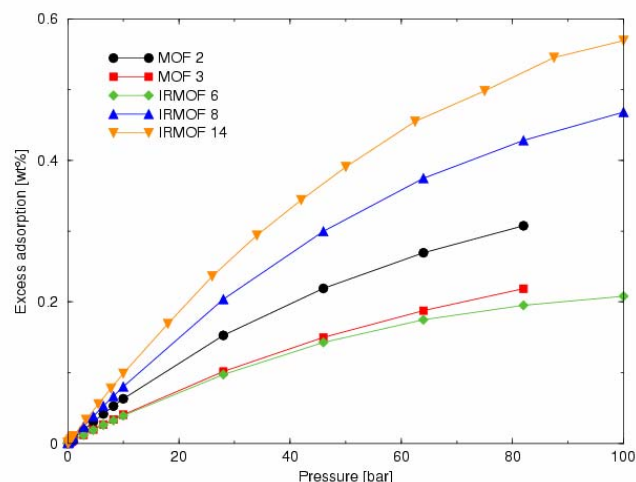


Figure 4. The computer simulation results for a series of MOFs at 298K.

Conclusions

We have tested the ability of the UFF force field to predict the adsorption isotherms of hydrogen in Metal Organic Frameworks. Assuming a rigid structure and a spherically symmetric model for the hydrogen molecule, we obtain very good agreement between the simulation and the available experiments at cryogenic temperatures and pressures less than 1 bar.

The agreement between simulation and experiments at room temperature is not as satisfactory; the simulations underestimate the amount of hydrogen adsorbed by almost a factor of three. We tentatively assign the origin of this discrepancy to the fact that we have assumed a rigid structure for the MOF.

Despite these shortcomings, we have shown our results for the adsorption at room temperature in a variety of MOFs, and shown that they do not meet the DOE requirements. Even if one supposes that the actual amount adsorbed is a factor of three higher than our prediction, as suggested by the MOF-5 results, the required goal of 7% would not be achieved.

The origin of this apparent poor performance of the MOFs with respect to the adsorption of hydrogen is attributed to the fact that the organic linkers do not play almost any role in the adsorption, at least in the materials we have taken into consideration.

References

- (1) Rosi, N.L.; Eckert, J.; Eddaoudi, M.; Vodak, D.T.; Kim, J.; O'Keeffe, M.; and Yaghi, O.M. *Science*, **2003**, *300*, 1127.
- (2) Rappé, A.K.; Casewit, C.J.; Colwell, K.S.; Goddard III, W.A.; Skiff W.M. *J. Am. Chem. Soc.* **1992**, *114*, 10024
- (3) Wang, Q.; Johnson, J.K.; Broughton, J.Q. *J. Chem. Phys.* **1997**, *108*, 5117
- (4) Rowsell, J.L.; Millward, A.R.; Park, K.S.; Yaghi, O.M. *J. Am. Chem. Soc.* **2004**, *126*, 5666

FIRST PRINCIPLES APPROACHES TO PREDICTING HYDROGEN PERMEATION THROUGH METAL ALLOY MEMBRANES

David S. Sholl^{1,2}, Preeti Kamakoti^{1,2}, and Sudhakar Alapati¹

¹Department of Chemical Engineering, Carnegie Mellon University, Pittsburgh, PA 15213

²National Energy Technology Laboratory, Pittsburgh, PA 15236

Introduction

Separation of hydrogen from mixed gas streams is one of the key steps required in the large-scale use of hydrogen as a fuel or a chemical feedstock. Dense metal membranes are a well-known technology for accomplishing this task. Practical metal membranes must simultaneously achieve multiple performance objectives, including delivering high hydrogen flux, being resistant to poisoning by impurities in the feed stream, and being robust to thermal cycling and long term use. The use of metal alloys is an obvious route to improve upon the well-known properties of pure metals as membranes. Many experimental studies of metal alloys as potential membranes have been performed. A significant difficulty with exploring the range of alloys available as potential membranes is that experimental screening of membranes is time-consuming and expensive. The aim of our work has been to develop theoretical tools that can predict the permeance of hydrogen through metal alloy membranes with quantitative accuracy in ways that will complement experimental studies in this area. Our work to date has been presented in Refs. [1] and [2]. Recently we have made comparisons between the predictions of our theoretical methods with extensive experimental measurements of PdCu alloy membranes. These results will be presented in a forthcoming paper [3].

Methods

We have developed a model that is appropriate for metal films that are sufficiently thick that resistance to transport of hydrogen through the film is dominated by intracrystalline resistance. In this case, the permeance of hydrogen through the membrane can be written as a product of the hydrogen solubility and hydrogen diffusivity. We further consider physical examples where the hydrogen concentration in the alloy is dilute, an approximation that is appropriate for separations performed at elevated temperatures and moderate pressures. In this case, the solubility of hydrogen in the alloy is described simply by Sievert's constant.

To predict the properties of interstitial hydrogen in metal alloys we have used plane wave Density Functional Theory (DFT) within the Generalized Gradient Approximation (GGA) [1,2]. For ordered alloys such as bcc PdCu, we used ordered crystal structures with supercells containing 20-30 metal atoms and a single H atom. For disordered alloys such as the fcc PdCu alloys, we used a supercell of 20-30 atoms with a substitutionally random distribution of the metal atoms within the supercell. This approach is sufficient to create examples of the many distinct types of interstitial sites that can exist in these disordered materials.

Hydrogen solubilities are predicted by first computing the binding energy of H in many distinct binding sites of representative alloys with GGA-DFT [1]. Our calculations include local lattice relaxation due to the presence of interstitial H and also incorporate zero point energy effects within the harmonic approximation [1]. Once these binding energies are computed, we use them to relate the binding energy of each site to the local alloy composition (nearest neighbors and next nearest neighbors) using a simple expression that can subsequently be used to predict binding energies in a site of any type for any alloy composition [3]. These binding energies can then

be used in a statistical mechanical description to predict the Sievert's constant for hydrogen as a function of alloy composition and temperature. Comparisons of the predictions of this method with experimental data for hydrogen solubility in fcc PdCu alloys indicates that our approach accurately predicts the variation in solubility in this material as a function of temperature and alloy composition.

Hydrogen diffusivities are predicted by first performing multiple GGA-DFT calculations to identify transition states for local hops of interstitial H between adjacent binding sites [1,2]. In disordered or partially ordered materials, this information must be extended to describe a wide range of possible transitions before macroscopic diffusion can be described. This task is accomplished in a similar way to our predictions of solubility: a model is parameterized from our DFT calculations that predicts the diffusion activation energy as a function of the local alloy composition [2]. Once this model is available, Kinetic Monte Carlo simulations are used to determine the net diffusivity that arise from the hopping of isolated H atoms through large numbers of interstitial sites. In these simulations, the hopping rates between adjacent interstitial sites were computed using a version of quantum correct transition state theory that incorporates zero point effects at the level of the harmonic approximation.

We have used the approach above to predict the diffusivity of H in both bcc PdCu alloys and in fcc PdCu alloys [2]. Diffusion in the bcc alloys is much faster than in the fcc alloys [1], and is found to depend only weakly on the alloy composition in the range of compositions where the bcc alloy can exist. Diffusion in the disordered fcc alloy, in contrast, is a strong function of the alloy composition. As the Cu content of the fcc alloy is increased, H diffusion slows down significantly. At 500 K, for example, the diffusivity of H in the fcc alloy with 50 at.% Cu is more than two orders of magnitude slower than diffusion in pure Pd at the same temperature. The effective activation energy of net diffusion in the fcc alloy also increases as the Cu content of the alloy is increased.

One advantage of the DFT-based lattice model we have developed for H diffusion in fcc PdCu alloys is that we can study the effect of local ordering in a simple way. We have performed Kinetic Monte Carlo simulations of H diffusion in a range of alloy structures by holding the alloy composition fixed and varying the short range order as characterized by the nearest-neighbor Warren-Cowley parameter [2]. Over the range of the Warren-Cowley parameter that is typically observed for disordered binary alloys, the observed diffusion rates are only weakly dependent on short range order [2]. This observation indicates that short-range order is likely to not be an important factor in the overall performance of PdCu alloys in practical settings.

The methods described above for predicting the Sievert's constant and diffusivity of interstitial H in PdCu alloys allow us to predict the net permeance of hydrogen through PdCu alloys under practical conditions. An important observation here is that this prediction does not rely on any experimental input apart from knowledge of the crystal structure of the alloy of interest. We have compared our predicted permeance with extensive experiments performed by thick PdCu foils at elevated temperatures and H₂ pressures from 1-25 atm. These comparisons will be presented in detail in a forthcoming publication [3].

Current Work

Our work has demonstrated that a first-principles based approach can be a useful complement to experimental studies of metal alloys as potential hydrogen separation membranes. Our current work is focused on two aspects of this general problem. First, we are using our methods to screen potential ternary alloys that

contain Pd and Cu. The intent of this screening effort is to provide information on what metal components can be added to PdCu alloys that would potentially increase the net hydrogen flux through a membrane by either increasing hydrogen solubility or hydrogen diffusivity (or, most preferably, both). A second effort is aimed at extending our first-principles based approach to describe the diffusion of hydrogen between surface and sub-surface sites at the interfaces of metal alloy membranes. For the ultra-thin film films that are most desirable in practical devices, the rates of these interfacial processes may have an appreciable impact on the overall hydrogen permeance. Understanding the transition between bulk-controlled and interface-controlled diffusion is challenging experimentally, so the use of quantitative modeling methods should yield useful insight into the significance of this transition for practical devices.

Acknowledgement. Work at CMU was partially supported by the ACS-PRF and the Department of Energy University Coal Research Program.

References

- (1) Kamakoti, P.; Sholl, D. S., *J. Membrane Sci* **225** (2003) 145-154
- (2) Kamakoti, P.; Sholl, D. S., *Phys. Rev. B*, in press
- (3) Kamakoti, P.; Morreale, B.; Ciocco, M.; Howard, B.; Killmeyer, R.; Cugini, A.; Sholl, D. S., in preparation.

MECHANISMS FOR HYDROGEN DESORPTION IN SODIUM-ALANATE

C. Moysés Araújo¹, Sa Li², R. Ahuja¹, and P. Jena²

¹Department of Physics, University of Uppsala, Box 530, SE-751 21, Uppsala, Sweden.

²Department of Physics, Virginia Commonwealth University, Richmond, VA 23284.

Introduction

The growing worldwide demand for energy, the limited amount of fossil fuels, and their adverse effect on the environment have made it necessary to search for alternative energy sources that are renewable, abundant, secure, environment friendly, and cost effective [1]. One of the alternate energy resources that are currently being pursued involves hydrogen [2-7]. Although hydrogen is the most abundant element on earth, exhibits the highest heating value per mass of chemical fuels, and is pollution free as water is the only by-product during combustion, there are numerous hurdles to overcome before hydrogen can be used to address the energy needs of the future. These include problems associated with its production, distribution, storage, and use in fuel cells. Among these, hydrogen storage is considered to be the biggest challenge in a new hydrogen economy [8] since the storage medium must meet the requirements of high gravimetric (9 wt % hydrogen) and volumetric density, fast kinetics and favorable thermodynamics.

The current methods for storing hydrogen in the gaseous form under high pressure or in the liquid form in cryogenic tanks are problematic. The solid state storage of hydrogen is regarded as the best choice. Unfortunately, among the 2000 elements and compounds known to store hydrogen, none meets the requirements of high gravimetric and volumetric density [9]. It is easy to see that for a material to store hydrogen at around 10 wt %, it has to consist of light elements such as Li, B, N, C, Na, Mg, and Al. Unfortunately, hydrogen in materials consisting of light elements is held by strong covalent or ionic bonds. Consequently desorption temperatures of hydrogen in these materials are high and the kinetics are not favourable. Ideally hydrogen should be stored in such a way that it is neither easy (as would be the case if they are molecularly physisorbed) nor difficult for it to desorb (as would be the case if hydrogen is held in strong covalent or ionic bonds) at moderate temperatures. The central challenge then is to find materials that can store hydrogen like methane but whose kinetics and thermodynamics mimic that of intermetallics.

Recently a great deal of attention has been focused on sodium-alanates (NaAlH_4) which has a theoretical hydrogen content of 7.5 wt % [10-12]. Here the four hydrogen atoms form a tetrahedron that encapsulates an Al atom (much as in methane) and the AlH_4 unit is stabilized by the transfer of one electron from the Na atom. The four hydrogen atoms are covalently bonded to Al while AlH_4 unit is bonded to Na by an ionic bond. However, the addition of TiCl_3 to sodium-alanate was found to markedly lower the hydrogen desorption temperature [10]. This discovery has revitalized the research into complex light metal hydrides as potential hydrogen storage materials and has highlighted the role of catalysts. In spite of this interest, a fundamental understanding of where does Ti reside and how does it help to lower the hydrogen desorption temperature is lacking. In this paper we address these two important issues.

Using density functional theory and super cell band structure methodology we show that, in agreement with previous calculations [13], Ti prefers to occupy the Na site, but more importantly it leads to vacancy formation. While the energy necessary to remove a hydrogen

atom from NaAlH_4 and $(\text{Ti},\text{Na})\text{AlH}_4$ are respectively 5.1 eV and 3.0 eV respectively, that from sodium-alanate containing a Na-vacancy is only 1.3 eV. In addition, the removal of hydrogen from NaAlH_4 containing a Na vacancy is an exothermic process. Thus the recent observation of the rapid diffusion of hydrogen in sodium alanate following the addition of TiCl_3 is vacancy mediated.

Recently several experiments have been carried out to study the location of Ti in sodium-alanate, but they have yielded conflicting results. While some experiments suggest that Ti occupies the surface site, others find Na to occupy the bulk Na site. It is also believed that Ti combines with Al to form TiAl and segregates to the zone boundary. Recent calculations on clusters and crystals of Ti doped sodium-alanate reveal that Ti prefers the Na site over the Al site [13-15]. While no calculations on surfaces are available, the energy gain in replacing a Na atom in a cluster is much larger than that in the crystal. Since a cluster mimics the surface more closely than the bulk, one could argue that it may be energetically preferable for Ti to replace a Na atom on the surface rather than that in the bulk. The formation of TiAl can also be understood by noting that during ball milling, TiCl_3 interacting with Na can form NaCl and the Ti atoms thus released can combine with Al formed during the first dehydrogenation phase of the sodium-alanate. Calculations have shown that the strength of the Al-H bond is reduced when Ti replaces a Na site and hence the hydrogen desorption temperature is lowered [13-15]. We show here that a more powerful mechanism for hydrogen desorption is caused by the formation of Na vacancies. Note that for every TiCl_3 that combines with Na to form NaCl , two Na vacancies are created.

Computational method

Our calculations are carried out within the framework of generalized gradient approximation to the density functional theory using PAW method, as implemented in the VASP code [16]. In order to simulate both the Na vacancy formation and the Ti substitutions, we have constructed a $(2 \times 2 \times 1)$ super cell consisting of 96 atoms ($\text{Na}_{16}\text{Al}_{16}\text{H}_{64}$). This is shown in Fig1. The PAW potentials with the valence states 3p, 3d and 4s for Ti, 2p and 3s for Na, 3s and 3p for Al and 1s for H were used. We have chosen an energy cutoff of 300 eV. The optimization of the geometry has been done (ionic coordinates and c/a ratio), without any symmetry constraint using the Hellmann-Feynman forces on the atoms and stresses on the super cell. For sampling the irreducible wedge of the Brillouin zone we used k-point grids of $3 \times 3 \times 3$ for the geometry optimization and $5 \times 5 \times 5$ for the final calculation at the equilibrium volume. In all calculations, self-consistency was achieved with a tolerance in the total-energy of at least 0.1 meV/atom.

Results and Discussion

To model Ti doping as well as vacancy we have used the super cell $\text{TiNa}_{15}\text{Al}_{16}\text{H}_{64}$ and $\text{Na}_{15}\text{Al}_{16}\text{H}_{64}$ respectively. The energies needed to remove a hydrogen atom from these supercells are obtained by repeating the total energy calculations with the supercells $\text{TiNa}_{15}\text{Al}_{16}\text{H}_{63}$ and $\text{Na}_{15}\text{Al}_{16}\text{H}_{63}$ respectively. In Table I we present the binding energy corresponding to each of the three supercells as obtained from the VASP code. We had earlier shown that the energy of the supercell with Ti replacing the Na site is 0.90 eV lower than that with Ti replacing the Al site.

The energies needed to remove a hydrogen atom from the above super cells are defined as;

$$\begin{aligned}\Delta E^0 &= E[\text{Na}_{16}\text{Al}_{16}\text{H}_{64}] - E[\text{Na}_{16}\text{Al}_{16}\text{H}_{63}] \\ \Delta E^{\text{Ti}} &= E[\text{TiNa}_{15}\text{Al}_{16}\text{H}_{64}] - E[\text{TiNa}_{15}\text{Al}_{16}\text{H}_{63}]\end{aligned}$$

$$\Delta E^V = E[\text{Na}_{15}\text{Al}_{16}\text{H}_{64}] - E[\text{Na}_{15}\text{Al}_{16}\text{H}_{63}]$$

TABLE 1. Binding energies and energies to remove a hydrogen atom corresponding to various supercells of Ti and vacancy containing sodium alanate.

Supercell	Binding energy	Hydrogen removal energy (ΔE)
$\text{Na}_{16}\text{Al}_{16}\text{H}_{64}$	-313.298	5.1
$\text{TiNa}_{15}\text{Al}_{16}\text{H}_{64}$	-316.807	3.0
$\text{Na}_{15}\text{Al}_{16}\text{H}_{64}$	-307.955	1.3

One can see that the hydrogen removal energy in the system containing Na vacancy is about a factor of four smaller than that in the perfect crystal and a factor of two smaller than that when Ti substitutes the Na site. The origin of this reduction is found to be due to the relaxation of the H atoms around Al following the removal of hydrogen. While the three H atoms around Al in NaAlH_4 and $(\text{Ti},\text{Na})\text{AlH}_4$ remain in a nearly tetrahedral form, that in the vicinity of the vacancy form a nearly planar structure. The AlH_3 thus formed is very similar in structure to an AlH_3 cluster which is known to be a magic cluster in the gas phase. Furthermore, desorption of hydrogen from $\text{Na}_{15}\text{Al}_{16}\text{H}_{64}$ is an exothermic process since the desorbed hydrogen atoms can combine to form a H_2 molecule. Note that the binding energy of a H_2 molecule is 4.5 eV which is much larger than the 2.6 eV it costs to desorb two hydrogen atoms from $\text{Na}_{15}\text{Al}_{16}\text{H}_{64}$.

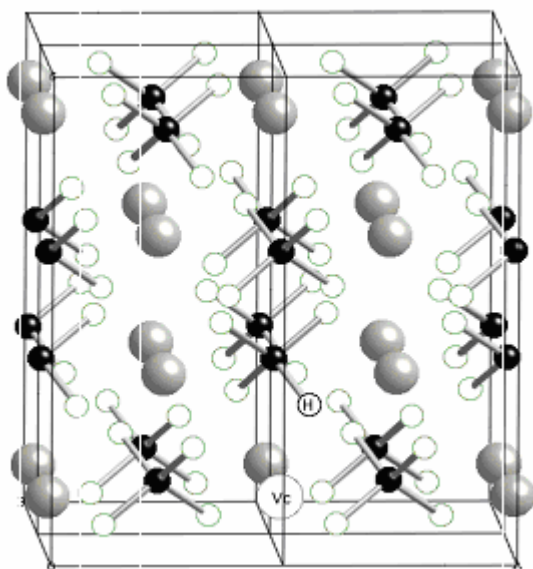


Figure 1. The 96-atom supercell geometry of $\text{Na}_{16}\text{Al}_{16}\text{H}_{64}$. The Na vacancy is marked by Vc and the hydrogen removed in the calculation is marked by H.

Conclusions

In summary, we have used density functional theory and super cell approach to study the Ti doping as well as Na vacancy in NaAlH_4 . We have found that Ti prefers to substitute the Na site and that the energy needed to remove a hydrogen atom is reduced from 5.1 eV in pure sodium alanate to 3.0 eV when doped with Ti. More importantly, we found that the presence of a Na vacancy plays an even larger role in the hydrogen desorption. The hydrogen removal

energy in this system (1.3 eV) is not only about a factor of four smaller than that in perfect crystal (5.1 eV), but also it is an exothermic process. Thus the dominant role of Ti in reducing hydrogen desorption temperature may be an indirect one - it leads to vacancy formation which then reduces the hydrogen desorption energy.

Acknowledgement. This work was supported in part by a grant from the department of Energy, Swedish Research Council (VR) and by the Swedish Foundation for International Cooperation in Research and Higher Education (STINT).

References

- See http://www.sc.doe.gov/bes/Basic_Research_Needs_To_Assure_A_Secure_Energy_Future_FEB2003.pdf
- Rigden, J. S. in *Hydrogen: The Essential Element*, Harvard University Press: Cambridge, MA 2003; pp.1; Gorchala, W. and Edwards P. *Chem. Rev.* **2004**, 104, 1283.
- Alper, J. *Science* **2003**, 299, 1686.
- Cortright, R. D.; Davada, R. R.; and Dumesic, J. A. *Nature* **2002**, 418, 964.
- Chen, P.; Xiong, Z.; Luo, J. Z.; and Tan, K. L. *Nature* **2002**, 420, 302.
- Rosi, N. L.; Eckert, J.; Eddaoudi, M.; Vodak, D. T.; Kim, J.; Keefe, M. O.; and Yaghi, M. *Science* **2003**, 300, 1127.
- Schlappbach, L.; and Züttel, A. *Nature* **2001**, 414, 353.
- see the report of DOE Workshop on hydrogen in <http://www.sc.doe.gov/bes/hydrogen.pdf>
- See data base <http://hydropark.ca.sandia.gov/>
- Boqdanovic, B.; and Schwickardi M. *J. Alloys Comp.* **1997**, 253, 1.
- Brinks, H. W.; Hauback, B. C.; Norby, P.; and Fjellvag, H. *J. Alloys Comp.* **2003**, 351, 222.
- Vajeeston, P.; Ravindran, P.; Vidya, R.; Fjellvag, H.; and Kjekshus, A. *Appl. Phys. Lett.* **2003**, 82, 2257.
- Jena, P.; and Khanna, S. N. *Chem. Phys. Lett.* (submitted).
- Iniguez, J.; Yildirim, T.; Udovic, T. J.; Sulic, M.; and Jensen, C. *M. Phys. Rev. B* **2004**, 70, 060101-1(R).
- Ahuja, R.; Jena P.; Guillén, J.M. O.; and Aratijo; C. M. (to be published).
- Kohn, W.; and Sham, L. *J. Phys. Rev.* **1965**, 140, A1133; Perdew, J. P.; Burke, K.; and Ernzerhof, M. *Phys. Rev. Lett.* **1996**, 77, 3865; Kresse, G.; and Heffner, J. *Phys. Rev. B* **1996**, 54, 11169.

HYDROGEN STORAGE IN MAGNESIUM BASED ALLOYS

William Stier, Luiz Gabriel Camargo, Finnbogi Óskarsson and Hannes Jónsson

Faculty of Science and Science Institute, University of Iceland

Introduction

Hydrogen is an appealing energy carrier, in particular for mobile applications such as cars and boats. But, storage remains a critical problem. While high pressure tanks are being used in several prototype cars today, the capacity is small and the volume large and it is likely that safety concerns will also call for alternative solutions. Light metal hydrides are a possible solution to this problem [1]. One example is magnesium hydride, MgH_2 , which contains 7.6% hydrogen by weight. There are two serious problems though: (1) the hydrogen binds so strongly in magnesiumhydride that temperature in excess of 700 K is needed to release the hydrogen, while a release temperature around 400 K would be preferable, and (2) the diffusion of hydrogen through the hydride is so slow that loading and unloading of hydrogen takes very long time [2]. The question is whether the binding energy can be reduced and the rate of diffusion increased by adding other elements to the magnesium while not reducing the mass ratio of hydrogen in the hydride too much. This question is being addressed by computational means.

Theoretical calculations

We have carried out various theoretical calculations based on density functional theory to study how binding energy and diffusivity of hydrogen change in magnesium hydride when other elements are added. The calculations make use of a plane wave basis set, ultrasoft pseudopotentials, the PW91 gradient dependent functional and the VASP code [3,4].

Results

We have carried out various theoretical calculations based on density functional theory to study how binding energy and diffusivity are affected by small addition of other light elements and transition metals to the magnesium. Some examples of results are discussed below.

The addition of aluminum was found to reduce the binding energy of hydrogen in the hydride. With a, Al molefraction of 0.15, the binding energy has been reduced from 0.38 eV to 0.24 eV, corresponding to hydrogen release at 1 bar and 350 K. The calculations were made assuming the rutile structure of the hydride remains stable, but it in fact becomes unstable with respect to phase separation. The calculations, however, illustrate that the addition of a rather small amount of a more electronegative element to the magnesium can significantly reduce the binding energy of the hydrogen in the hydride [5].

Experimental measurements have indicated that the addition of small amount of transition metal, for example titanium, can speed up the unloading of hydrogen from magnesium hydride [6]. A cubic crystal structure with a unit cell of Mg_7TiH_x was found from X-ray crystallography. The compound was synthesized under high pressure. Our calculations have shown that the hydrogen ions sit in tetrahedral holes in the lattice (unlike the rutile structure of pure magnesium hydride) and that $x=16$ [7]. The structure of the hydride is shown in figure 1. A large increase in diffusivity of hydrogen in the magnesium-titanium hydride is predicted from the theoretical calculations as compared with pure magnesium hydride, largely because of greatly reduced formation energy of hydrogen interstitials in the hydride.

Preliminary results on more complex compounds indicate that the lowering of binding energy that can be accomplished by adding a less electronegative element such as aluminum and the acceleration of diffusion that can be accomplished by adding a transition metal do not exclude each other and that a ternary alloy could both have reduced binding energy and fast diffusion. The task remains, however, to find a stable alloy where both the pure metal alloy and the hydride are stable. Theoretical calculations are being carried out to search for such an alloy.

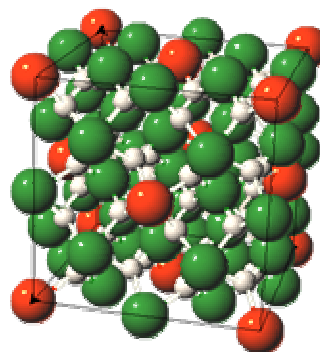


Figure 1. Structure of $\text{Mg}_7\text{TiH}_{16}$. The hydrogen ions sit in tetrahedral holes of the cubic Mg-Ti lattice.

References

- (1) L. Schlappbach and A. Züttel, *Nature* **2001**, 414, 353.
- (2) A. Krozer, P. Hjort and B. Kasemo. *J. Alloys. & Compounds* **1996**, 34, 11.
- (3) G. Kresse and J. Hafner, *Phys. Rev. B* **1993**, 47, 558; **1994**, 49, 14251.
- (4) J. P. Perdew, J. A. Chevary, S. H. Vosko, K. A. Jackson, M. R. Pederson, D. J., Singh, and C. Fiolhais, *Phys. Rev. B*, **1992** 46, 6671.
- (5) F. Óskarsson and H. Jónsson, (submitted to *J. Alloys. & Compounds*).
- (6) D. Kyoï *et al.*, *J. Alloys. & Compounds* **2004**, 375, 253.
- (7) W. Stier *et al.*, (in preparation).

HIGH LEVEL COMPUTATIONAL APPROACHES TO THE PREDICTION OF THE THERMODYNAMICS OF CHEMICAL HYDROGEN STORAGE SYSTEMS AND HYDROCARBON FUELS

David A. Dixon, Maciej Gutowski, Lisa Pollack, Theresa L. Windus, Wibe de Jong

Chemistry Department, University of Alabama, Tuscaloosa AL, 35487-0336; William R. Wiley Environmental Molecular Sciences Laboratory and Fundamental Sciences Directorate, Pacific Northwest National Laboratory, Richland WA 99352

Introduction

The development of H₂-based fuel cells promises clear economic, energy, and environmental security benefits to the United States. There is a critical need to develop new chemical H₂ storage materials and novel approaches for the release/uptake of H₂ for use in on-board transportation systems. An important need for understanding these materials and their performance are accurate thermodynamic data. Such data are needed in designing not only the release process but also the regeneration system. The suitability of the NH_xBH_x (x=1-4) compounds for hydrogen storage has recently been evaluated using theoretical methods.^{1,2} The amine boranes have excellent weight percent storage for H₂ with BH₃NH₃ having 19% if 3 molecules of H₂ are produced and the salt (NH₄)(BH₄) having 24% if 4 molecules of H₂ are produced. In both cases, the final product would be BN. Thus, the NH_xBH_x series of compounds (x = 1-4) are attractive targets for chemical H₂ storage materials.

The development of combustion models for hydrocarbon fuels requires reliable heats of formation of reactants, products and intermediates and as much kinetic information as possible about individual reaction steps. The heats of formation of the longer chain alkanes are of real interest in terms of developing models for gasoline and diesel fuel combustion. Although the heats of formation of the alkanes up through the nonanes are reasonably well-established, there is much less known about the heats of formation of higher alkanes, especially the cetanes and other compounds of interest for diesel fuel.³ There is also little reliable information currently available for the heats of formation of many of the radical intermediates of interest in combustion processes.

We have been developing an approach to the reliable calculation of molecular thermodynamic properties, notably heats of formation, based on *ab initio* molecular orbital theory.⁴ Our approach is based on calculating the total atomization energy of a molecule and using this with known heats of formation of the atoms to calculate the heat of formation at 0K. This approach starts with coupled cluster theory, including a perturbative triples correction (CCSD(T)), combined with the correlation-consistent basis sets extrapolated to the complete basis set limit to treat the correlation energy of the valence electrons. This is followed by a number of smaller additive corrections including core-valence interactions and relativistic effects, both scalar and spin-orbit. Finally, one must include the zero point energy obtained either from experiment, theory, or some combination.

We have applied this approach to the prediction of the heats of formation of the molecular amine boranes, BH₃NH₃, BH₂NH₂, and HBNH, and the ion BH₄⁻ which in combination with our previous work on BH₃, B₂H₆, NH₃, and NH₄⁺ can be used to predict the thermodynamics of reactions of these species. We have also used this approach to predict the heats of formation of the hydrocarbon fuels C₅H₁₂, C₆H₁₄, and C₈H₁₈.

Computational Approach

For the current study, we used the augmented correlation consistent basis sets aug-cc-pVnZ for H, B, and N (n = D, T, Q).⁵ Geometries were optimized at the CCSD(T) or MP2 levels with these types of basis sets. Zero point energies were obtained at the CCSD(T) or B3LYP level with these types of basis sets and scaled to experiment to obtain the best estimate of the zero-point energy. The CCSD(T) total energies were extrapolated to the CBS limit by using a mixed exponential/Gaussian function of the form:

$$E(n) = E_{\text{CBS}} + A \exp[-(n-1)] + B \exp[-(n-1)^2] \quad (1)$$

with n = 2 (DZ), 3 (TZ) and 4(QZ). Core-valence corrections, ΔE_{CV} , were obtained at the CCSD(T)/cc-pCVTZ level of theory. Relativistic corrections were obtained at the CI-SD/cc-pVTZ level with ΔE_{SR} taken as the sum of the mass-velocity and 1-electron Darwin (MVD) terms in the Breit-Pauli Hamiltonian⁶ or at the MP2/aug-cc-pVTZ level with the spin-free, one-electron Douglas-Kroll-Hess (DKH) Hamiltonian.⁷ Atomic spin-orbit corrections were taken from the excitation energies of Moore.⁸ By combining our computed ΣD_0 values with the known heats of formation⁹ at 0 K for the elements we can derive ΔH_f^0 values for the molecules under study in the gas phase.

The calculations were done with the program systems MOLPRO and NWChem. The calculations required considerable computational resources and many of them were done on the massively parallel 1980 processor HP Linux cluster with Itanium-2 processors located in the Molecular Sciences Computing Facility in the William R. Wiley Environmental Molecular Sciences Laboratory at the Pacific Northwest National Laboratory. The largest calculation performed was the CCSD(T)/aug-cc-pVQZ calculation on octane with 1398 basis functions. The perturbative triples (T) for octane took 23 hours on 1400 processors, with 75% CPU efficiency and a sustained performance of 6.3 TFlops. Fourteen iterations were required for convergence of the CCSD, which took approximately 43 hours on 600 processors. As far as we are aware, is one of the largest CCSD(T) calculations ever performed.

Results and Discussion

Borane Amines. The calculated heats of formation are given in Table 1. The calculated heats of formation for BH₃ and NH₃ are in excellent agreement with experiment as we have previously shown. Our current calculated value for $\Delta H_f^0(\text{BH}_3)$ is 26.4 kcal/mol and for $\Delta H_f^0(\text{NH}_3)$ is -9.6 kcal/mol. The dissociation energy of BH₃NH₃ has been estimated to be 31.1 ± 1 kcal/mol based on the binding energy for the adduct of BH₃ with N(CH₃)₃.¹⁰ Our calculated value at 0K is 25.9 kcal/mol with zero point effects included, about 5 kcal/mol lower than the estimated value. We suggest that our value for the binding energy of BH₃NH₃ is the best available value and, hence, our heat of formation is the best available value.

Table 1. Borane-Amine Heats of Formation at 0 K (kcal/mol).

Molecule	Calc(298K)	Expt(298K)
BH ₃ NH ₃	-13.5	
BH ₂ NH ₂	-18.6	
HBNH	12.8	
BN(³ Π)	147.1	114 ± 30
BH ₄ ⁻	-13.5	
BH ₃	25.5	
NH ₃	-11.3	-10.97 ± 0.10
NH ₄ ⁺	150.9	

Based on the calculated values, we can calculate the energy for the sequential release of H₂ from these molecules in the gas phase:

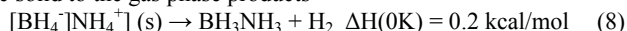


Clearly, BH_3NH_3 will be a good source of H_2 as the release of H_2 from this species is not far from thermoneutral. For comparison, we list the energies of the following gas phase reactions based on hydrocarbons

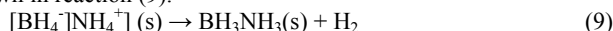


Based on these results, it is clear that the hydrocarbons cannot release H_2 . What is surprising is how close the reaction energies are for reactions (3) and (6) and reactions (4) and (7). This is a manifestation of similarity of the isoelectronic CCH_m and BNH_m systems.

Another possibility for an H_2 storage system is the salt $[\text{BH}_4^-][\text{NH}_4^+]$. We can estimate the lattice energy of the salt from an empirical relationship and experimental ionic volumes¹¹ giving a lattice energy of 151.3 kcal/mol and a calculated heat of formation of the salt at 0K of -9.3 kcal/mol. Alternatively, we may use the calculated volume at the DFT level of 0.098 nm³ for solid $[\text{BH}_4^-][\text{NH}_4^+]$, which leads to a lattice energy of 146.1 kcal/mol and a heat of formation of the salt at 0K of -4.1 kcal/mol. The reaction from the ionic solid to the gas phase products



is essentially thermoneutral and the salt would be a good source of H_2 . In order for the salt to be stable, we need to look at the possibility of electron transfer. The electron affinity (EA) of NH_4^+ is very low as NH_4 is a Rydberg molecule with only a weak binding of H to NH_3 if at all. Thus we can estimate the EA(NH_4^+) as the energy of the reaction $\text{NH}_4^+ + \text{e}^- \rightarrow \text{NH}_3 + \text{H}$ giving -111.6 kcal/mol (4.84 eV). The ionization potential of BH_4^- is given by the reaction $\text{BH}_4^- \rightarrow \text{BH}_3 + \text{H} + \text{e}^-$ as BH_4 is also a very weakly bonded system and the electron affinity of BH_3 is very small ($0.038 \pm 0.015 \text{ eV} = 0.88 \pm 0.35 \text{ kcal/mol}$).¹² The ionization potential of BH_4^- is 89.6 kcal/mol (3.89 eV). The fact that the electron affinity of NH_4^+ and the ionization potential of BH_4^- are comparable within 1 eV of each other is consistent with the fact that this salt can be produced. Another possibility for the formation of $\text{H}_2(\text{g})$ is formation of $\text{NH}_3\text{BH}_3(\text{s})$ as shown in reaction (9).



The calculated cohesive energy for BH_3NH_3 is 17 kcal/mol and the enthalpy change for the hydrogen release reaction is substantially more exothermic, $\Delta\text{H}(0\text{K}) = -16.8 \text{ kcal/mol}$, than if $\text{BH}_3\text{NH}_3(\text{g})$ is produced.

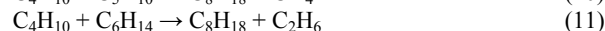
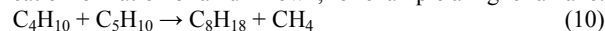
Alkanes. The calculated heats of formation for octane, hexane and pentane at 298K are given and compared to experiment in Table 2. The calculated values are in excellent agreement with experiment, differing at most by 0.30 kcal/mol for octane, which is within our desired uncertainty of $\pm 1 \text{ kcal/mol}$. The result for pentane only differs by 0.07 kcal/mol from the experimental value. It is useful to remember that there is a $\pm 0.1 \text{ kcal/mol/C atom}$ uncertainty in our calculated heats of formation due to the uncertainty in the heat of formation of the C atom in the gas phase. For octane, the uncertainty in the atomization energy alone due to the uncertainty in $\Delta\text{H}_f(\text{C})$ is 0.8 kcal/mol. Our value of -50.20 kcal/mol for $\Delta\text{H}_f^{298}(\text{C}_8\text{H}_{18})$ octane's heat of formation compares favorably to the G3 value -50.74 kcal/mol.¹³ As noted by Redfern et al., conformational averaging, which is more important the larger the chain, will raise our calculated value by 0.5 to 1 kcal/mol. For example, they calculated corrections due to conformational averaging of 0.26 and 0.46 kcal/mol for n- C_4H_{10} and n- C_5H_{12} , respectively. Even with the conformational averaging correction, our calculated values would still be in excellent agreement with the experimental values.

In order to calculate the heats of formation of larger alkanes, we can consider other approaches including the use of isodesmic reactions. For example, the reaction energy for the following two

Table 2. Heats of Formation of Alkanes at 298 K (kcal/mol).

Molecule	CCSD(T)	Expt ^{3,9}
CH_4	-17.6	-17.81 \pm 0.10
C_2H_6	-20.3	-20.03 \pm 0.07
C_4H_{10}	-30.1	-30.31 \pm 0.14
C_5H_{12}	-35.0	-35.11 \pm 0.19
C_6H_{14}	-40.2	-39.89 \pm 0.19
C_8H_{18}	-50.2	-49.90 \pm 0.31

isodesmic reactions could be used in a reverse process to calculate the heat of formation of an unknown, for example a higher alkane:



The reaction energies are given in Table 3 and the overall agreement is good within 1 kcal/mol for all methods and basis sets.

Table 3. Isodesmic reaction energies in kcal/mol^a

Approach	Reaction 10	Reaction 11
Experiment ^{3,9}	-3.9 \pm 0.7	-0.7 \pm 0.7
aVDZ/MP2	-4.2	-0.5
aVTZ/MP2	-3.5	-1.1
aVQZ/MP2	-3.5	-0.2
CBS/MP2	-3.7	0.3
CCSD(T)/aVDZ	-4.2	-0.9
CCSD(T)/aVTZ	-3.3	-0.4
CCSD(T)/aVQZ	-3.3	-0.4
CCSD(T)/CBS	-3.3	-0.3
CCSD(T)/CBS + all corrections	-3.2	-0.2

References

- Gutowski, M.; Autrey, T. Prepr. Pap. -Am. Chem. Soc., Div. Fuel Chem. **2004**, 49, 275.
- Gutowski, M.; Autrey, T.; Linehan, J. J. *Phys. Chem. A*, submitted for publication.
- Pedley, J.B. "Thermochemical Data and Structures of Organic Compounds, Volume I" TRC Data Series, Thermodynamics Research Center, College Station TX, 1994.
- Feller, D.; Dixon, D. A. *J. Chem. Phys.* **2001**, 115, 3484.
- Kendall, R. A.; Dunning, T. H., Jr.; Harrison, R. J. *J. Chem. Phys.* **1992**, 96, 6796.
- Davidson, E. R.; Ishikawa, Y.; Malli, G. L. *Chem. Phys. Lett.* **1981**, 84, 226.
- Douglas, M.; Kröll, N. M. *Ann. Phys.* **1974**, 82, 89; Hess, B. A. *Phys. Rev. A* **1985**, 32, 756; Hess, B. A. *Phys. Rev. A* **1986**, 33, 3742.
- Moore, C. E. "Atomic Energy Levels," Washington, D.C.; Vol. U.S. National Bureau of Standards Circular, **1949**, 467, NBS.
- Chase, M.W., Jr.; NIST-JANAF Tables (4th Edition), *J. Phys. Chem. Ref. Data*, Mono. 9, Suppl. 1 (1998); Ruscic, B.; Mayhew, C.A.; Berkowitz, J. *J. Chem. Phys.* **1988**, 88, 5580.
- Haaland, A. *Angew. Chem.* **1989**, 101, 1017.
- Jenkins, H. D. B.; Roobottom, H. K.; Passmore, J.; Glasser, L. *Inorg. Chem.* **1999**, 38, 3609.
- Wickham-Jones, C.T.; Moran, S.; Ellison, G.B., *J. Chem. Phys.*, **1989**, 90, 795.
- Redfern, P.C.; Zapol, P.; Curtiss, L.A.; Raghavachari, K. *J. Phys. Chem. A*, **2000**, 104, 5850.

CURRENT ADVANCEMENTS AND NEEDS IN DIESEL FUEL COMBUSTION MODELING

Daniel T. Daly Ph.D.

Director of AIME
University of Alabama

Introduction:

There has been great progress in the modeling of the combustion event. Kinetic models exist that can capture many of the hydrocarbons that are combusted in today's internal combustion engines. Modeling of the detailed oxidation of C10-C11 fuels are currently being used by researchers in advanced combustion investigations. Some of the oxidative mechanisms capture the formation of soot precursors up to several ring complexes.

However, the modeling community still lags behind advances in combustion schemes employed by engine manufacturers. Kinetic combustion models are rarely used on engine design teams who are optimizing combustion chambers for power and emissions.

As the world searches for cleaner sources of fuel for combustion, the need for detailed kinetic models to assist in this search increases. In this paper an overview of the current conceptual model of diesel combustion is given. The current advances of kinetic modeling will be highlighted along with gaps. Potential methods to address these shortcomings will be discussed.

Conceptual Model of Diesel Combustion

In direct-injection diesel engines, liquid fuel, injected at high pressure, penetrates into the in-cylinder gases and the fuel jet expands into a conical shape with a roughly uniform cone angle as the in-cylinder gases are entrained. The thermal energy provided by the entrained in-cylinder gas heats and vaporizes the liquid fuel, and at some downstream location, termed the "liquid length", no liquid-phase fuel remains [1,2]. Momentum carries the vapor fuel downstream of the liquid length where it continues to entrain hot in-cylinder gases. First-stage ignition reactions commence in this fuel-rich, high-temperature mixture of vapor fuel and entrained air. Excited chemical species formed during the first stage of ignition emit low levels of light (chemiluminescence), and this emission provides a spatial indicator of the reactions that lead to ignition [3]. After a short time (~1 ms), the reactions evolve into highly exothermic second stage ignition reactions, leading to the "premixed burn" phase of diesel combustion. A diffusion flame quickly forms on the periphery of this high-temperature region, and grows upstream to surround the rich core of the diesel plume [3,4]. The upstream edge of the diffusion flame does not extend fully to the injector nozzle, but rather it remains some distance downstream of the nozzle. The distance from the nozzle orifice to the most upstream extent of the diffusion flame is termed the "lift-off length" [4].

After the initial transient of the diesel ignition process but before the end of injection, the diesel plume enters a "quasi-steady" period, when the characteristic description of combustion does not change, as depicted in Fig. 1. During this quasi-steady period, in-cylinder gases are entrained along the whole length of the combusting jet as it expands downstream. Downstream of the lift-off length, oxygen in the entrained gas is quickly consumed by the fast, high-temperature reactions in the diffusion flame. As a result, downstream of the lift-off length, most of the oxygen is carried into

the central region of the jet only in the form of the combustion products of the diffusion flame. Upstream of the lift-off length, however, unreacted oxygen is entrained into the jet, and mixes with the liquid spray and vaporized fuel as it is transported downstream. Based on observations from planar laser imaging experiments [4], it has been hypothesized that this hot (700-900 K), fuel-rich mixture is transported downstream of the liquid-phase fuel, where it reacts in a standing premixed combustion zone within the jet, as shown schematically in Fig. 1. These exothermic reactions in the standing premixed combustion zone raise the temperature of this fuel-rich mixture as the available fresh oxygen is consumed. The resulting fuel-rich product mixture (1300-1600 K) is ideal for formation and growth of soot, which occurs downstream of the standing premixed reaction zone, throughout the central region of the jet [4].

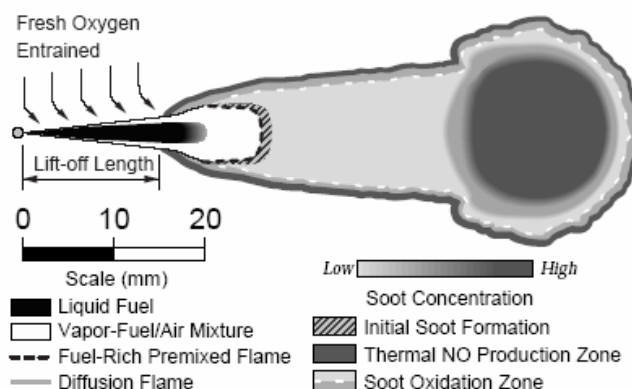


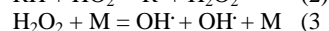
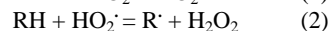
Figure 1. Conceptual Model of Diesel Combustion

Schematic of the quasi-steady state period according to the conceptual model of diesel combustion. Currently, kinetic models do not capture many of the aspects of this conceptual model of diesel combustion.

Westbrook's n-heptane Model

This reaction mechanism is constructed based on the hierarchical nature of hydrocarbon-oxygen systems. It is built in a stepwise fashion starting with small hydrocarbons and progressing to larger ones. A semi-detailed kinetic scheme developed by Ranzi et al. [5] in which both the low and the high temperature reaction sub-mechanisms are reduced to a lumped kinetic model involving a limited number of intermediate steps has been employed in this mechanism. [6]

The general features of Westbrook's models are the importance of the initiation reactions, chain propagation reactions, chain branching reactions and chain termination reactions. Of particular interest, was how the thermal energy of the initial bond dissociation is stored and later released during the pre-mixed burn phase of diesel combustion. Westbrook's model handles this by the formation of hydrogen peroxide by the reaction sequence below:



This is a clever means to allow for the complex kinetic feature of low temperature hydrocarbon oxidation to occur yet delays the introduction of hydroxyl radicals till a temperature of 1000K occurs.

This delay is accomplished by condition of bond dissociation of H_2O_2 . It can be observed that the onset of H_2O_2 build up is slower for the fuel containing ethanol than for the diesel fuel, which is consistent on the impact of ethanol on cetane. Also it is consistent with a plot of Time versus Temperature. These two plots demonstrate that Westbrook's heptane oxidation model does simulate conditions of low temperature diesel combustion.

Frenklach's Soot Model

The model developed by the Frenklach group combines developments in gas-phase reactions, aromatic chemistry, soot-particle coagulation and soot particle aggregation. In this investigation the gas phase reactions were not used.

Kinetic studies with this model revealed [7] a dominant kinetic pattern of aromatic-ring growth, H-abstraction C_2H_2 addition (HACA). This reaction scheme is adopted for surface growth of soot particles, and the combined soot formation model reproduces such diverse soot characteristics as soot yield, sooting limits, and particle size.

The reaction steps comprising HACA has been subjected to theoretical scrutiny [8] and these efforts produced a mutually consistent set of reaction rate coefficients, thermodynamic data, and transport properties for PAH compounds. A data based kinetic model has been developed and shown to reproduce the concentration profiles of major, intermediate, and aromatic species from several studies of acetylene and ethylene flames.

The Frenklach model attempts to capture all of the cyclization reactions leading to formation of aromatic compounds in the complex array of species in the soot formation pathway.

The main radical recombination reactions for the formation of aromatic rings is shown below in reactions

Heptane-Soot Model

A detailed kinetic model of soot formation, from the perspective of computer implementation, can be considered to consist of two principal components: gas-phase chemistry, which determines the flame structure, and soot particle dynamics, which describes the evolution of the particle ensemble. The correctness of the particle dynamics submodel relies, first of all, on the accuracy of the species profiles supplied by the gas-phase submodel, those that define the soot particle nucleation and surface growth rates.

The n-heptane mechanism was used for generation of the gas chemistry and the Frenklach soot model was used for the soot particle dynamics. The combination of these gave rise to a mechanism having 614 species and 2883 reactions. This was done on the premise that the heptane mechanism would cause the fuel pyrolysis leading to the formation of basic radicals, which would activate the soot build up mechanism.

The duplication, which arose from the combination, was avoided by eliminating the duplicate reactions from the soot mechanism. The reasoning behind this step was that the duplicate reactions were mostly those involving the gas-phase chemistry and since heptane was being used as the fuel, it would be reasonable to retain the gas-phase chemistry from the model causing the fuel breakdown.

Gaps in the Oxidative Pathways

Dec et al [9] investigated the impact of heavier boiling components of diesel fuel on his conceptualization model and discovered a strong correlation between the T50 of the fuel and the in-cylinder liquid penetration. Figure 2 shows the results of this study. In this investigation a high sooting fuel BP 5080 was

fractionated into three cuts: high, medium and low. The high cut had the longest in-cylinder liquid penetration.

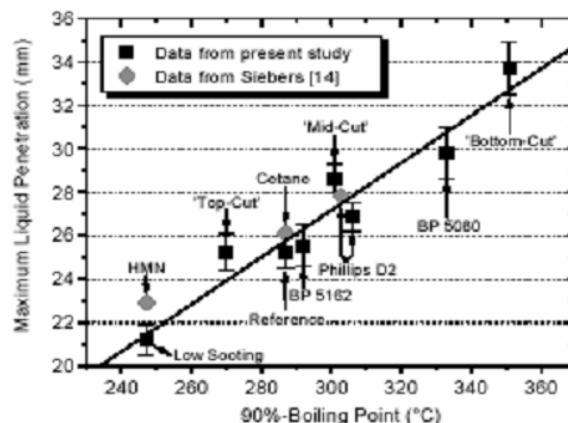


Figure 2. Maximum liquid phase fuel penetration correlated with 90% boiling point.

This work was done to look into a pyrolytic pathway postulated by Toyota Research. In their work, they also fractionated diesel fuel and discovered that the chromatogram of the heavier boiling fraction which were placed back into the diesel fuel was identical to the chromatogram of the soluble organic fraction of the particulates captured when the doped fuels were tested.

These two studies suggest that along with the oxidative pathway a pyrolytic pathway needs to be included into the kinetic models.

Another gap is a detailed oxidation of the soot particle in the later stages of combustion. Even though Frenklach's model has reversible pathways in his soot formation models, soot oxidation needs to be explored as the soot particle crosses the flame sheath and in the later stages of combustion when pockets of high hydroxyl radicals come into contact with soot particles.

Promising Developments

A. Lutz and J Broadwell [10] have developed a Two-staged Lagrangian approach to introduce some basic fluid dynamic process into the fuel oxidation pathways. In this approach, an interactive two reator model is used such that flame chemistry can be introduced into the fuel model. The mixing rules were determined experimentally.

A. Violi, G. A. Voth and A. F. Sarofim have developed a method of model soot precursors to soot particles using a combination of Kinetic Monte Carlo and Molecular Dynamics methodologies. They were able to model a soot particle formation while preserving the atomic scale structure with three-dimensional features.

W. Tsang at NIST has made great progress in delineating pyrolytic pathways in hydrocarbons. A combination of the oxidative and the pyrolytic pathways needs to be integrated to form a comprehensive model.

References

- (1) Espey, C. ; J.E. Dec, Society of Automotive Engineering Paper 952456, 1995
- (2) Naber, J. D.; Siebers, D. L., Society of Automotive Engineering Paper 960034, 1996
- (3) Espey, C. ; J.E. Dec, Society of Automotive Engineering Paper 982685 1998
- (4) Dec, J. E. ; Society of Automotive Engineering Paper 970873, 1997

- (5) Ranzi, E., Gaffuri, P., Faravelli, T., and Dagaut, P., *Combust. and Flame*, 103:91-106 (1995)
- (6) Curran, H. J., Gaffuri, P., Pitz, W. J., and Westbrook, C. K., *Combustion and Flame*, 1998
- (7) Chevalier, C., Pitz, W. J., Warnatz, J., Westbrook, C. K., and Melenk, H., Twenty-Fourth Symposium (International) on Combustion., The Combustion Institute, Pittsburgh, 1992, pp. 92-101
- (8) Wang, H., and Frenklach, M., *Combust. Flame* 96:163 (1994)
- (9) Cannan, R. E. , Dec, J. E., Daly, D. T.; Society of Automotive Engineering Paper 980510, 1995
- (10) Broadwell, J., Lutz, A.; *Combustion and Flame* 114,319-345 1998

BARRIERS TO DEVELOPING SIMULATION MODELS FOR REAL TRANSPORTATION FUELS

Jeffrey A. Manion, Donald R. Burgess, Jr., Thomas C. Allison,
Jeffrey W. Hudgens, and Wing Tsang

Physical and Chemical Properties Division, MS 8380
National Institute of Standards and Technology
Gaithersburg, Maryland 20899

Introduction

Combustion of fuels for energy production plays an enormous role in the United States economy and there are well-recognized benefits that would accrue from increased energy efficiency and pollution minimization.¹ For these benefits to be realized, it is necessary to efficiently translate our underlying scientific understanding of combustion to technological development. The cost and time delays associated with purely empirical approaches make it essential to better develop the means to realistically simulate combustion processes for device design purposes. Such simulations entail combining Computational Fluid Dynamics (CFD) with detailed chemical kinetic models. While this is becoming an increasingly tractable problem there are a number of barriers that continue to retard progress in the field. The purpose of this paper is to provide an overview of some of the challenges, with an emphasis on what is needed to further develop chemical kinetic models.

The Role of Simulations in Combustion Science.

Combustion is a complex process controlled by a combination of chemistry (kinetics) and fluid dynamics (mixing). The complexity of the process means that optimum solutions that balance efficiency and pollutant production are beyond simple or intuitive analysis. Design goals are frequently directly competing. For example higher temperature conditions that reduce particulate formation (soot) lead to increased NO_x, while lower temperatures that control NO_x lead to increased particulates. The high dimensionality of these models, the nonlinearity of the underlying differential equations, and the multifaceted dependence on temperature and pressure mean that the only cost and time effective means of exploring the relevant phase space is through computer simulation. This is not a surprise. Computer-based simulations are at the heart of all modern device design methods. Such simulations have been used for years with great success in, for example, aerodynamics and computer chip design. Indeed in these fields no one would seriously undertake the design of a new product without employing such tools.

In the above two examples the simulations are of purely physical phenomena. The situation for combustion is more complex in that it involves both physical and chemical processes. This added complexity requires both more computing power and a greater degree of interdisciplinary knowledge. This added dimensionality has impeded progress in this field. Until recently the required computing power was simply not available. However, the latest generation of computational fluid dynamics (CFD) codes is able to incorporate a sufficient amount of chemistry to realistically simulate complex processes. The time is ripe for application of these methods to the design and optimization of real devices. Specific examples include the use of additives, the design of nozzles, changing the geometric configuration of combustors, the effect of fuel composition, or a combination of these possibilities. In the absence of a simulation tool direct physical testing is the only alternative. This is extremely slow and expensive, making it effectively impossible to explore novel designs that could dramatically advance the field.

Technical Challenges: Scientific Infrastructure Development.

Simulations of real combustion devices span length scales ranging from atoms and molecules up to engines and turbines. The required disciplines include kinetics, thermodynamics, computational chemistry, fluid dynamics, mechanical design, and a host of mathematical methods. The facile exchange of data across these scientific domains and multiple length scales is a large barrier to progress in the area of combustion processes.

A significant problem in describing the chemistry is that there currently exist no generally accepted standards for nomenclature, notation, and traceability of the information contained in the detailed chemical kinetic models used to describe combustion systems. Such standards are primary requirements needed to facilitate the comparison and improvement of models developed by different researchers. Historically, when reaction sets were small such limitations were relatively easy to overcome. However, as the amount of available information and complexity of models has grown from tens of reactions to thousands, it has become increasingly difficult to process the data in the absence of computer automation. This explosion of information continues to increase as the multi-channel nature of many combustion reactions is taken into account and computational chemistry methods lead to more detailed information about potential energy surfaces of reactions.

Automated processing of the available data requires not only the development of information standards, but also the development of a wide variety of community tools. Such tools are needed to fill gaps in experimental data with adequate estimates, to generate and analyze large kinetic models,^{2,3} and then to reduce the large models to sizes acceptable to CFD codes. The latter step must of course be done without losing the decisive information needed for design purposes. The propagation of uncertainties in the input parameters to uncertainty in the predictions remains an often neglected area of key importance.⁴

There are a number of efforts under development that address various aspects of the required infrastructure.⁵⁻⁷ While promising, many of these efforts are in the early stages and the support infrastructure is not yet well-developed. We at NIST believe that it is crucial that this development continue and become a collaborative, community-wide effort.

Technical Challenges: Surrogate Fuels.

Real liquid fuels such as gasoline, diesel, and aviation fuels are complex mixtures containing hundreds of compounds. These mixtures are specific cuts and blends from many different refinery streams and depend on the origin of the crude, the specific refinery, and other factors such as seasonal needs and additives. Nonetheless the hydrocarbon constituents of gasoline, diesel, and aviation fuels encompass the same set of compound classes, albeit in significantly different proportions.

The idea of using surrogate fuels is that each chemical class can be adequately represented by a single or small number of model compounds. Various mixtures of these model compounds could then be matched to and used to mimic the chemical and physical properties of the real mixtures. An obvious advantage is that researchers could conduct experiments on highly reproducible standards. Equally important, a greatly reduced reaction set would be required to develop detailed chemical kinetic models.

For example, the surrogate mixture(s) for diesel fuel will contain different relative amounts of the model compounds than the surrogates for gasoline or aviation fuel. It is further likely that a range of surrogate mixtures may be needed to accurately mimic any property of interest, *e.g.*, the best surrogate to understand sooting may be different from that most useful to model ignition

characteristics. The key point is that the same chemical and kinetics properties databases will support modeling of all these mixtures. This approach thus leverages the research efforts across the community and supports the combustion simulation needs of all sectors of the transportation industry.

At a recent workshop¹ held at NIST there was general consensus that the surrogate approach is likely to be profitable and a tentative set of surrogate model compounds was identified. The ultimate validity of these suggestions will, of course, require significantly more testing and scientific review.

Technical Challenges: Chemical Understanding.

While the scientific understanding of combustion has advanced tremendously in the past several decades, there remain gaps in our understanding of the chemistry. Combustion remains an area where continuing basic research is needed to address the technological needs. Although by no means a complete listing, a few of the more prominent issues are touched on below.

Decomposition of large fuel molecules. One of the main initial steps in the combustion of a hydrocarbon fuel is abstraction of hydrogen, usually by OH radical, to form water and an unstable hydrocarbon radical intermediate. A difficulty in the treatment of real fuels has been our understanding of the subsequent breakdown of the radical intermediate. This intermediate may isomerize to a variety of other radicals or decompose in a unimolecular fashion. The information of ultimate utility is the product distribution, which is determined by this multi-channel competition. An additional complication is that the branching ratio is dependent on both temperature and pressure. The final situation is quite complex. Until recently there were a number of technical challenges to correctly treating such systems. However, with the development of programs such as NIST ChemRate¹⁰ it is now possible to rigorously treat multi-channel pressure dependent reactions. This program enables one to extrapolate rate constants determined under one set of temperature and pressure conditions to all others. Although requiring some work, the analysis will lead to analytical rate expressions suitable for input into the combustion models and need only be done once.

Cool Flames. For ground-based transportation, the Homogenous Charged Compression Ignition (HCCI) engine is one of the more promising engine designs on the horizon. HCCI promises a significant increase in energy efficiency while reducing the formation of pollutants. A barrier to progress in this area is our ability to understand and control the ignition characteristics in the cool flame temperature regime. The chemistry involves the formation and subsequent reaction of many peroxy radical species. The nature of the radical isomerization reactions and the competition between isomerization and bimolecular reactions appears to play a dominant role in controlling the pressure and temperature behavior. This is a rich area that will require continued experiments as well as the application of computational chemistry methods to better understand the complex energy surfaces.

Additives. An ongoing issue is the effect of additives on the chemistry of combustion and the ability of additives to limit the formation of soot and other pollutants. In general the behavior additives can be treated as an overlay to the base hydrocarbon chemistry. The details will obviously vary with the nature of the additive.

Soot and Soot Precursors. The formation and burnout of soot and soot precursors remains an area of very active research and development.^{8,9} These efforts are driven by regulatory concerns stemming from the health effects of particulates as well as unfavorable consequences related to tracking signatures of jet aircraft and deleterious effects of soot on turbine performance.

In a detailed chemical kinetic sense, the tremendous complexity of soot particles means that it is realistic to envision the development of detailed kinetic models that enumerate all chemical species only for the early stages of soot formation. This may be sufficient for purposes of controlling soot formation in some instances. Additional models are needed, however, that propagate the growth processes up through larger particulates or consider the burnout of particulates. In such cases it is a practical necessity to use approaches that lump reactions and species. Such models are under development by various groups. In addition to continued development of the specific and lumped models, a better understanding of how to interface the two approaches is needed.

Final Comments

We have provided a brief overview of a number of barriers that need to be overcome to address the complexities associated with real transportation fuels. History makes it clear that dedicated researchers will overcome the individual scientific technical challenges to our understanding of combustion. There is less precedent for the multi-disciplinary cooperation that is necessary to rapidly address the practical technological needs. At the heart of this uncertainty is the need for the creation of an organized standard infrastructure for the exchange of combustion related data. The recent efforts in this direction are promising and will hopefully begin to bear fruit in the near future.

References

- (1) Tsang, W.; Hudgens, J.W.; Allison, T. C.; Burgess, D. R., Jr.; Manion, J. A.; Matheu, D. M.; *Workshop on Combustion Simulation Databases for Real Transportation Fuels* (National Institute of Standards and Technology, Gaithersburg, MD 20899, September 4-5, 2003), NISTIR 7155.
- (2) Bhattacharjee, B.; Schwer, D. A.; Barton, P. I.; Green, W. H. ; *Combust. Flame*, **2003**, *135*, 191-208.
- (3) Tomlin, A. S.; Turanyi, T.; Pilling, M.J. In *Comprehensive Chemical Kinetics. Low Temperature Combustion and Autoignition*; Pilling, M. J. and Hancock, G., Eds.; Elsevier, Amsterdam, 1997; pp. 293-437.
- (4) Hoffmann, V. H.; McRae, G.J.; Hungerbuhler, K.; *Ind. Eng. Chem. Res.*, **2004**, *43*, 4337-4349.
- (5) PrIme (Process Informatics Model). <http://www.me.berkeley.edu/prime/>
- (6) CMCS (Collaboratory for Multi-Scale Chemical Science). <http://cmcs.org/>
- (7) NIST Detailed Chemical Kinetic Combustion Model Database. <http://kinetics.nist.gov/realfuels/>
- (8) Violi, A.; Sarofim, A.F.; Voth, G. A.; *Comb. Sci. Tech.*, **2004**, *176*, 991-1005.
- (9) Frenklach, M.; *Phys. Chem. Chem. Phys.*, **2002**, *4*, 2028-2037.
- (10) NIST ChemRate. A Computational Database for Unimolecular Reactions. <http://www.nist.gov/kinetics/chemrate/chemrate.html>

THE NIST "REAL FUELS" DETAILED CHEMICAL KINETIC COMBUSTION MODEL DATABASE

Donald R. Burgess, Jr., Jeffrey W. Hudgens,
Thomas C. Allison, Wing Tsang, and Jeffrey A. Manion

Physical and Chemical Properties Division, MS 8380
National Institute of Standards and Technology
Gaithersburg, Maryland 20899

Introduction

Existing evaluated databases addressing combustion needs are not continually updated and, consequently, often do not reflect current accepted "best" values. The "Workshop on Combustion Simulation Databases for Real Transportation Fuels" identified a strong need for "critically evaluated" databases of thermochemical properties and elementary reaction rate coefficients to support detailed chemical kinetic models.¹ A critically evaluated database would target important combustion species and reactions. For each species and reaction, a critically evaluated database would list "recommended" numbers found by identifying the best data along with the set of other values available in the literature, including those obtained from reviews, experimentally derived data, and quantum calculations, as well as estimated values. The existence of critically evaluated databases would greatly reduce the extensive effort required to trace and ascertain the quality and uncertainty of thermochemical and chemical kinetic data used in detailed chemical kinetic models for combustion applications.

A compilation of complete and reduced chemical kinetics models used in combustion modeling applications is urgently needed. No database devoted to chemical kinetic models is readily available, nor is any organization known to be assembling such as database, although individual sites include collections of a number of models.

Currently, no real standards for nomenclature, notation, and traceability exist. The absence of such standards and the absence of a central data repository prevents facile comparison of models developed by different researchers. These absences hamper efforts to determine why two models, for example, may predict the same results under one set of conditions, yet diverge as conditions change. Such comparisons are essential for identifying the absence of important elementary reactions and presence of inaccurate rate coefficients. Creation of a detailed chemical kinetic model database will benefit all combustion modelers — and ultimately industry — through rapid dissemination of improved models.

The NIST "Real Fuels" Detailed Chemical Kinetic Combustion Model Database will provide the combustion community with an online centralized source for detailed chemical kinetic models, along with supporting data and relevant information. The database will accelerate research directed to model optimization by standardizing nomenclature, notation, traceability, and communication. This unified Web site is currently in its developmental stage, and NIST requests comments from the community to refine and improve its content, features, and capabilities.

Related Efforts

The NIST "Real Fuels" Detailed Chemical Kinetic Combustion Model Database is one of a set of tools under development throughout the kinetic modeling community that are directed at next-generation predictive reaction modeling capabilities. For example, a software package at MIT called RIOT (Range Identification and Optimization Tool for Kinetic Modeling) has been developed to aid in kinetic model reduction tasks.² Another software tool for reaction mechanism development and reduction is MECHMOD.³ PrIME

(Process Informatics Model) is an important community effort directed at creating a framework for community-wide development of predictive reaction models that are widely agreed upon, as well as a thermochemical, chemical kinetic, and validation/target data warehouse of information.⁴ Successfully applying such tools requires a computer infrastructure to facilitate their implementation and integration. The Collaboratory for Multi-Scale Chemical Science (CMCS), sponsored by the U.S. Department of Energy with participation by many scientists throughout the United States, is developing such a capability.⁵ The online "Real Fuels" Detailed Chemical Kinetic Combustion Model Database is intended to facilitate collaboration among the community and to be integrated into the developing infrastructure.

Implementation Issues

A number of problematic issues with regard to implementation must be addressed in establishing a database for detailed chemical models, along with supporting data and information. For example, in general, no real standards for nomenclature, notation, and traceability exist that are commonly and universally employed in detailed chemical kinetic models. The models and data to support the models are often in many places (published, unpublished, online) and are often in many different formats. At times, adequate documentation with regard to the thermochemical and chemical kinetic parameters used in the model, the "pedigree" of the data, and the range of conditions for which they are valid is lacking.

Results and Discussion

The NIST "Real Fuels" Detailed Chemical Kinetic Combustion Model Database Web site,⁶ which is currently under development, is contains a number of different sections.

The Overview section provides information regarding the data contained within the site, the organization of the data, and a brief description of the history and relevance of the site. This section also provides links to related sites at NIST and elsewhere. The "Conventions Used" subsection provides a list of standard definitions, along with more detailed descriptions and examples, for chemical terminology relevant to aspects of this database. These definitions were adapted from a number of sources, including the *IUPAC Compendium of Chemical Terminology (Gold Book)*.⁷ In the field of chemical kinetics (and other fields), many "disagreements" often occur simply because one person is using a loose colloquial definition of a term, while another is using a more precise, standard definition. This list provides ready access to standard definitions and gives examples relevant to information contained in the database.

The Models section allows users to obtain (or provide) descriptive information about specific chemical kinetic combustion models and download (or upload) archival "flat file" listings of reaction sets. The goal is to have a number of well-documented annotated models, each of which can be perused with regard to similar or related reactions, references, and other relevant information. This section also includes a list of other models for many different systems that are available for archival purposes. The models systems are divided into general classes, (e.g., alkanes, aromatics, oxygenates, real fuels) and then further subdivided into individual systems (e.g., methane, butane, toluene, ethanol, dimethyl ether, JP-10).

The Reactions section includes model reaction sets that can be perused with regard to similar or related reactions, references, and other relevant information. The user will be able to search for all reactions in a particular detailed chemical kinetic model, compare forward and reverse rate expressions for specific reactions, compare rate expressions for reaction classes in a particular model and for specific reactions between different models, and compare rate

expressions in a model with data contained in the NIST Chemical Kinetics Database.⁸ Each reaction will include links to information about molecular properties, thermochemical, and other data for any species in a reaction. Some of this information will be contained directly in this database, and other information is provided simply through links to other databases at NIST (such as the NIST Chemistry Webbook⁹) or elsewhere. Other features include identification of the data type for a particular rate expression and a link to a citation for a particular rate expression in the bibliographic portion of the database. An important feature is the classification of the reactions by reaction type (*e.g.*, C-H abstraction by OH). This feature facilitates comparison (and error checking) of rate expressions that are (or should be) similar.

The Species section allows users to browse and search species by type (*e.g.*, normal alcohols, sec-alkenyl radical). For example, hydrocarbon-based systems are subdivided into acyclic aliphatics, cyclic aliphatics, and aromatics. They are then further subdivided into alkynes, alkenes, and alkanes, and then branched species. Oxidized hydrocarbons are subdivided into carboxylic acids, aldehydes, alcohols, etc. and then further subdivided based on other functionalities in the molecules. Another feature in this section is a simplified notation scheme for Polyaromatic Hydrocarbons (PAH's) that enables searching for PAH's by visually oriented structural patterns. In this section, a "species translator" is also provided for the *ad hoc*, pseudo-trivial, and often cryptical symbols commonly used to represent molecules in detailed chemical models.

The Bibliographic section supports data contained elsewhere in the database and contains references pertaining to hydrocarbon combustion and relevant detailed chemical kinetic models, molecular and physical properties, thermochemical data, and chemical reaction rate data.

Summary

The NIST "Real Fuels" Detailed Chemical Kinetic Combustion Model Database, which is currently under construction, will provide the modeling community with a centralized source for detailed chemical kinetic models. In addition to the ability to simply download archival "flat file" listings of reaction sets (largely the current practice), the database will also provide more descriptive information about each model along with supporting data. An additional feature will be the ability to upload detailed models and supporting information, enabling efficient dissemination of improved models throughout the community. A particularly important emphasis of this database is the promotion of standards for nomenclature, notation, traceability, and communication in the modeling community. This database will accelerate research directed toward model optimization and the development of next-generation, robust, validated models for use in combustion and other applications.

NIST requests comments from the community to refine and improve the content, features, and capabilities of the "Real Fuels" Detailed Chemical Kinetic Combustion Model Database.

References

- (1) Tsang, W.; Hudgens, J.W.; Allison, T. C.; Burgess, D. R., Jr.; Manion, J. A.; Matheu, D. M.; *Workshop on Combustion Simulation Databases for Real Transportation Fuels* (National Institute of Standards and Technology, Gaithersburg, MD 20899, September 4-5, 2003), NISTIR 7155.
- (2) Bhattacharjee, B.; Schwer, D. A.; Barton, P. I.; Green, W. H. ; *Combust. Flame*, **2003**, *135*, 191-208.
- (3) Tomlin, A. S.; Turanyi, T.; Pilling, M.J. In *Comprehensive Chemical Kinetics. Low Temperature Combustion and Autoignition*; Pilling, .M. J. and Hancock, G., Eds.; Elsevier, Amsterdam, 1997; pp. 293-437.
- (4) PrIme (Process Informatics Model). <http://www.me.berkeley.edu/prime/>

- (5) CMCS (Collaboratory for Multi-Scale Chemical Science). <http://cmcs.org/>
- (6) NIST Detailed Chemical Kinetic Combustion Model Database. <http://kinetics.nist.gov/realfuels/>
- (7) McNaught, A. D.; Wilkinson, A.; *IUPAC Compendium of Chemical Terminology (Gold Book)*, Blackwell Science: Oxford, 1997.
- (8) NIST Chemical Kinetics Database. <http://kinetics.nist.gov>
- (9) NIST Chemistry Webbook. <http://webbook.nist.gov>

DENSITY FUNCTIONAL TIGHT BINDING (DFTB) METHOD AND ITS APPLICATION TO MOLECULAR DYNAMICS SIMULATION OF FORMATION OF FULLERENES AND CARBON NANOTUBES

Stephan Irle,^a Guishan Zheng,^a Henryk Witek,^a Keiji Morokuma,^a
and Marcus Elstner^b

^aCherry L. Emerson Center for Scientific Computation and
Department of Chemistry, Emory University, Atlanta, GA 30322

^bFachbereich Physik, Universität Paderborn, 33095 Paderborn,
Germany

Introduction.

Carbon nanostructures today are the most intensively researched species in the context of molecular engineering on the nanometer scale, with the widest range of promising applications in materials science, molecular electronics, and molecular machinery. Elementary building blocks are all members of the third allotrope form of carbon, namely fullerene cages and carbon nanotubes. From these zero- and one-dimensional units it is hoped that two- and three-dimensional structures can be readily engineered with atomic precision to create any kind of desirable material or objects on the nanoscale, thereby extending the range of traditional chemistry to true molecular manufacturing. Fullerenes and carbon nanotubes are made by methods as diverse as carbon arc, laser evaporation, chemical vapor decomposition, and combustion of aromatic hydrocarbons. It is generally believed that self-assembly mechanisms¹ will play a very important role besides more cumbersome positional assembly in the manufacturing processes of complex carbon nanostructures.² However, at present it remains unclear what the nature of these mechanisms are, and how one could apply them in practical applications. A deep, atomic level understanding of the behavior of carbon clusters at high temperatures is a vital prerequisite to formulate pathways controlling self-assembly processes required for molecular engineering and an imperative requirement for making carbon nanostructures integral part of industrial material sciences. For MD studies of fullerene formation and nanotube growth mechanism, reactive molecular mechanics force fields, such as the Reactive Empirical Bond Order (REBO) method,³ has typically been used. This kind of force field, different from standard force field methods, allows the breaking and formation of chemical bond by adopting More-type dissociative bond functions. However, the effects of π electron conjugation are completely neglected. Such an effect is essential for the description of π -conjugated system, since, as is well known, this effect determines the reactivity of conjugated hydrocarbons. The conjugation effect cannot be described by classical molecular mechanics force fields but requires quantum mechanics to predict accurate chemistry of aromatic carbon systems.

First principle quantum mechanical methods are in general several orders ($\sim 10^6$) of magnitude more expensive than force field methods. It is still almost impossible to run long time ($>ps$) simulations for systems containing tens and hundreds of carbon atoms. There are several semi-empirical methods, such as AM1 and PM3, that are often used in nanostructure simulations. However, we found in our comparative studies of stability of isomers of C_{28} cluster, these methods give very poor correlation with the B3LYP density functional method with a correlation coefficient around 0.3.⁴ We felt that even qualitative conclusions derived from these methods are not reliable.

Meanwhile we paid attention to the density functional tight binding (DFTB) method developed by Frauenheim, Elstner and others.⁵ DFTB is an extended Hückel-type two-center approximation

to density functional theory (DFT), using a minimum basis set in combination with atomic and diatomic potentials obtained from high level DFT calculations DFTB has been successfully used in the past to explain relative stabilities of fullerene isomers and aggregates.⁶ We have compared the results of DFTB calculations for C_{28} with the B3LYP results, where the correlation coefficient of 0.75 was obtained,⁴ much better than the other semiempirical methods. The cost of DFTB is a few orders of magnitude ($\sim 10^3$) more expensive than the molecular mechanics but is a few orders of magnitude ($\sim 10^3$) less expensive than the DFT. Therefore this method is ideally suited for the dynamics of conjugated systems, and we decided to adopt the DFTB method for the simulation of the fullerene and carbon nanotube formation. Toward this end, we have made substantial efforts in improving the method, by introducing the analytical second derivative, writing a new code for Gaussian, refitting some parameters to improve the vibrational frequencies and adding parameters for various transition metals.

In the present presentation, we will at first review our recent developments in the DFTB methods, codes and parameterization and then discuss applications to the fullerene formation mechanism as well as recent progress in the nanotube growth mechanism.

Density Functional Tight Binding (DFTB) Method

The SCC (self-consistent charge)-DFTB energy expression is given by

$$E^{\text{SCC-DFTB}} = \sum_i n_i \langle \varphi_i | \hat{H}^0 | \varphi_i \rangle + \frac{1}{2} \sum_{A,B}^{AT} \gamma_{AB} \Delta q_A \Delta q_B + E_{\text{rep}}, \quad (1)$$

where φ_i is an SCC-DFTB molecular orbital, n_i is its occupation number, Δq_A is the induced charge on an atom A , γ_{AB} is a charge-charge interaction function, and E_{rep} is a sum of core-core repulsive potentials. The first sum runs over all molecular orbitals, and the second sum, over all atoms. The operator \hat{H}^0 stands for the effective Kohn-Sham Hamiltonian, which depends only on the reference density ρ_0 :

$$\hat{H}^0 = -\frac{1}{2} \nabla^2 - \sum_K^{AT} \frac{Z_K}{|\vec{R}_K - \vec{r}|} + \int \frac{\rho_0(\vec{r}')}{|\vec{r} - \vec{r}'|} d\vec{r}' + V_{\text{xc}}[\rho_0(\vec{r})]. \quad (2)$$

In Equation (2), Z_K is the charge and \vec{R}_K is the position of the K th nucleus, and V_{xc} represents the exchange-correlation potential. The SCC-DFTB molecular orbitals φ_i and induced charges Δq_A in Eq. (1) are determined by solving a generalized SCC-DFTB eigenvalue problem given by

$$\mathbf{H}\mathbf{C} = \mathbf{S}\mathbf{C}\mathbf{e}, \quad (3)$$

where \mathbf{C} denotes the matrix of expansion coefficients of the molecular orbitals (MO) in the basis of atomic orbitals (AO),

$$\varphi_i = \sum_{\mu}^{AO} c_{i\mu} \chi_{\mu}, \quad (4)$$

and \mathbf{S} and \mathbf{H} are the AO overlap matrix and the AO Hamiltonian matrix, respectively. \mathbf{S} and \mathbf{H} are given by

$$S_{\mu\nu} = \langle \chi_{\mu} | \chi_{\nu} \rangle \quad (5)$$

$$H_{\mu\nu} = \langle \chi_{\mu} | \hat{H}^0 | \chi_{\nu} \rangle + \frac{1}{2} S_{\mu\nu} \sum_K^{AT} (\gamma_{MK} + \gamma_{NK}) \Delta q_K, \quad (6)$$

where M and N are the atoms on which the orbitals χ_{μ} and χ_{ν} , respectively, are centered.

We have recently implemented analytical geometrical second derivative and the numerical derivative of analytical gradient with respect to external electric field.⁷ The calculated vibrational frequencies and infrared and Raman intensities are in good agreement with experiment.⁸ Improvement in the functional fit of

diatomic repulsive parameters resulted in substantially better vibrational results with little change in geometry.⁹ Only a few transition metals were parameterized previously. We have recently determined and tested parameters for many first row transition metals with HCNOPS atoms.¹⁰ The results will be presented in the talk.

DFTB Molecular Dynamics Simulation of Fullerene Formation from Small Carbon Fragments.

The Role of π -Conjugation and Aromatic Stabilization. Previous molecular dynamics (MD) simulation of fullerene formation mechanism based on the REBO molecular mechanics potential showed that fullerene formation occurs on the order of nanoseconds, without occurrence of long carbon chains,¹¹ which are believed to be major player in high temperature carbon chemistry due to their high entropy. On the contrary, carbon polyene chains are frequently observed in DFTB-based quantum mechanical QM/MD calculations at high temperatures. For instance, we ran trajectories for open-ended achiral and chiral carbon nanotubes with various tube lengths at 1000-5000 K.^{4,12} Besides Stone-Wales rearrangements, we find particularly that acetylenic “wobbling C_2 units” and longer fragments up to C_4 emerge frequently at the open ends, standing upright from the SWNT rims due to their sp-hybridization and making contact with defect structures (other wobbling C_2 units or 10-membered macrocycles created from adjacent 5- and 7-membered rings) on the opposite site of the opening, leading eventually to rapid tube closure within typically 14 picoseconds. We noted that once a structural defect like C_2 creation occurs, π -delocalization in that region of the opening is decreased, and more bonds are likely to break in its vicinity. At final stages of tube closure, [2+4] cycloaddition “zipper” type reactions occur when the opening size has been reduced and only consists of 12-membered. None of these reactions could be observed when similar trajectories were run using the REBO potential; instead, unreasonable transformation in the center parts of the tubes were observed which prolonged the tube closing processes substantially into the nano second regime. Obviously, quantum mechanical delocalization effects play a synergetic effect in carbon chemistry that cannot be accounted for without electronic structure calculations.

The Role of Open Environment in QM/MD Simulations.

Several mechanisms for the formation of fullerenes have been proposed in the literature, e.g. party line, fullerene road, pentagon road, etc. All of them are merely guesswork and share the assumption of an underlying principal of orderly growth by which fullerene molecules are systematically constructed. However, under experimental conditions of fullerene formation, a constant flow of carbon material can be expected, forcing initially formed carbon clusters constantly out of thermodynamic equilibrium. We model such an open environment by adding more C_2 units to a trajectory when an equilibrium state is reached with no further apparent structural reorganization.¹³ Temperature is kept constant at 2000 K or 3000 K using a scaling of velocities thermostat. It is found that the gradual addition of C_2 is essential for the formation of a significantly curved carbon cluster, and three stages of fullerene growth can be identified under non-equilibrium conditions: *nucleation* of polycyclic structures from entangled carbon chains, *growth* by ring condensation of carbon chains attached to the hexagon and pentagon containing nucleus, and at final stages *cage closure* similar to the mechanisms observed for the transformation of open-ended carbon nanotubes to fullerenes (see Figure 1). Driving force behind the growth of the curved carbon sheet is increasing π -delocalization.

The “Size-up” Approach. We call the previously described self-assembly of fullerenes from small carbon fragments the “size-up” approach, and in dependence on initial *carbon densities*,

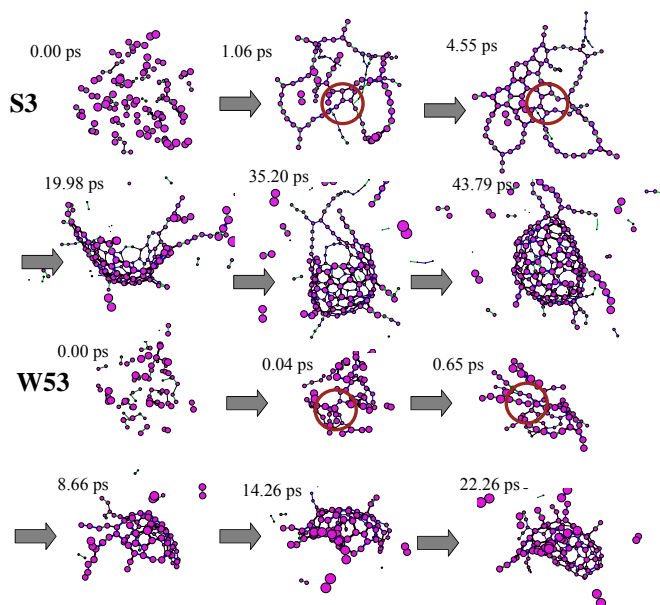


Figure 1. Snapshots for two successful trajectories for fullerene formation from C_2 molecules using different carbon densities. The **S3** trajectory¹³ starts at 0.09 g/cm³ and leads to a C_{146} cage, **W53**¹⁴ starts at 0.20 g/cm³ and leads to a C_{82} cage.

different size and formation time domains of self-assembled fullerenes are observed.¹³ In Ref. 13 our QM/MD simulations led only to the formation of so-called “giant fullerenes”, namely C_{146} , C_{184} , and C_{208} by self-assembly from ensembles of C_2 molecules. Starting at higher carbon densities reduced the size of resulting fullerenes down to C_{72} .¹⁴ With the higher carbon density, long linear or branched carbon chains appearing at initial stages of the trajectories become more entangled, which is crucial for two reasons: a) formation of a nucleus of polycyclic structures, and b) formation of a 3D-scaffold along which ring-condensation growth can occur subsequently. According to these observations, carbon density can therefore be considered as a possible environmental factor that can possibly be optimized and tuned to achieve size-selective fullerene synthesis. Somewhat surprisingly, C_{60} , the most important and abundant representative of fullerenes, was still not found in our simulations, and we therefore investigated the possibility of shrinking giant fullerenes under prolonged heating as described in the next section.

The “Size-down” Approach. The five giant fullerene molecules obtained in the low-density “size-up” approach¹³ were subjected to prolonged heating at 3000 K, using only the fullerene cages plus carbon side chains directly attached to them.¹⁴ For these calculations, no periodic boundary conditions were applied. Due to the relative ease of which C_2 units can be expelled from giant fullerene cages,¹⁵ we expected to observe significant cage shrinkage, and indeed, besides “fall-off” events associated with the attached side chains, “pop-out” events are observed on the order of 1 carbon atom per picosecond. Typically, the fullerene cages are observed to be shrinking by expelling C_2 units after major cage deformations caused by excited vibrational modes. So far, we only studied trajectories up to about 40 ps, and “pop-out” events occurred only after 20 ps, therefore the appearance of C_{60} fullerene cages was not observed yet.

DFTB Molecular Dynamics Simulation of Carbon Nanotube Growth.

In the past, single-walled carbon nanotubes (SWNT) have been synthesized by various research groups mainly from pure carbon or

chemical vapor deposition of carbon-rich gases in the presence of a metal catalyst such as Fe, Co, Ni, Y, or Mo. Results vary in different experiments, even when same catalyst elements are used.¹⁶ Recently, SWNT have been synthesized without metal catalyst by laser-annealing of amorphous SiC films.¹⁷ The exact mechanism of SWNT nucleation and growth at the atomic scale is still unclear, even though advances in time-resolved *in situ* high resolution transmission electron microscopy and its applications to SWNT growth have been reported. In earlier times, a “scooter model”¹⁸ was proposed where single catalytic metal atoms move around open ends of growing SWNTs, supposedly preventing the formation of tube closure by scooting around the edge. Yudasaka *et al.*¹⁹ suggested a “metal-particle” model, in which droplets of carbon-containing catalytic metal were formed as a consequence of laser ablation and in the subsequent cooling stage the carbon atoms were separated out from the metal nuclei to form SWNTs. There are two possible scenarios to the “metal-particle” model: the “extrusion-root growth” and the “tip-growth” model, depending on whether the metal nanoparticle moves with the tip of the growing tube, or remains on the substrate. All conceptual models share the notion that nanotube growth occurs at the metal/tube interface, and that the metal serves to saturate the dangling bonds of the growing nanotube edges.

In order to verify these hypothetical models, several research groups have carried out atomic scale molecular dynamics simulations. Tight binding molecular dynamics²⁰ and *ab initio* DFT studies²¹ have been carried out on small model tubes in the presence of single catalyst atoms. But metal nanoclusters are much more difficult to model and computationally very expensive, and therefore modified versions REBO force field is typically employed as underlying potential for the dynamics. For instance, Maruyama *et al.*²² made observations along both lines of “scooter” and “metal-particle” models for systems consisting of randomly placed carbon and individual Ni metal atoms at 2500 K. Ding *et al.* studied Fe catalyzed nucleation and growth and investigated the role of the particle size for SWNT diameter distributions.²³ However, as we have shown in our previous QM/MD studies on the capping mechanism of open-ended SWNTs^{4,12} and on the growth mechanism of fullerenes,^{13,14} the inclusion of full quantum chemical potential is important to describe essential features of carbon nanochemistry such as π delocalization and aromaticity, and we demonstrated that REBO simulations predict even qualitatively inaccurate dynamics in terms of structures as well as time scale. DFTB-based QM/MD simulations is ideally suited for re-visiting the formation mechanisms of SWNTs, and we report results in the presence of Fe catalyst nanoclusters, using randomly oriented C₂ molecules. We propagate these systems in a periodic boundary box under stepwise addition of more C₂ molecules similar to our fullerene formation trajectories. We include small metal clusters with varying sizes, and investigate the effect of various temperatures ranging from 1000 to 3000 K. Similar to the studies of fullerene formation mechanisms, the accuracy of the DFTB QM/MD simulations is checked by performing B3LYP/6-31G(d) single-point energy calculations for randomly selected frames of the trajectory. In order to be able to do this accurately, the iron nanoclusters were computed themselves both at the SCC-DFTB and B3LYP/6-31G(d) level of theory. We also present results of QM/MD simulations based on controlled heating of SiC crystals in the absence of metal catalysts. A comparison between both approaches allows to shed light on the role of the catalyst nanoparticles for SWNT growth and nucleation at the atomic level.

Conclusions

The DFTB method, an extended Hückel-type method with two-center approximation in which the parameters are fitted to *ab initio*

DFT calculations, is a reasonable method for calculation of large molecular systems. It gives geometries and energies similar to the DFT results. Our recent extension of the method includes the analytical geometrical second derivatives and numerical derivatives of the analytical gradient with respect to external field. New parameters have been developed for transition metals. The DFTB method, although substantially more expensive than the MM force field, is orders of magnitude less expensive than *ab initio* DFT methods and is ideal suited for MD simulation of processes leading to the formation of fullerene and carbon nanotubes from small carbon fragments.

The concept of “self-assembly” in fullerene formation emerges somewhat surprisingly but naturally as a consequence of our non-equilibrium dynamics, and we found that fullerenes might in fact represent “frozen” dissipative dynamic carbon structures commonly found in non-linear dynamic systems, trapped by rapid cooling thanks to their kinetic stability. A “size-up” approach has been described by which fullerene molecules are formed from random ensembles of small carbon fragments in QM/MD simulations when periodically batches of C₂ units are added. Depending on the density, different sizes and formation times are observed, but so far all trajectories lead to fullerene cages larger than C₆₀. In a “size-down” approach, these giant fullerenes are exposed to prolonged heating at 3000 K, and “pop-out” events are observed, consistent with experiment. Both approaches provide an explanation for the dominant appearance of thermodynamically stable C₆₀ and the existence of larger fullerenes in experiment, and at this point it is impossible for us to provide a definitive answer as to which one of the both pathways or possibly both at the same time is actually followed.

We have shown that DFTB QM/MD trajectories, although not representing statistical ensembles, are valid exploratory tools of investigations into the dynamics of carbon clusters at high temperature, capable of detecting key features in the formation mechanisms of carbon nanostructures.

Acknowledgement. This work was partially supported by grants from the Mitsubishi Chemical Corporation and from the Petroleum Research Fund, the American Chemical Society. Acknowledgement is made to the Cherry L. Emerson Center of Emory University for the use of its resources. We also thank the Pacific Northwest National Laboratory’s EMSL for valuable computer time through its Grand Challenge project, GC3564.

References

- (1) Nicolis, G.; Prigogine, I. *Self-Organization in Nonequilibrium Systems: From Dissipative Structures to Order Through Fluctuations*; Wiley: New York, 1977.
- (2) Merkle, R. C. *Nanotechnology* **2000**, *11*, 89.
- (3) Brenner, D. W. *Phys. Rev. B* **1990**, *42*, 9458.
- (4) Zheng, G.; Irle, S.; Elstner, M.; Morokuma, K. *J. Phys. Chem. A* **2004**, *108*, 3182.
- (5) Seifert, G.; Porezag, D.; Frauenheim, T. *Int. J. Quantum Chem.* **1996**, *58*, 185; Elstner, M.; Porezag, D.; Jungnickel, G. *Phys. Rev. B* **1998**, *58*, 7260.
- (6) Fowler, P. W.; Heine, T.; Rogers, K. M. *Chem. Phys. Lett.* **1999**, *300*, 369; Fowler, P. W.; Heine, T.; Mitchell D. *J. Chem. Soc. Farad. Trans.* **1996**, *92*, 2203.
- (7) Witek, H. A.; Irle, S.; Morokuma, K. *J. Chem. Phys.* **2004**, *121*, 5163.
- (8) Witek, H. A.; Morokuma, K. *J. Comp. Chem.* **2004**, *25*, 1858; Witek, H. A.; Morokuma, K.; Stradomska, A. *J. Chem. Phys.* **2004**, *121*, 5171.
- (9) Witek, H. A.; Malolepsza, E.; Morokuma, K. in preparation.

- (10) Zheng, G.; Irle, S.; Elstner, M.; Morokuma, K. in preparation.
- (11) Chelikowsky, J. R.; *Phys. Rev. B* **1992**, *45*, 12062; Maruyama, S.; Yamaguchi, Y. *Chem. Phys. Lett.* **1998**, *286*, 343; Yamaguchi Y.; Maruyama, S. *Chem. Phys. Lett.* **1998**, *286*, 336.
- (12) Irle, S.; Zheng, G.; Elstner, M.; Morokuma, *Nano Lett.* **2003**, *3*, 465.
- (13) Irle, S.; Zheng, G.; Elstner, M.; Morokuma, K. *Nano Lett.* **2003**, *3*, 1657.
- (14) Zheng, G.; Irle, S.; Elstner, M.; Morokuma, K. *J. Chem. Phys.* in press.
- (15) O'Brien, S. C.; Heath, J. R.; Curl, R. F. *J. Chem. Phys.* **1988**, *88* 220.
- (16) Journet, C.; Bernier, P. *Appl. Phys. A.* **1998**, *67*, 1.
- (17) Kusunoki, M.; Rokkaku, M.; Suzuki, T. *Appl. Phys. Lett.* **1997**, *71*, 2620. Kusunoki, M.; Suzuki, T.; Hirayama, M.; Shibata, N.; Kaneko, K. *Appl. Phys. Lett.* **2000**, *77*, 531. Botti, S.; Ciardi, R.; Terranova, M. L.; Piccirillo, S.; Rossi, M.; Vittori-Antisari, M. *Appl. Phys. Lett.* **2002**, *80*, 1441. Botti, S.; Asilyan, L. S.; Ciardi, R.; Fabbri, F.; Loreti, S.; Santoni, A.; Orlanducci, S. *Chem. Phys. Lett.* **2004**, *396*, 1.
- (18) Thess, A.; Lee, R.; Nikolaev, P.; Dai, H.; Petit, P.; Robert, J.; Xu, C.; Lee, Y.H.; Kim, S. G.; Rinzler, A. G.; Colbert, D. T.; Scuseria, G. E.; Tomanek, D.; Fischer, J. E.; Smalley, R. E. *Science* 1996, **273**, 483.
- (19) Yudasaka, M.; Yamada, R.; Sensui, N.; Wilkins, T.; Ichihashi, T.; Iijima, S. *J. Phys. Chem. B* **1999**, *103*, 6224.
- (20) Andriotis, A.N.; Menon, M.; Froudakis, G. *Phys. Rev. Lett.* **2000**, *85*, 3193.
- (21) Lee, Y.H.; Kim, S.G.K.; Tomanek, D. *Phys. Rev. Lett.* **1997**, *78*, 2393.
- (22) Shibuta, Y.; Maruyama, S. *Chem. Phys. Lett.* **2003**, *382*, 381.
- (23) Ding, F.; Bolton, K.; Rosen, A. *J. Vac. Sci. Technol. A* **2003**, *22*, 1471. Ding, F.; Rosen, A.; Bolton, K. *J. Chem. Phys.* **2004**, *121*, 2775. Ding, F.; Rosen, A.; Bolton, K. *Chem. Phys. Lett.* **2004**, *393*, 309.

NANOPARTICLE AGGLOMERATION

Angela Violi, Sergey Izvekov, Gregory A. Voth

Department of Chemical Engineering
Department of Chemistry
University of Utah
1495 E 100 S
Salt Lake City, UT 84112

Introduction

Previous results from this group have shown the importance of using atomistic methods to characterize the growth of hydrocarbon molecules up to sizes of nanoparticles in flames. In particular KMC and MD methodologies have been employed (AMPI code) to study relationships between structure and pathways, structure and properties, and structure and reactivity (accessibility) of nanostructures.¹⁻²

The use of atomistic simulations allows us to follow the transformations that occur during nanoparticle formation in combustion environments in a chemically specific way, providing information on both the final chemical structure and the configuration of the nanoparticles and young soot particles. This approach provides a connection between the various time scales in the high molecular mass compound growth problem, together with an unprecedented opportunity for the understanding of the atomistic interactions, and underlying carbonaceous nanoparticle structures and growth. The coupling between the KMC and MD modeling approaches provides a key to the multiple time-scales involved in the formation of nanoparticles, spanning pico- or nanoseconds for intramolecular processes that can occur for example on a particle surface to milliseconds for intermolecular reactions. The capability of the AMPI code has been validated in different combustion conditions. Nanoparticles have been characterized in terms of chemical structure/components and relationships between structure and pathways, structure and properties, and structure and reactivity population of active sites have been addressed. In particular, computed properties of nanoparticles have been compared with experimental data in terms of H/C trends, particle morphology and depolarization ratio, and free radical concentration.

In order to study nanoparticle interactions, their agglomeration and further growth to soot, a different approach needs to be used. The nanoparticle assemblies are influenced by large length and time scale motions, that extend to mesoscopic scales, i.e., hundreds of nanometers or more in length and one microsecond or more in time. These mesoscales do not fit into an atomistic MD simulation. In addition, carbonaceous nanoparticles assembly will also cause significant structural and dynamical effects that will propagate upward in scale, both in length and in time. To deal with this problem, a common solution is coarse graining the atomistic region. In essence, coarse graining introduces constraints among the atomic coordinates that reduce the number the degrees of freedom of the system.

In this paper we report preliminary results obtained using MD for nanoparticles agglomeration that highlight the influence of particle morphology on clustering behaviors. The results obtained using atomistic MD will be compared with those obtained coarse-graining the systems. The reason for doing so is to identify a good method to run MD simulation on big systems and for long time.

Method

A new and unique approach for the coarse-graining allows the length and time scales of the simulations to be increased by a factor

of 10 – 100. The force-match method used in the present paper is described in detail in Ref. 3³ The method is a variant of the force-matching approach originally proposed by Ercolessi and Adams⁴ and can be applied if a force field depends linearly on the fitting parameters. In this case the problem of finding the best least-squares fit to configuration and force data can be accomplished through the solution of an overdetermined system of linear equations.

In the “multi-scale coarse-graining” methodology (MCG) the effective forces between whole groups of atoms in the condensed phase molecular system are mapped into much simpler effective forces for coarse-grained “sites” on the molecules (or nanoparticles). These resulting forces are, in effect, the potential of mean forces between the coarse-grained sites (i.e., groupings of atoms). As a result, the effective phase space of the system is significantly reduced in size, as are the number of costly long-ranged electrostatic calculations. The method is based on a least squares algorithm which, when combined with simple empirical functional forms for the coarse-grained force field, yields an over-determined set of linear equations that can be solved repeatedly through singular-value decomposition and block averaged over a reasonably short fully atomistic MD trajectory (usually under 100 ps).

In the multi-scale coarse-graining approach the CG parameters are instead developed “on the fly” from the actual atomistic-level forces coming from a relatively short full MD “pre-simulation.” Hence, the term “multi-scale” is used for the MCG method, meaning that changes at the atomistic level of the force field will systematically propagate upward via the FM algorithm to the CG representation of the system.

The method can be applied to parameterize the classical force field if it is linearly dependent on the parameters, a property which can be achieved by using proper interpolation.

Results and Discussion

The AMPI code has been previously used to simulate the formation of nanoparticles in aromatic and aliphatic low-pressure laminar flames. The results have shown that the aromatic growth process strongly depends on the specific local environment, which is characterized by several experimentally measured properties, such as temperature, concentration of hydrogen, polycyclic aromatic hydrocarbons (PAH), etc., and this work reveals in the influence of different environments on structural properties of the compounds formed. In the case of aromatic fuels, polymerization reactions can occur early since aromatic compounds are in relatively large concentrations in the fuel, whereas in the case of aliphatic fuels such as acetylene, ethylene, or methane the first aromatic ring must be formed from fuel decomposition products by a sequence of elementary reactions and therefore the concentrations of aromatic soot precursors are in lower concentrations than in the aromatic flames. The structures formed in the aromatic flame shows a high degree of curvature, as a consequence of dehydrogenation reactions and ring closure leading to 5-membered rings, whereas the particle formed in an acetylene environment has less curvature than that produced in a benzene environment.

These two environments have here been used to study nanoparticle agglomeration. **Figure 1** shows results from MD simulation in aromatic and aliphatic flames (left and right panel respectively). In benzene flames, the round particles tend to cluster and they show a preferred orientation, that is back to back. The sheet-like particles produced in the acetylene flame show a different behavior: some of them drift away from the ensemble, some do cluster in small agglomerates. The clustering behavior for aliphatic particles is pretty different from the aromatic environment: the orientation is more edge to edge or stacking and the interacting

particles are tightly constrained. Therefore, the agglomeration behavior of nanoparticles is influenced by their morphology. And this information needs to be carried out to build a realistic model for soot formation.

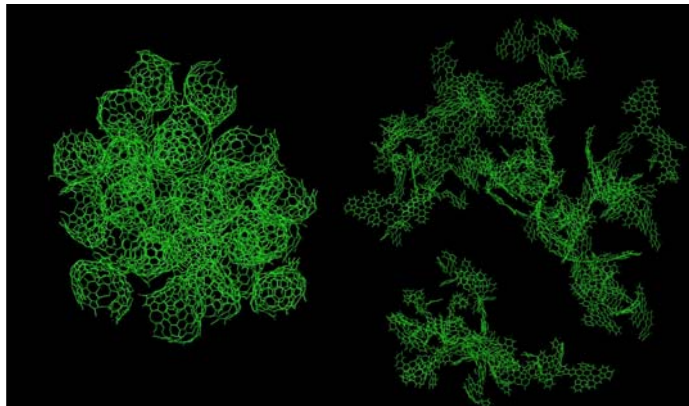


Figure 1. Nanoparticle agglomeration in an aromatic flame – left and in an aliphatic flame – right panel.

As second part of this work, we coarse grained the system and built a potential to describe the interaction of CG centers. In the

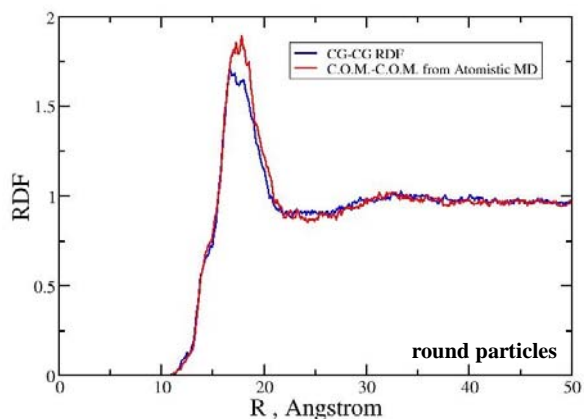


Figure 2. Comparison between RDF computed with the fully atomistic MD –red line- and the one obtained with CG MD –blue line.

aromatic flame, we replaced the round particle with its center of mass (one site model) and ran MD simulations of the system. **Figure 2** shows the comparison between the radial distribution function (RDF) obtained with the fully atomistic MD and the one computed using the one-site model CG. The results are virtually the same.

For the aliphatic flames, we developed a three site model to represent the nanoparticles (See **Figure 3**). **Figure 4** shows the comparison between RDF computed with fully atomistic MD and the

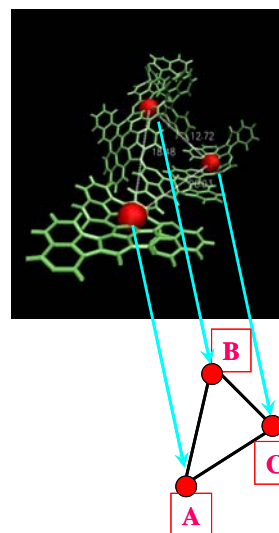


Figure 3. The three site model for flat nanoparticles

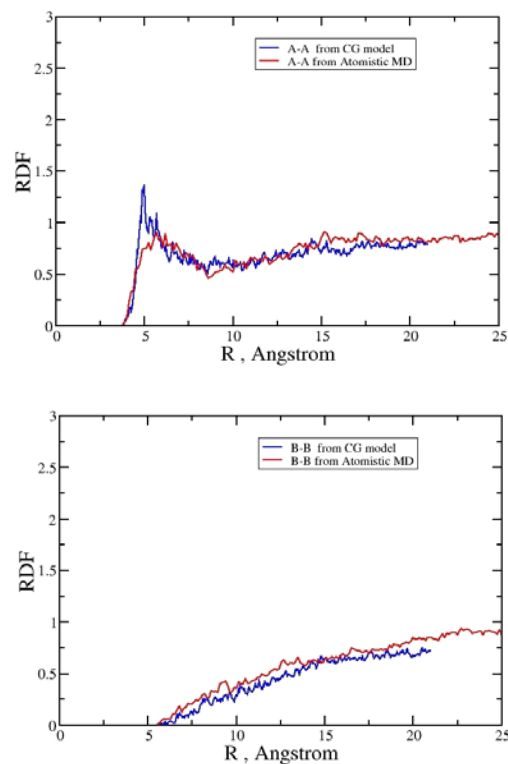


Figure 4. Comparison between RDF obtained with fully MD and the CG MD with the three-site model.

Conclusions

Preliminary results have been reported for the agglomeration of nanoparticles using Molecular Dynamics. The clustering behavior is highly dependent on the morphology of the nanoparticles. Molecular Dynamics calculations of the coarse-grained systems show results in terms of RDF that agree very well with the fully atomistic calculations. These results are very encouraging since allow us to

extend our calculations of MD to longer time scales and bigger length scales. The knowledge of the structures of soot precursors, obtained with these atomistic methods can supply valuable guidance to the development of soot formation models.

Acknowledgment. This research is funded by the University of Utah Center for the Simulation of Accidental Fires and Explosions (C-SAFE), funded by the Department of Energy, Lawrence Livermore National Laboratory, under subcontract B341493, and by a National Science Foundation Nanoscale Interdisciplinary Research Team grant (EEC-0304433).

References

- ¹ Violi A., Comb. Flame in press (2004).
- ² Violi A., Sarofim A.F., Voth G.A. Comb. Sci. Tech 175(5-6): 991 (2004).
- ³ Izvekov S., Parrinello M., Burnham C.J., Voth G.A., *J. Chem. Phys* 120 (23): 10896 (2004).
- ⁴ F. Ercolessi and J. Adams, Europhys. Lett. **26**, 583 (1994).

USING COMPUTATIONAL METHODS TO GAIN INSIGHT INTO MERCURY CHEMISTRY IN FLUE GAS

Jan Steckel

National Energy Technology Laboratory, Pittsburgh, PA 15236
and Parsons, South Park, PA 15236

Introduction

This work centers on using quantum chemical methods to characterize reactions of mercury of importance to the mercury removal program at NETL. Mercury is a hazardous metal and is present in coal and at ppb concentrations in the flue gas of coal fired power plants. Efforts are underway to devise cost-effective methods to remove mercury from flue gas.

Calculations involving mercury are quite challenging, due to a host of reasons. Mercury possesses 80 electrons, making the use of a pseudopotential practically mandatory except for diatomics or small models. Relativistic effects cannot always be neglected in mercury chemistry, but thorough and accurate methods for fully relativistic calculations are not widely available, nor are these practical for large models. For open shell systems or excited states, spin orbit coupling effects are likely to be significant.

However, the need for accurate calculations and an increased understanding of mercury chemistry is quite urgent. There are a large number of fundamental questions involving mercury chemistry that may be addressed using computational methods, albeit in a slightly approximate way at present.

Mercury interacts with activated carbon and with coal, but very little is known about these important interactions. Activated carbon is particularly important because it is already employed as a means for cleaning mercury out of the flue gas of power plants. There are conditions under which activated carbon has been shown to perform very well. However, operating conditions of power plants and the variety of coals used tend to make conditions widely variable in the flues of power plants. If the interaction were better understood, it is possible that the performance of activated carbon could be controlled more effectively. In this paper, we present results for the interaction of mercury with benzene, as a model interaction between mercury and activated carbon or coal. Both coal and activated carbon have substantial graphitic portions.

It is known that mercury interacts with metal surfaces of various types; the strong interaction of mercury with gold, for example, is used in certain types of mercury detection devices. In addition, it has been noted that models based on homogeneous oxidation alone do not do a good job of describing the speciation and reaction kinetics of mercury oxidation in flue gas. It is likely that heterogeneous oxidation is playing a role and metal surfaces may play a crucial role.¹ Several surfaces can be identified as important either because they have been used in experimental studies or because they might be useful in industrial scale Hg-removal schemes. Pd, Cu, Ag and Au are among metals that might provide a catalytic surface for Hg oxidation.

Ab initio calculations of Hg-benzene interactions

Calculations of interactions between Hg and benzene have been carried out at MP2 and higher levels of theory. Hg may interact with benzene in several fashions: the Mulliken outer pi (η^6), a pi complex (η^2), and the sigma complex (η^1).

¹(Hg-benzene) Mulliken outer pi (η^6) complex. In the singlet ground state, benzene and Hg form a neutral complex in which Hg interacts with all six C atoms in the ring (**Figure 1**). CCSD(T) calculations have been carried out using the large-core quasi-relativistic pseudopotential of Küchle et al.² and the basis set of

Czuchaj et al.³ with the addition of 3f and 2g functions. The basis set used for the C and H atoms is Dunning's valence triple zeta.⁴ These calculations have been carried out with the Molpro package.⁵ Higher angular momentum basis functions have been shown to be important for the accuracy of calculations of weak interactions involving mercury; for example in the mercury dimer.⁶ Another consequence of the weakness of this interaction is that basis set superposition error can be significant; in the current calculations the BSSE is estimated to be 0.05 eV. The counterpoise corrected interaction energy is -0.15 eV. In the minimum energy configuration the Hg atom is positioned 3.3 Å above the plane of the benzene ring.

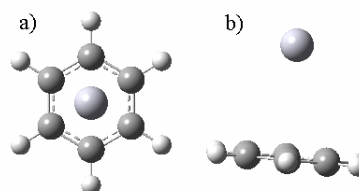


Figure 1. The Mulliken outer pi (η^6) complex pictured from the top (a) and from the side (b).

²(Hg-benzene)⁺ cationic complex. UMP2 calculations have been carried out on the cationic complex between Hg and benzene. In this case, the small core quasi-relativistic pseudopotential of Andrea *et al.*, which is based on relativistic Dirac-Fock all-electron calculations, has been used.⁷ For these calculations we have made use of the double-zeta quality (7s7p6d2f)/[4s4p3d2f] correlation consistent basis set for Hg developed by Peterson.⁸ For the C and H atoms, the 6-311G(d) basis set was used. The Gaussian 03 program has been used.⁹

In this cationic complex, the minimum energy structure is a pi-bonded (η^2) structure (**Figure 2**) with an interaction energy of -2.18 eV. A sigma-bonded (η^1) transition state (**Figure 3**) lies only 0.3 eV above the ground state and a (η^6) saddle point lies only 0.79 eV higher than the ground state. The characterization of these stationary points has been determined via frequency calculations at the UMP2 level.

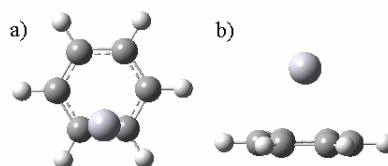


Figure 2. The pi (η^2) complex pictured from the top (a) and from the side (b). The distance from the Hg atom to the two nearest C atoms is 2.50 Å.

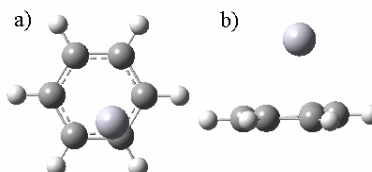


Figure 3. The sigma (η^1) complex pictured from the top (a) and from the side (b). The distance from the Hg atom to the nearest C atom is 2.49 Å.

³(Hg-Benzene) Pi (η^2) complex. UMP2 calculations have been carried out to characterize the pi complex of Hg with benzene in the triplet state with pseudopotential and basis sets as above. This neutral complex is not stable in the ground state, but the triplet state appears to be stable. Calculations on this state are ongoing, but

preliminary results indicate that the triplet state is bound by as much as -1.28 eV at the UMP2 level of theory. This compares to the outer pi Mulliken complex for neutral ¹(Hg-benzene), which is bound by only -0.34 eV at the MP2 level of theory, and to the pi complex for ²(Hg-benzene)⁺, which is bound by -2.18 eV. The structure of the triplet state appears similar to that of the pi (η²) complex of the cation (**Figure 2**), except that the Hg-C distances are shortened (2.47 Å for the triplet as compared to 2.50 Å for the cation) while the C-C bond distance is lengthened (1.56 Å for the triplet as compared to 1.43 Å for the cation).

The reason for the stability of this edge-bonded triplet state appears to be increased orbital overlap of the 6p orbital of Hg with the highest occupied pi orbital of benzene, that with a nodal plane perpendicular to the plane of the benzene ring. Singlet Hg has no orbital with the correct symmetry to mix with this orbital.

Density functional theory calculations of Hg on metal surfaces

Density functional theory calculations are underway to describe the bonding of Hg to various metal surfaces, including Cu, Pd, Ag and Au. Fully relativistic, all electron, density functional calculations have been carried for small models (~10 metal atoms) but these techniques are not widely available and not practical for modeling the binding energy of atoms or molecules to a metal surface at the present time. Plane-wave density functional theoretical methods using pseudopotentials lack a description of spin-orbit and relativistic effects but have the advantages of being widely used and well tested.

In order to validate the use of non-relativistic (Kohn-Sham) DFT, comparisons have been made for several interactions with results from scalar relativistic calculations (for the metal dimers) and experiment. The results are shown in **Figure 4**.

The all-electron scalar relativistic DFT calculations of Pershina et al.¹⁰ are presented in orange. These binding energies are for the Hg-M dimer, where M=Cu, Pd, Ag or Au. In this study, the relativistic local density approximation was used with non-self-consistent non-local corrections via the relativistic forms of Becke's exchange and Perdew's correlation functionals as well as optimized extended basis sets.^{11,12}

Binding energies for the Hg-M dimers calculated with non-relativistic DFT are shown in blue. These calculations also made use of the 1988 exchange functional of Becke and the gradient corrected correlation functional of Perdew, but in this case using the non-relativistic forms. Rather than calculating all electrons explicitly, these calculations made use of the effective core potentials and corresponding basis sets of Sevens et al, CEP-4G.¹³ Relativistic effects are reflected in these results to the extent that they are carried in the pseudopotentials, which were constructed to reproduce the valence electron orbital energies obtained from numerical solutions of the Dirac-Fock equations. The basis sets are not large; for example the Hg basis is (8sp,5d)\[4sp,3d].

The non-relativistic DFT results making use of the limited basis set and the CEP-4G effective core potential are within 0.16 eV of the more demanding fully relativistic DFT study of Pershina et al. for all the Hg-M dimers. It can be seen from **Figure 4** that the trend across the series of metals is consistent between the two methods. These results suggest that non-relativistic DFT methods would be a worthwhile first step in the study of Hg binding to metal surfaces.

The experimental binding energy of Hg to the metal surface is shown in green in **Figure 4**. The four metals, from left to right, are Cu, Pd, Ag and Au and the binding energies are given in eV. The binding energies for the dimers, is of course less than for the surface, which is to be expected. More interesting, is that the trend for both DFT methods tracks so closely the trend observed experimentally for the Hg-metal surface binding energy.

Finally, we have performed plane-wave DFT calculations of Hg adsorbed to the Au(111) surface. The DFT calculations were performed with the Vienna *ab initio* simulation package (VASP)^{14,15} and made use of the projector augmented wave (PAW) method of Blöchl.^{16,17} The plane-wave basis set included waves up to 280 eV. In calculations of bulk Au, the Perdew and Zunger parametrization¹⁸ of the local exchange-correlation functional reproduced most closely the experimental values for cohesive energy, bulk modulus and lattice parameter, and therefore this exchange-correlation functional was used for the subsequent surface calculations. A (√3 x √3) surface cell was employed, with 4 atomic layers, resulting in 24 Au atoms in the supercell model.

As can be seen in **Figure 4**, the value for the adsorption of Hg on the Au surface is quite close to the experimentally determined value. It remains to be seen if the calculated values for the other metals reproduce so well the experimental results.

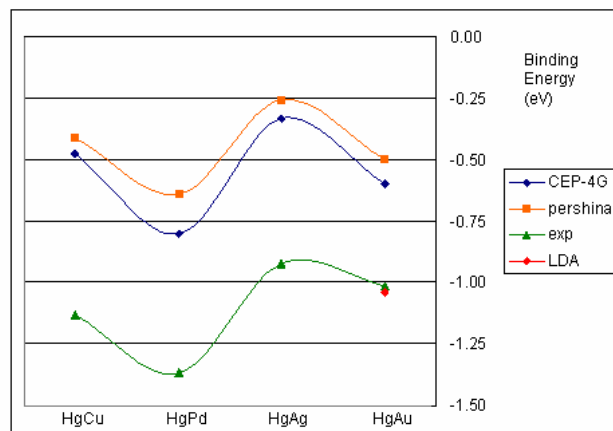


Figure 4. DFT results for Hg-metal binding energies. The orange line is the binding energy of the Hg-M dimer from scalar relativistic DFT calculations of Pershina et al.,¹⁹ the blue line is the binding energy for the same dimers calculated with non-relativistic DFT, and the green line is the experimental binding energy of Hg to the metal surface. The four metals, from left to right, are Cu, Pd, Ag and Au and the binding energies are given in eV

References

- 1 Fujiwara, N.; Fujita, Y.; Tomura, K.; Moritomi, H.; Tuji, T.; Takasu, S.; and Niksa, S.; *Fuel*, **2002**, *81*, 2045.
- 2 Küchle, W.; Dolg, M.; Stoll, H.; and Preuss, H. *Mol. Phys.* **1991**, *74*, 1245.
- 3 Czuchaj, E.; Rebentrost, F.; Stoll, H.; and Preuss, H. *Chem. Phys.* **1997**, *214*, 277.
- 4 Dunning, T. H.; *J. Chem. Phys.*, **1989**, *90*, 1007.
- 5 MOLPRO, version 2002.6, written by H.-J. Werner, P. J. Knowles, M. Schütz, R. Lindh, P. Celani, T. Korona, G. Rauhut, F. R. Manby, R. D. Amos, A. Bernhardsson, A. Berning, D. L. Cooper, M. J. O. Deegan, A. J. Dobbyn, F. Eckert, C. Hampel, G. Hetzer, A. W. Lloyd, S. J. McNicholas, W. Meyer, M. E. Mura, A. Nicklaß, P. Palmieri, R. Pitzer, U. Schumann, H. Stoll, A. J. Stone, R. Tarroni, and T. Thorsteinsson.
- 6 Munro, L. J.; Johnson, K. J.; and Jordan, K. D. *J. Chem. Phys.* **2001**, *114*, 5545.
- 7 Andrae, D.; Häussermann, U.; Dolg, M.; Stoll, H.; and Preuss, H. *Theor. Chim. Acta*, **1990**, *77*, 123.
- 8 Peterson, K. A. In *Recent Advances in Electron Correlation Methodology*; Wilson, A. and Peterson, K. A., Ed.; American Chemical Society, 2003; pp
- 9 Gaussian 03, Revision C.02, Frisch, M. J.; Trucks, G. W.; Schlegel, H. B.; Scuseria, G. E.; Robb, M. A.; Cheeseman, J. R.; Montgomery, Jr., J. A.; Vreven, T.; Kudin, K. N.; Burant, J. C.; Millam, J. M.; Iyengar, S. S.; Tomasi,

J.; Barone, V.; Mennucci, B.; Cossi, M.; Scalmani, G.; Rega, N.; Petersson, G. A.; Nakatsuji, H.; Hada, M.; Ehara, M.; Toyota, K.; Fukuda, R.; Hasegawa, J.; Ishida, M.; Nakajima, T.; Honda, Y.; Kitao, O.; Nakai, H.; Klene, M.; Li, X.; Knox, J. E.; Hratchian, H. P.; Cross, J. B.; Bakken, V.; Adamo, C.; Jaramillo, J.; Gomperts, R.; Stratmann, R. E.; Yazyev, O.; Austin, A. J.; Cammi, R.; Pomelli, C.; Ochterski, J. W.; Ayala, P. Y.; Morokuma, K.; Voth, G. A.; Salvador, P.; Dannenberg, J. J.; Zakrzewski, V. G.; Dapprich, S.; Daniels, A. D.; Strain, M. C.; Farkas, O.; Malick, D. K.; Rabuck, A. D.; Raghavachari, K.; Foresman, J. B.; Ortiz, J. V.; Cui, Q.; Baboul, A. G.; Clifford, S.; Cioslowski, J.; Stefanov, B. B.; Liu, G.; Liashenko, A.; Piskorz, P.; Komaromi, I.; Martin, R. L.; Fox, D. J.; Keith, T.; Al-Laham, M. A.; Peng, C. Y.; Nanayakkara, A.; Challacombe, M.; Gill, P. M. W.; Johnson, B.; Chen, W.; Wong, M. W.; Gonzalez, C.; and Pople, J. A.; Gaussian, Inc., Wallingford CT, 2004

¹⁰ Pershina, V.; Bastug, T.; Jacob, T.; Fricke, B.; and Varga, S. *Chem. Phys. Lett.* **2002**, 365, 176.

¹¹ Becke, A. D. *Phys. Rev. A* **1988**, 38, 3098.

¹² Perdew, J. P. *Phys. Rev. B* **1986**, 33, 8822.

¹³ Stevens, W. J.; Krauss, M.; Basch, H.; and Jasien, P. G. *Can. J. Chem.* **1992**, 70, 612.

¹⁴ Kresse G. and Furthmüller, J. *Phys. Rev. B* **1996**, 54, 11169.

¹⁵ Kresse G. and Furthmüller, J. *Comput. Mater. Sci.* **1996**, 6, 15.

¹⁶ Blöchl, P. E. *Phys. Rev. B* **1994**, 50, 17953.

¹⁷ Kresse, G. and Joubert, D. *Phys. Rev. B* **1999**, 59, 1758.

¹⁸ Perdew, J. P.; and Zunger, A. *Phys. Rev. B* **1981**, 23, 5048.

¹⁹ Pershina, V.; Bastug, T.; Jacob, T.; Fricke, B.; and Varga, S. *Chem. Phys. Lett.* **2002**, 365, 176.

FIRST-PRINCIPLES KINETICS FOR COMBUSTION SYSTEMS USING REACTION CLASS TRANSITION STATE THEORY

Lam K. Huynh and Thanh N. Truong

Henry Eyring Center for Theoretical Chemistry, Department of Chemistry, University of Utah, Salt Lake City, 315 S. 1400 E. Rm. 2020, Salt Lake City, Utah 84112

Introduction

Accurate kinetic data of important elementary reactions are of utmost critical for molecular-level detailed simulations of combustion of hydrocarbons. Kinetic models for such system often involve a very large number of elementary reactions. The greatest challenge arises from this is that kinetic information of most of elementary reactions involved in combustion of hydrocarbons is not known either experimentally or theoretically.

Recently we introduced a theory called Reaction Class Transition State Theory (RC-TST) for predictions of thermal rate constants for a large number of reactions in a given class.^{1,2} The RC-TST method recognizes that reactions in a given class having the same reactive moiety, therefore their potential energy surfaces along the reaction coordinate are very similar and thus can be extrapolated from one to the others. Furthermore, within a given reaction class there is a linear energy relationship (LER) between the barrier heights and reaction energies. Combining both facts, the RC-TST/LER theory provides a rigorous methodology for estimating thermal rate constants of any reaction only from its reaction energy, which can be calculated from a relatively low level of theory such as a semi-empirical molecular orbital method.

Since reactions in the same class have the same reactive moiety, the difference between the rate constants of two reactions is mainly due to differences in the interactions between the reactive moiety and their substituents. Within the TST framework, the rate constant of an arbitrary reaction (denominated by R_a) is proportional to the rate constant of the reference reaction (denominated by R_p) of the same class, to which it is related by a temperature dependent function $f(T)$:

$$k_a(T) = f(T)k_p(T) \quad (1)$$

The reference reaction is often a small reaction in the class of which the rate constants k_p can be accurately predicted from first principles and are often also known experimentally. The key idea of the RC-TST method is to factor $f(T)$ into different components under the TST framework:

$$f(T) = f_\sigma f_\kappa f_Q f_V \quad (2)$$

where f_σ , f_κ , f_Q and f_V are symmetry number, tunneling, partition function and potential energy factors, respectively. These factors are simply the ratio of the corresponding components in the TST expressions for the two reactions:

$$f_\sigma = \frac{\sigma_a}{\sigma_p} \quad (3)$$

$$f_\kappa(T) = \frac{\kappa_a(T)}{\kappa_p(T)} \quad (4)$$

$$f_Q(T) = \frac{\left(\frac{Q_a^\ddagger(T)}{\Phi_a^R(T)} \right)}{\left(\frac{Q_p^\ddagger(T)}{\Phi_p^R(T)} \right)} = \frac{\left(\frac{Q_a^\ddagger(T)}{Q_p^\ddagger(T)} \right)}{\left(\frac{\Phi_a^R(T)}{\Phi_p^R(T)} \right)} \quad (5)$$

$$f_V(T) = \exp \left[-\frac{(\Delta V_a^\ddagger - \Delta V_p^\ddagger)}{k_B T} \right] = \exp \left[-\frac{\Delta \Delta V^\ddagger}{k_B T} \right] \quad (6)$$

The central task is to determine approximate analytical expressions for these factors so that rate constants for any reaction can be quickly estimated according to Eq. (1). This can be accomplished by selecting a small representative set of reactions in the considered class, which often ranges in the order of 15-20 reactions, to perform explicit TST/Eckart rate calculations. Analyses of the 'exact' calculated factors as functions of temperature allow us to find general trends and to fit these factors to analytical expressions for representing the entire class.

The symmetry number factor f_σ can be determined exactly from the symmetry numbers of R_p and R_a . The symmetry number of a reaction can be easily calculated from the rotational symmetry numbers of the reactant and transition state.³

The tunneling factor f_κ is the ratio of transmission coefficients of R_a and that of R_p . Although absolute transmission coefficients for hydrogen abstraction reactions often require multi-dimensional tunneling methods to account for the large corner-cutting effects, due to cancellation of errors, we have shown that the tunneling factor f_κ can be accurately predicted using the 1-D Eckart method⁴. The calculated results for the representative set of reactions then can be fitted to an analytical expression.

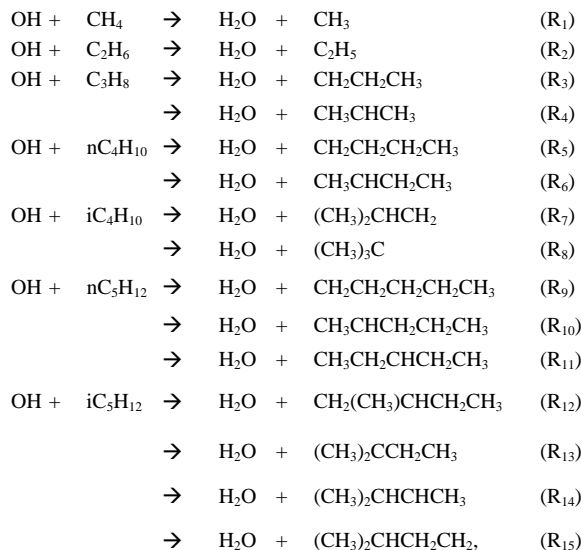
The partition function factor f_Q is the ratio of partition functions of the reactants and transition states of R_a and R_p (Eq.5). We have shown that the main factors that govern the temperature dependence of the f_Q factor are the differences in the vibrational frequencies due to the coupling of substituents with the reactive moiety. Thus, even in flexible molecules where it is difficult to calculate accurately the partition functions of the low frequency vibrational modes such as hindered rotations, their effects can be easily included in f_Q . We found that f_Q are often not sensitive to the temperature and a single analytical expression can be used to approximate this factor for the entire class.

The potential energy factor can be calculated from the differential barrier height of the reference reaction and the target reaction according to Eq. (6). It is known that in order to achieve accuracy of order 1 kcal/mol in the classical barrier height for radical reactions a rather high level of electronic structure theory such as CCSD(T) is required. However, we have shown that the differences in the barrier heights for reactions in a given class can be accurately calculated at a lower level of theory. In fact, we also have shown that within a given class there is a Linear Energy Relationship (LER) between the barrier height and reaction energy, similar to the well-known Evans-Polanyi linear energy relationship. Such relationships have been observed in all of reaction classes that we considered so far. As a result, the f_V factor can be computed from only the reaction energy, which can be calculated using potential energy information calculated for calculations of thermodynamic properties of these species discussed above.

In summary, to develop RC-TST/LER parameters for each reaction class, we need to carry out a series of tasks: 1) Performing accurate calculations of rate constants of the reference reaction using Canonical Variational TST augmented with multi-dimensional semiclassical tunneling corrections or use known accurate literature data; 2) Performing TST/Eckart calculations for a representative set of reactions in the considered reaction class; 3) Analyzing the exact calculated factors in order to derive approximate expressions to represent the entire class. This includes determining the LER between the barrier heights and reaction energies.

Application to the OH + H-C(sp³) class

Here we illustrate how the RC-TST/LER method is employed to estimate rate constants for the reaction class hydrogen abstraction by hydroxyl radical OH+H-C(sp³), where C(sp³) denotes a saturated carbon atom. This is one of the most important reaction classes in combustion. Following is the set of reactions that are used to derive the analytic expression for the whole reaction class.



Computational methods. All the electronic structure calculations were carried out using the program package GAUSSIAN 98.⁵ BH&HLYP density functional method has been found previously to be sufficiently accurate for predicting the transition state properties for hydrogen abstraction reactions by a radical.⁶⁻⁹ Note that within the RC-TST framework as discussed above, only the relative barrier heights are needed. Our previous study has shown they can be accurately predicted by the BH&HLYP method.⁹ Geometries of reactants, transition states, and products were optimized at the BH&HLYP level of theory with the cc-pVDZ basis set, which is large enough to capture the physical change in this type of reaction. Frequencies of the stationary points were also calculated at the same level of theory. This information was used to derive the RC-TST factors. The AM1 semi-empirical method was also employed to calculate the reaction energies of those considered here. AM1 and BH&HLYP/cc-pVDZ reaction energies were then used to derive the LER's between the barrier height and reaction energy. The TST rate constants, tunneling factors, and partition function factors including the hindered rotation treatment were calculated employing kinetic module of the web-based CSEO program.¹⁰

Due to the simplicity and similarity (C-C and C-H bond) of reaction R₂ to other reactions in the class, this reaction is chosen to be the reference reaction; thus the following analysis is based on this reaction.

Symmetry number factor. Symmetry number factors f_{σ} were calculated simply from the ratio of symmetry numbers of the arbitrary and principal reactions using Eq. (3) and are listed in Table 1.

Tunneling factor. It is observed in this study as well as in our previous work^{1,2} that tunneling factors for hydrogen abstraction reactions at the same sites - primary, secondary or tertiary carbon site - are rather similar and thus can be assumed to be the same for each site. Simple expressions for the three factors for primary, secondary

and tertiary carbon sites, respectively, are obtained by fitting to the calculated values, given in Table 2.

Table 1. Calculated symmetry number factors and tunneling factors at 300K

Rxn	Sym. number factor	Tunneling ratio factor, f_{κ}			
		(^a)	(^b)	(^c)	(^d)
R ₂	1.000	(13.08 ^g)			
R ₃	1.000	0.89 ^{a1}	1.04	0.14 ^e	13.73
R ₄	0.333	0.29 ^{a2}	0.35	0.06	17.59
R ₅	1.000	0.89 ^{a1}	0.86	0.03	4.00
R ₆	0.667	0.29 ^{a2}	0.30	0.02	5.82
R ₇	1.500	0.89 ^{a1}	0.83	0.06	7.64
R ₈	0.167	0.15 ^{a3}	0.16	0.01	6.84
R ₉	1.000	0.89 ^{a1}	0.99	0.10	10.15
R ₁₀	0.667	0.29 ^{a2}	0.26	0.02	8.22
R ₁₁	0.333	0.29 ^{a2}	0.21	0.08	35.67 ^e
R ₁₂	1.000	0.89 ^{a1}	0.84	0.06	6.86
R ₁₃	0.167	0.15 ^{a3}	0.12	0.03	23.52
R ₁₄	0.333	0.29 ^{a2}	0.28	0.01	3.03
R ₁₅	0.500	0.89 ^{a1}	0.81	0.09	10.91
MAD^f				0.05	11.85

^a Calculated by using fitting expression (see Table 2); ^{a1} primary sites, ^{a2} secondary site, and ^{a3} tertiary sites; ^b Calculated directly using Eckart method with BH&HLYP/cc-pVDZ reaction barrier heights and energies; ^c Absolute deviation between the fitting and directly calculated values; ^d Percentage of deviation (%); ^e Maximum values; ^f Mean absolute deviations (MAD) and deviation percentage between the fitting and directly calculated values; ^g Tunneling coefficient calculated for reaction (R₂) using Eckart method.

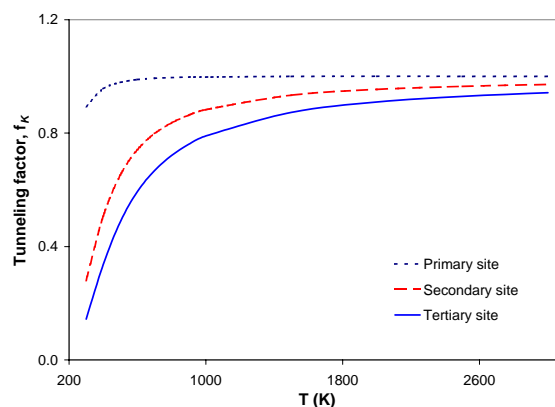


Figure 1. Plot of the tunneling factors f_K as functions of temperature for abstractions of hydrogen from primary (dotted line), secondary (dashed line), and tertiary (solid line) carbon atoms.

The correlation coefficients for these fits are larger than 0.999. The results are plotted in Figure 1. The error analysis of tunneling ratio factor at 300K where the error is the largest is also shown in Table 2. It can be seen that the same tunneling factor can be reasonably assigned to those reactions at the same site with the

largest absolute deviation of 0.14 for R₃, the largest percentage deviation of 35.6% at R₁₁, and the mean absolute deviation of 11.8 % compared to the direct Eckart calculation using reaction information from BH&HLYP/cc-pVDZ level of theory. At higher temperatures the differences between the approximated values and the explicitly calculated ones decrease, for example, the maximum error for all reactions is less than 10% at 500K. Besides, when the temperature increase, these factors approach constant values, which mean that when the temperature high enough, these factors are temperature independent as expected since tunneling becomes less important at high temperatures.

Partition function factor. Partition function factors for 13 reactions in the class calculated in the temperature range 300-2500K are given in Figures 2 a & b. It is noted that the hinder rotation treatment of low frequencies is also included in the partition function calculations as described in ref.¹¹. The partition for the secondary and tertiary sites is less dependent on the temperature than the primary site (see figure 2); thus we can group and treat them together. It can be seen that the partition function factor for primary sites tends to increase linearly with the increasing temperature while the trend for secondary and tertiary sites is almost constant at high temperature (T>1000K). Since the temperature dependent part cancels out in translational and rotational components of f_Q , temperature dependence comes only from the vibrational function factor.

The partition function factors for this class can be approximated by the fitting functions given in table 2. These expressions give the maximum error of less than 70% and the mean absolute error less than 58% for all reaction from 300K to 2500K. In other words, this approximation will affect at most the total rate constant individually by a factor of 1.7. This is the source that causes the most internal error for this approach (see Figure 2).

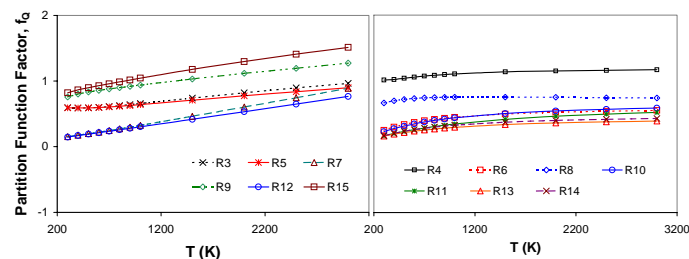


Figure 2. Plot of the partition function factor f_Q as functions of the temperature for all reactions considered at (a) primary carbon sites and (b) secondary and tertiary carbon sites.

Potential energy factor. The potential energy factor f_V can be easily calculated using eq. (6) where ΔV_a^\ddagger and ΔV_p^\ddagger are the barrier heights of the arbitrary and the reference reactions, respectively. The reaction barrier heights of any reaction in this class can be obtained by utilizing the LER between the reaction energy and the reaction barrier height. The reaction barrier heights calculated at BH&HLYP/cc-pvdz are plotted against reaction energies calculated at the BH&HLYP/cc-pVDZ and AM1 level. The two linear relationships were plotted in Figures 3 a & b. The fitting expressions using the least squared method are given in table 2 below. The absolute deviations of reaction barrier heights between the LERs and full quantum calculations are smaller than 1.0 kcal/mol. The mean absolute deviation of reaction barrier heights predicted from BH&HLYP and AM1 reaction energies are 0.51 and 0.49 kcal/mol, respectively. These deviations are in fact smaller than the systematic errors of the computed reaction barriers from full electronic structure calculations. Both LER's yield very similar barrier heights with the

maximum difference of less than 0.2 kcal/mol. For this reason, for the error analyses given below only the BH&HLYP results were used. However, for actual application of the method, AM1 is recommended.

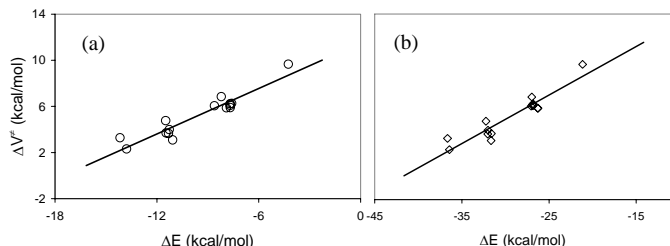


Figure 3. Linear energy relationship plots of barriers heights ΔV^\ddagger versus reaction energies ΔE . Barrier heights were calculated at BH&HLYP/cc-pVDZ level of theory. ΔE 's were calculated at (a) the BH&HLYP/cc-pVDZ and (b) AM1 level of theory.

Table 2 summarizes the RC-TST parameters for this reaction class.

Table 2. *Ab Initio* Derived Parameters and Formulations for the OH+H-C(sp³) Hydrogen Abstraction Reaction Class.

$k(T) = f_\sigma \times f_K(T) \times f_Q(T) \times f_V(T) \times k_p(T)$	
f_σ	Calculated explicitly from the sym. of rxns (see Table 1)
$f_K(T)$	$f_K = \frac{5 \times 10^{-8}}{4.998 \times 10^{-8} + T^{-3.32}}$: primary sites
	$f_K = 0.974 \times \exp(-2.581 \times 10^5 \times T^{-2.149})$: secondary sites
	$f_K = 0.9557 \times \exp(-1.026 \times 10^5 \times T^{-1.917})$: tertiary sites
$f_Q(T)$	$f_Q = 0.0002912 \times T + 0.1763$: primary sites
	$f_Q = \frac{T}{0.0006621 + 1.471 \times T}$: secondary & tertiary sites
$f_V(T) = \exp\left[\frac{-(\Delta V_a^\ddagger - \Delta V_p^\ddagger)}{k_B T}\right]$	
$f_V(T)$	$\Delta V_a^\ddagger = 0.4466 \times \Delta E_a + 18.491$: ΔE_a at the AM1
	$\Delta V_a^\ddagger = 0.6573 \times \Delta E_a + 11.491$: ΔE_a at the BH&HLYP
	$\Delta V_p^\ddagger = 6.10$ kcal/mol
$k_p(T)$	$k_P = 1.06 \times 10^{-12} \times \left(\frac{T}{298K}\right)^{2.00} \times \exp\left(-\frac{860(\text{cal/mol})}{RT}\right)$, cm ³ .molecule ⁻¹ .s ⁻¹ (from ref. ¹²)

We selected the hydrogen abstraction reaction of propane at primary carbon site as a representative reaction whose rate constants have been determined experimentally or derived from other experimental data for more detailed discussion to illustrate the theory.

Figure 4 shows the Arrhenius plots of the calculated rate constants using the RC-TST/LER method for this reaction along with available experimental data. The estimated rate constants are quite closed to the experimental value of ref.¹³ at low temperatures and tend to approach the values of ref.¹⁴ and ref.¹⁵ at high temperatures.

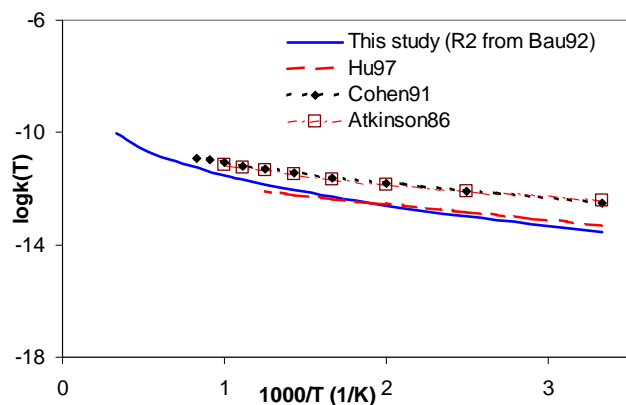


Figure 4. Arrhenius plots of the calculated rate constants using the RC-TST/LER method for the hydrogen abstraction reaction at primary carbon site of C_3H_8 (Reaction R_3)

We examined the internal errors in different factors in the RC-TST/LER method. The total internal error is affected by the errors in the approximations in the tunneling factor, partition function factor and the potential energy factor used in the method. The results of the error analysis from these different relative rate factors are shown in Figure 5. Errors from all components are less than 60% for the temperature range from 300 to 3000K. The errors tend to decrease when temperature increases. The total internal errors occurring in the relative rate factor of less than 60% show that RC-TST/LER is an excellent extrapolation method for the rate constants of any reaction in this class from that of the reference reaction.

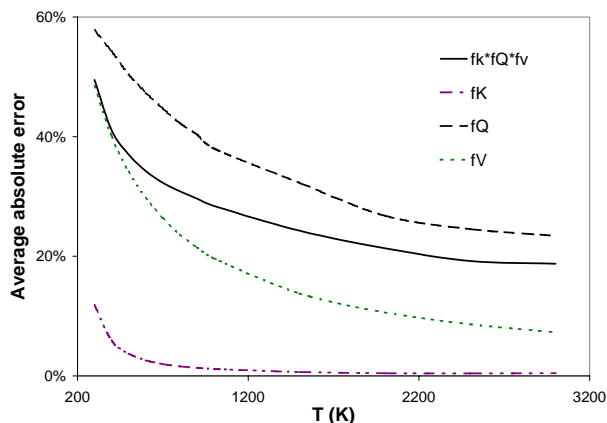


Figure 5. Average absolute errors of the total relative rate factors $f(T)$ (Eq. 2) and its components, namely the tunneling (f_K), partition function (f_Q), and potential energy (f_V) factors as functions of temperature.

Conclusions

We have introduced the RC-TST/LER method and presented its application for prediction of thermal rate constants of the reaction class $OH + H-C(sp^3)$. The RC-TST/LER method is shown to be both simple and effective for rate constant prediction of any reaction in a given class from only the reaction energy that can be calculated from a low level of electronic structure theory such as DFT or semiempirical molecular orbital method. We have derived parameters for the RC-TST/LER method for the above reaction class from first-principles

rate constants of 13 small reactions. We found that the predicted rate constants are in good agreement with available data. Finally, detailed analysis shows that the systematic errors in the calculated rate constants arise from approximations used in the RC-TST/LER method are less than 60%.

Acknowledgement. This work is supported in part by NSF. LKH is grateful to the Vietnam Education Foundation for a Graduate Fellowship. The authors would like to thank the Utah Center for High Performance Computing for computer time support.

References

- (1) Truong, T. N. *J. Chem. Phys.* **2000**, *113*, 4957-4964.
- (2) Zhang, S.; Truong, T. N. *J. Phys. Chem. A* **2003**, *107*, 1138-1147.
- (3) Duncan, W. T.; Bell, R. L.; Truong, T. N. *J. Comp. Chem.* **1998**, *19*, 1039-1052.
- (4) Miller, W. H. *J. Am. Chem. Soc.* **1979**, *101*, 6810-6814.
- (5) Frisch, M. J.; Trucks, G. W.; Schlegel, H. B.; G. E. Scuseria; Robb, M. A.; Cheeseman, J. R.; Zakrzewski, V. G.; Montgomery, J. A.; Stratmann, R. E.; Burant, J. C.; Dapprich, S.; Millam, J. M.; Daniels, A. D.; Kudin, K. N.; Strain, M. C.; Farkas, O.; Tomasi, J.; Barone, V.; Cossi, M.; Cammi, R.; Mennucci, B.; Pomelli, C.; Adamo, C.; Clifford, S.; Ochterski, J.; Petersson, G. A.; Ayala, P. Y.; Cui, Q.; Morokuma, K.; Malick, D. K.; Rabuck, A. D.; Raghavachari, B.; Foresman, J. B.; Cioslowski, J.; Ortiz, J. V.; Stefanov, B.; Liu, G.; Liashenko, A.; Piskorz, P.; Komaromi, I.; Gomperts, R.; Martin, R. L.; Fox, D. J.; Keith, T.; Al-Laham, M. A.; Peng, C. Y.; A. Nanayakkara; Gonzalez, C.; Challacombe, M.; Gill, P. M. W.; Johnson, B. G.; Chen, W.; Wong, M. W.; Andres, J. L.; Head-Gordon, M.; Replogle, E. S.; Pople, J. A. *GAUSSIAN 98, Revision A.7*, Gaussian, Inc., Pittsburgh PA (1998).
- (6) Truong, T. N.; Duncan, W. *J. Chem. Phys.* **1994**, *101*, 7408-7414.
- (7) Lynch, B. J.; Fast, P. L.; Harris, M.; Truhlar, D. G. *J. Phys. Chem. A* **2000**, *104*, 4811-4815.
- (8) Zhang, Q.; Bell, R.; Truong, T. N. *J. Phys. Chem.* **1995**, *99*, 592-599.
- (9) Truong, T. N.; Maity, D. K.; Truong, T.-T. *J. Chem. Phys.* **2000**, *112*, 24-30.
- (10) Truong, T. N. <http://www.cseo.net>.
- (11) Ayala, P. Y.; Schlegel, H. B. *J. Chem. Phys.* **1998**, *108*, 2314.
- (12) Baulch, D. L.; Cobos, C. J.; Cox, R. A.; Esscer, C.; Frank, P.; Just, T.; Kerr, J. A.; Pilling, M. J.; Troe, J.; Walker, R. W.; Warnatz, J. *J. Phys. Chem. Ref. Data* **1992**, *21*, 411-429.
- (13) Hu, W.-P.; Rossi, I.; Corchado, J. C.; Truhlar, D. G. *J. Phys. Chem. A* **1997**, *101*, 6911-6921.
- (14) Cohen, N. *Int. J. Chem. Kinet.* **1991**, *23*, 397-417.
- (15) Atkinson, R. *Int. J. Chem. Kinet.* **1986**, *18*.

REACTIONS OVER MULTIPLE INTERCONNECTED POTENTIAL WELLS: A THEORETICAL FRAMEWORK

James A. Miller and Stephen J. Klippenstein

Combustion Research Facility
Sandia National Laboratories
Livermore, CA 94551-9069

Many reactions in combustion, particularly those involved in the formation of aromatic compounds, polycyclic aromatic compounds (PAH), and soot, are complicated processes that take place over multiple, interconnected potential wells. Such reactions may be chemically activated, or they may be thermal dissociation/isomerization processes. Some of the former are “collisionless” in that the intermediate complexes are so short-lived that they effectively do not suffer any collisions under conditions that are normally of interest. However, intermediate complexes more commonly live long enough to suffer numerous collisions. In such cases, any of a number of stabilized or bimolecular products may result. These reactions require a theoretical description in terms of a time-dependent, multiple-well master equation. While solving the master equation is reasonably straightforward, obtaining rate-constant information from the analysis has not proven to be a simple task. In this presentation, we describe the methods we have developed for solving the master equation and obtaining thermal rate coefficients from its solution. We use reactions involving propargyl radicals (C_3H_3+H , $C_3H_3+O_2$, and $C_3H_3+C_3H_3$) to illustrate the methods.

The objective of our efforts is to develop robust, systematic procedures for extracting phenomenological rate coefficients from solutions to the time-dependent, multiple-well master equation. Such an equation can be written in the deceptively simple matrix form

$$\frac{d|w\rangle}{dt} = G|w\rangle, \quad (1)$$

where G is the transition matrix. The solution to Eq. (1) can be written as

$$|w(t)\rangle = \hat{T}|w(0)\rangle, \quad (2)$$

where \hat{T} is the time evolution operator, $\hat{T} = \sum_{j=0}^N e^{\lambda_j t} |g_j\rangle\langle g_j|$, and can be constructed from the eigenvalues and eigenvectors of G , $G|g_j\rangle = \lambda_j|g_j\rangle$. Of course, having the solution (2) does not help us very much; what we really want is phenomenological rate coefficients, $k(T,p)$, to use in flame models.

In accomplishing this objective the first point to realize is that, although G will likely have several thousand eigenpairs, only a small number,

$$N_{\text{chem}} = S-1, \quad (3)$$

where S is the number of chemical configurations in the problem (wells plus sets of bimolecular fragments), describe chemical change. The remainder relax much faster than these CSE's

(chemically significant eigenpairs) and describe internal energy relaxation. At the same time, there are “forward” rate coefficients (and all equal number of reverse rate coefficients) embedded in the CSE's.

$$N_k = \frac{S(S-1)}{2} \quad (4)$$

We have derived 2 different methods of obtaining the rate coefficients from the CSE's. The first (and simplest) is to apply \hat{T} to multiple initial conditions and take the limit as $t \rightarrow 0$. In this case, one obtains

$$k_{Ti} = \sum_{j=1}^{N_{\text{chem}}} \lambda_j \Delta X_{ij}^{(i)} \quad (5)$$

and

$$k_{i\ell} = - \sum_{j=1}^{N_{\text{chem}}} \lambda_j \Delta X_{\ell j}^{(i)}$$

where k_{Ti} is the total rate coefficient for removal of “species” i , and $k_{i\ell}$ is the $i \rightarrow \ell$ rate coefficient. In Eq. 5 ΔX_{ij} is the change in population of the i^{th} configuration (or species) brought about by the j^{th} eigenpair; the superscript i indicates that species i is the initial reactant.

The second method exploits the fact that the time evolution of the chemical system, regardless of the initial condition, is equivalent to the solution of a system of rate equations with the rate coefficients,

$$k_{Ti} = - \sum_{j=0}^{N_{\text{chem}}} \lambda_j a_{ij} b_{ji}$$

and

$$k_{i\ell} = \sum_{j=0}^{N_{\text{chem}}} \lambda_j a_{\ell j} b_{ji}$$

where $a_{ij} = -\Delta X_{ij} (j \neq 0)$ and $a_{i0} = X_i(\infty)$, the population at $t = \infty$. If the a_{ij} are considered to be the elements of a matrix A , the b_{ij} are the elements of $B = A^{-1}$. The 2 different methods, as expected, give the same results for the rate coefficients under normal conditions.

The power of the methodology is illustrated well by applying it to reactions occurring on the C_3H_4 potential. We will note 2 points specifically:

1. The formalism allows one to distinguish *unambiguously* between the one-step process allene \rightleftharpoons propyne and the two-step process allene \rightleftharpoons cyclopropene \rightleftharpoons propyne even though both processes follow the same reaction path on the potential.

2. It also allows one to distinguish between the dissociations of allene and propyne to propargyl + H, even though the allene \rightleftharpoons propyne isomerization equilibrates much faster than either dissociation. In fact, most experiments are sensitive only to the eigenvalue of G that describes the dissociation of the equilibrated isomers (allene, propyne, and cyclopropene).

Acknowledgement. This work was supported by the United States Department of Energy, Office of Basic Energy Sciences, Division of Chemical Sciences, Geosciences, and biosciences. Sandia is a multi-program laboratory operated by Sandia Corporation, a Lockheed Martin Company, for the United States Department of Energy's National Nuclear Security Administration under contract DE-AC04-94AL85000.

AB INITIO AND DENSITY FUNCTIONAL THEORY CALCULATIONS OF THE ENERGETICS OF AUTOXIDATION REACTIONS

Steven Zabarnick

University of Dayton Research Institute
300 College Park
Dayton, OH 45469-0116

Introduction

Prior to being combusted for propulsion, jet fuel is heated during passage through aircraft fuel system components. This heating occurs incidentally while passing through fuel pumps, but is encouraged via heat exchangers, particularly in advanced military aircraft, to remove excess heat from numerous aircraft subsystems. Systems which may require cooling include avionics, hydraulics, and environmental control. The use of fuel to cool fuel system and combustion components is an enabling technology for advanced military aircraft. Unfortunately, the heat absorbed by the fuel is not always innocuous. When fuel temperatures approach 150°C, the fuel begins to react via an autoxidation chain with the small amount of dissolved oxygen present from exposure to air. These autoxidation reactions ultimately result in formation of detrimental surface deposits and bulk insolubles. These deposits can plug narrow passageways in valves, filters, and nozzles and can inhibit required heat transfer in heat exchangers. Numerous techniques have been investigated to limit the production of deposits, including: fuel system design to minimize fuel temperatures, additives to inhibit autoxidation and/or deposit formation, deoxygenation, surface coatings, and inclusion of "sacrificial" or coke tolerant components.¹ Each of these solutions has corresponding advantages and disadvantages which are dependent on the application.

In recent years chemical kinetic models have been developed which simulate the major autoxidation reactions which occur in jet fuels.²⁻⁴ Development of a widely applicable autoxidation mechanism, which includes deposit formation, would greatly aid the fuel system design process, and enable the more efficient use of the fuel as a heat sink. As jet fuels consist of thousands of individual species, which vary in their identity and concentration in different fuel samples, it is impractical to build detailed chemical kinetic mechanisms. Grouped or lumped mechanisms, referred to as "pseudo-detailed" mechanisms, have been used to simulate the most important reactive pathways, including the effects of antioxidants and catalytic surfaces.²⁻⁴ These mechanisms have been combined with computational fluid dynamic techniques to simulate the complex time and temperature variation in flowing fuel system components.^{5,6} Most recently, initial attempts at including global deposit formation reactions to these mechanisms has been performed.^{7,8}

Unfortunately, reliable experimental kinetic parameters are often not available for inclusion in these chemical kinetic mechanisms. It is desirable to have a consistent and reliable method to estimate such parameters. Recently, researchers have begun to apply semi-empirical quantum mechanical⁹ and density functional theory¹⁰ methods to determine Arrhenius parameters for autoxidation reactions. These techniques promise to provide methods to readily estimate rate parameters and evaluate the plausibility of candidate autoxidation and deposit forming reactions. In the current work, we explore the use of *ab initio* and density functional theory electronic structure methods for the calculation of the energetics of autoxidation reactions.

Computational Methodology

All calculations were performed using Gaussian 03 software (Gaussian, Inc.) on the USAF Aeronautical Systems Center Major Shared Resource Center computational facilities. Frequency and thermodynamic calculations were performed at 25°C and one atmosphere pressure. Transition state geometries were calculated using the Synchronous Transit-Guided Quasi-Newton method. All transition states reported were confirmed to contain a single imaginary frequency. Animation of the normal mode coordinate corresponding to the imaginary frequency of the transition state was performed to confirm connection between the reactants and products. Activation energies were calculated from the difference between the unscaled zero-point and thermal energy corrected enthalpies of the transition state and the reactants. Self-consistent reaction field simulations of the effect of solvation was performed using the SCI-PCM technique with heptane as the solvent.

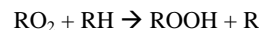
Results and Discussions

Initial validation runs were conducted for the calculation of the bond dissociation enthalpy of the O-O bond in n-butylhydroperoxide. Hydroperoxides are known to be important initiators of autoxidation and intermediates in the overall chain process. n-Butylhydroperoxide was chosen as a small model molecule of the large chain hydroperoxides produced in fuel. Previous work indicates that the bond dissociation enthalpies of alkyl hydroperoxides, nearly independent of the identity of the alkyl group, is ~45 kcal/mol.¹¹ Results at various levels of theory using the 6-31G(d) basis set, except where noted, are shown in Table 1. The results indicate that using electron correlation techniques (all except the HF result) are essential to obtain accurate values. The density functional technique employed here, B3LYP, is similar in computational cost to HF, but yields more accurate values. *Ab initio* (MP2), complete basis set (CBS), and compound techniques (G3B3) yield even better results at a significantly higher computational cost. It was concluded that the density functional method resulted in the best compromise between accuracy and computational cost for the relatively large reaction systems that need to be studied in the autoxidation chemistry of jet fuel. All subsequent calculations employed the B3LYP level of theory.

Table 1. Calculated Bond Dissociation Enthalpies for the O-O Bond in n-Butylhydroperoxide Using the 6-31G(d) Basis Set

Level of Theory/Basis Set	ΔH
HF/6-31G(d)	0.3
B3LYP/6-31G(d)	40.0
B3LYP/6-31G(d,p)	40.0
MP2/6-31G(d)	48.8
CBS-4M	45.0
G3B3	43.5
Experiment	~45

One of the most important reactions in autoxidation is the propagation reaction in which peroxy radicals abstract a hydrogen atom from a fuel species, producing a hydroperoxide and a hydrocarbon radical:



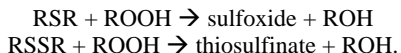
We have calculated the reaction enthalpies and activation energies at the B3LYP level of theory using both the 6-31G(d) and 6-31G(d,p) basis sets for the reaction of 2-butylhydroperoxy with a number of model fuel species, as shown in Table 2. The data show that, using the 6-31G(d) basis set, the enthalpy of reaction with the benzylic hydrogen in ethylbenzene is significantly lower than reaction with a secondary hydrogen in n-butane. In addition, the activation energy is

significantly lower for the benzylic hydrogen reaction. This result agrees with well known higher reactivity of benzylic hydrogens and indicates that fuel aromatics, which are typically 15-20% by volume, can play an important role in controlling the overall oxidative reactivity of the fuel. Also shown in the table are the results for reaction with the phenolic hydrogen in ethylphenol and the antioxidant species BHT (2,6 di-*t*-butyl-4-methylphenol). The results indicate that these phenolic hydrogens are significantly higher in reactivity than even the benzylic hydrogens. The calculations show that abstraction of the BHT phenolic hydrogen is the only one of these reactions that is exothermic, which explains its high reactivity even when employed as an additive at very low concentrations, although the calculated activation energy is similar to that of ethylphenol. The table also shows results when polarization functions, which allow p-orbital character on hydrogen atoms, are included in the basis sets (i.e., the 6-31G(d,p) basis set). The results indicate that including these additional polarization functions usually decreases the calculated enthalpies and activation energies by <3 kcal/mol. Previous chemical kinetic mechanisms²⁻⁶ for fuel autoxidation used activation energy values of 10-12 and 5 kcal/mol for the reaction of peroxy radicals with fuel species and antioxidants, respectively.

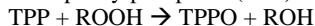
Table 2. Calculated Reaction Enthalpies and Activation Energies using B3LYP Density Functional Theory for the Abstraction of Hydrogen from Model Fuel Species by 2-Butylhydroperoxy Radicals

Reaction species (abstracted H)	ΔH	E_a	ΔH	E_a
	6-31G(d)		6-31G(d,p)	
n-butane (secondary hydrogen)	20.9	20.1	--	--
ethylbenzene (benzylic hydrogen)	9.2	15.4	6.7	13.6
ethylphenol (phenolic hydrogen)	3.4	1.8	3.8	0.8
BHT (phenolic hydrogen)	-4.6	2.2	--	--

Another important class of reactions in autoxidation is the reaction of alkyl or aromatic hydroperoxides with species such as sulfides and disulfides via:



These reactions proceed via a non-radical pathway and can greatly slow autoxidation by consumption of the peroxide,¹² thereby preventing its decomposition into additional radicals which would accelerate the chain. It has been proposed that these reactions may contribute to formation of deposits.⁷ Table 3 shows results for B3LYP calculations of reaction enthalpies and activation energies of the reaction of diethylsulfide and diethyldisulfide with n-butylhydroperoxide. The results show that both reactions are quite exothermic (ca. -27 kcal/mol), but have significant activation barriers (26 to 29 kcal/mol). The magnitudes of these barriers imply an interesting competition for the fate fuel peroxides, which can decompose unimolecularly with a 45 kcal/mol activation energy, as discussed above. Obviously, the concentration of the sulfides and/or disulfides present will determine the fate of the peroxides. This implies that this fate is quite fuel sample dependent, as the concentrations of these species can vary greatly between fuel samples. Also shown in Table 3 are calculated results for the reaction of fuel peroxides with triphenylphosphine (TPP) via:



TPP is known to react readily with peroxides and has been used in their quantitation.¹³ The data show that the reaction is highly exothermic with a relatively small barrier. Also shown in the table are the calculated values of the transition state imaginary frequencies (reaction coordinate) for each of these reactions with hydroperoxides.

Previous workers have shown that the magnitude of this frequency indicates the type of molecular motion of the OH group in the transition state.¹⁴ In agreement with this previous work, the frequencies obtained imply that the sulfide/disulfide reaction coordinate is dominated by motion of the hydrogen atom (high frequency), while the phosphine reaction coordinate is dominated by motion of the oxygen atom (low frequency).

Table 3. Calculated Reaction Enthalpies and Activation Energies using B3LYP Density Functional Theory for Reaction of n-Butylhydroperoxide with Sulfides and Phosphines

Reaction species	ΔH	E_a	Transition State Imaginary Freq (cm ⁻¹)
diethylsulfide	-26.3	26.1	-668
diethyldisulfide	-27.7	28.7	-716
triphenylphosphine	-75.0	12.9	-369

Conclusions

Ab initio and density functional theory calculations of reaction enthalpies and activation energies were calculated for important reactions involved in the autoxidation of jet fuel. The results show that these computational techniques can yield information that is useful in the development of chemical kinetic mechanisms of the chain oxidation process. These methods are particularly useful in estimating activation energies for reactions that have no previous experimental measurements. Currently we are exploring the use of self-consistent reaction field calculations to explore the effect of the solvent on the reaction energetics of these reactions.

Acknowledgement. This material is based on research sponsored by Air Force Research Laboratory under agreement number F33615-03-2-2347. The U.S. Government is authorized to reproduce and distribute reprints for Governmental purposes notwithstanding any copyright notation thereon.

The views and conclusions contained herein are those of the authors and should not be interpreted as necessarily representing the official policies or endorsements, either expressed or implied, of Air Force Research Laboratory or the U.S. Government.

The author would like to thank Dr. Don Phelps of AFRL for many helpful discussions.

References

- (1) Heneghan, S.P.; Zabarnick, S.; Ballal, D.R.; Harrison, W.E. *J. Energy Res. Tech.* **1996**, *118*, 170-179.
- (2) Zabarnick, S. *Ind. Eng. Chem. Res.* **1993**, *32*, 1012-1017.
- (3) Zabarnick, S. *Energy Fuels*. **1998**, *12*, 547-553.
- (4) Kuprowicz, N.J.; Ervin, J.S.; Zabarnick, S. *Fuel*. **2004**, *83*, 1795.
- (5) Ervin, J.S.; Zabarnick, S. *Energy Fuels*. **1998**, *12*, 344-352.
- (6) Doughtip, T.; Ervin, J.S.; Zabarnick, S.; Williams, T.F. *Energy Fuels*. **2004**, *18*, 425.
- (7) Balster, L.M.T.; Zabarnick, S.; Striebich, R.C. *Prepr.-Am. Chem. Soc., Div. Pet. Chem.* **2002**, *47*, 161.
- (8) Doughtip, T. Thesis, University of Dayton, 2004.
- (9) Nikolaeva, E.V.; Shamov, A.G.; Khrapkovskii, G.M.; Kharlampidi, K.E. *Russ. J. Gen. Chem.* **2002**, *72*, 748.
- (10) Denisova, T.G.; Emel'yanova, N.S. *Kinetics and Catalysis*. **2003**, *44*, 441.
- (11) Sebban, N.; Bockhorn, H.; Bozzelli, J.W. *Phys. Chem. Chem. Phys.* **2002**, *4*, 3691.
- (12) Zabarnick, S.; Mick, M.S. *Ind. Eng. Chem. Res.* **1999**, *38*, 3557.
- (13) West, Z.; Zabarnick, S.; Striebich, R.C., *Ind. Eng. Chem. Research.*, submitted for publication, 2004.
- (14) Bach, R.D.; Dmitrenko, O. *J. Phys. Chem. B*. **2003**, *107*, 12851-12861.

COMPUTATIONAL CHEMICAL KINETICS OF HYDROCARBON AND CHLORINATED HYDROCARBON SPECIES IN COMBUSTION AND PYROLYSIS

Vadim D. Knyazev

Research Center for Chemical Kinetics, Department of Chemistry
The Catholic University of America, Washington, DC 20064

and

National Institute of Standards and Technology
Physical and Chemical Properties Division, Gaithersburg, MD 20899

Introduction

Kinetic modeling of processes such as the combustion and pyrolysis of hydrocarbon-based fuels is essential for understanding their mechanisms and for use of these mechanisms as tools of prediction and control. The success of such modeling is currently limited by a lack of fundamental information on the rates and products of a large number of elementary reactions. This presentation will focus on recent computational studies of the kinetics and mechanisms of reactions important in the combustion and pyrolysis of hydrocarbons and chlorinated hydrocarbons.

New methods of evaluating reaction energy barriers and rate constants were developed: IRTS (Isodesmic Reactions for Transition States) and RESLIR (Reactivity Extrapolation from Small to Large Molecular Systems via Isodesmic Reactions for Transition States).

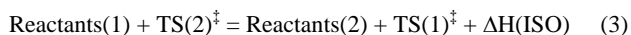
The individual reactions studied include atomic abstraction reactions, a series of reactions of molecular cycloaddition, addition of radicals to double bonds, and reactions of thermally and chemically activated decomposition of chlorinated hydrocarbon radicals.

Isodesmic Reactions for Transition States (IRTS)

Isodesmic reactions,¹ i.e., (usually) fictitious reactions that conserve the types of chemical bonds and their numbers, are often used in computational thermochemistry. Enthalpies of these reactions are usually obtained in quantum chemical calculations and it is expected that computational errors that are specific to a particular bond type will, to a large extent, cancel on both sides of the chemical equation. The IRTS method^{2,3} applies the same formalism to transition states. For example, for any two reactions of the same class expressed via chemical equations

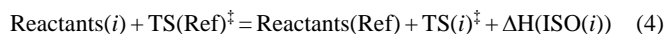


one can write a formal isodesmic reaction



provided that the class of reactions is defined by the similarity of the chemical transformations taking place and the structures of the transition states ($\text{TS}(i)^{\ddagger}$ where i is the reaction number).

In the IRTS technique, first, the energy barrier $E(\text{Ref})$ for one of the reactions within the reaction class (a "reference" reaction) is evaluated on the basis of reliable experimental data on the temperature dependence of the reaction rate constant, $k(T)$. Then, for all other reactions within the class, formal isodesmic reaction schemes of the type



are written and their 0 K enthalpies, $\Delta H(\text{ISO}(i))$, are obtained in quantum chemical calculations. Here, $\text{Reactants}(\text{Ref})$ and $\text{TS}(\text{Ref})^{\ddagger}$ are the reactants and the transition state for the "reference" reaction and i is the reaction number. Finally, energy barriers for all cognate reactions are calculated using the values of $E(\text{Ref})$ and $\Delta H(\text{ISO}(i))$:

$$E(i) = E(\text{Ref}) + \Delta H(\text{ISO}(i)) \quad (I)$$

The values of $\Delta H(\text{ISO}(i))$ are expected to be accurate due to cancellation of errors on both sides of the chemical equation (4); this accuracy is expected to propagate into the values of $E(i)$. Note that for any two reactions within the class (reactions 1 and 2), the 0 K enthalpy of the isodesmic reaction (3) equals the difference in the energy barriers of these reactions. Thus, the primary postulation of the IRTS technique is equivalent to the assumption that, although a particular quantum chemical method may not yield accurate absolute values of energy barriers, differences between the energy barriers of individual reactions can be calculated with a high degree of accuracy for a series of reactions of the same type.

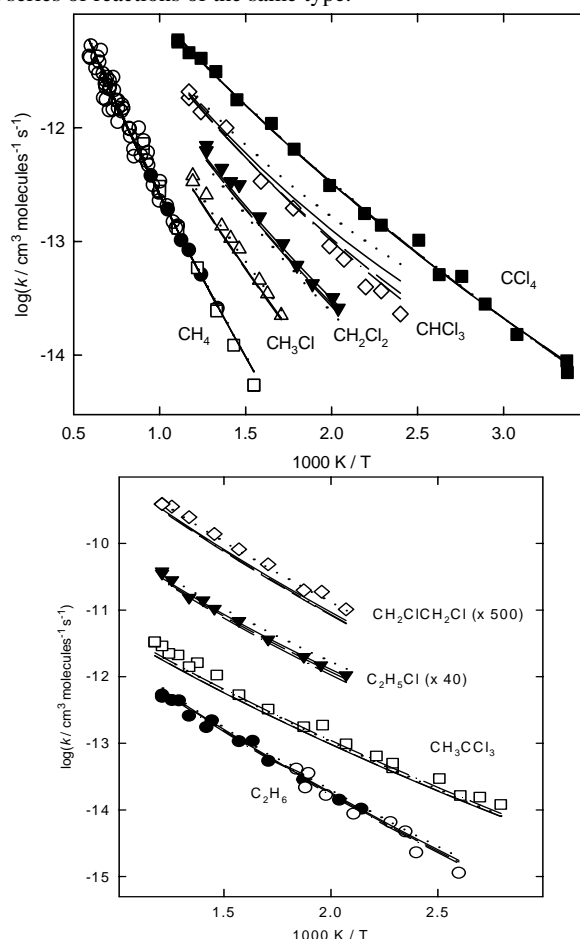


Figure 1. Experimental and computational results on the rate constants of the reactions of H atoms with methane, ethane, and chlorinated methanes and ethanes. All experimental data are from refs 4 and 5 except for the reactions of CH_4 and C_2H_6 , where results of other direct studies are also shown by open symbols (CH_4 : open circles, ref 6; squares, ref 7. C_2H_6 : open circles, ref 8). Lines are the results of computations with the IRTS method. Different lines correspond to different quantum chemical techniques applied within the framework of the IRTS method.

The IRTS technique has been applied^{2,3} to three classes of reactions: abstraction of H by an H atom, abstraction of Cl by an H atom (from chloroalkanes), and abstraction of H by a Cl atom from halogenated methanes. These studies demonstrated that the IRTS approach yields very high accuracy in predicting reactivity. For example, average deviations between calculated and experimental rate constants for the seven H + chloroalkane reactions considered in ref 2 are only 17 – 24 %, depending on the quantum chemical method used within the IRTS technique.

The RESLIR method

The RESLIR method⁹ is based on the use of the IRTS technique to extrapolate reactivity from small to large molecular systems within the same class of reactions. Unlike the previous applications^{2,3} of the IRTS technique, it does not rely on the existence of extensive experimental information on the kinetics of at least one reaction within the class. Instead, high-level predictive calculations are performed for the reference reaction, which is chosen in such a way as to include only small molecules.

The algorithm of the RESLIR method is as follows.

1. A class of reactions is defined by the similarity of the chemical transformations occurring and the structures of the transition states. This class includes reactions involving both small and large molecules.
2. Within this class, a "reference" reaction involving only molecules of small sizes is chosen.
3. Two quantum chemical methods of different levels are selected: a low-level (LL) method and a high-level (HL) method.
4. High-level quantum chemical calculations are performed for the "reference" reaction to evaluate its energy barrier.
5. For other reactions of interest within the same class, including reactions involving large molecules, isodesmic reaction schemes of the type given by equation 4 are designed. 0 K enthalpies of these reactions, $\Delta H(\text{ISO}(i))$, are computed at the low level of theory.
6. Finally, energy barriers of the reactions of interest are calculated using the relationship of equation 1.

The notation RESLIR(HL|LL) is used to indicate the HL and the LL methods used within the RESLIR algorithm.

Evaluation⁹ of the RESLIR method demonstrates the validity of this approach. The accuracy in determination of energy barriers achieved by using low-level quantum chemical calculations to extrapolate the high-level results for reference reactions to reactions involving larger species is clearly better than that obtained if low-level calculations alone are used. Predictive performance of the method was evaluated for two classes of reactions: eleven Diels-Alder reactions and twenty reactions of the addition of CH_3 and CF_3 radicals to $\text{C}=\text{C}$ double bonds. Fig. 2 illustrates one of the tests of the extrapolative ability of the RESLIR method.

Potential Energy Surfaces and Kinetics of the Reactions of Decomposition of Chlorinated Hydrocarbon Radicals

Cl atom departure reactions. Two reactions of decomposition of chlorinated hydrocarbon radicals where reactions occur via elimination of a chlorine atom and formation of a π bond were studied experimentally and computationally.^{10,11}



In these reactions, the minimum energy paths pass through shallow regions on the PES with energies below those of the separated products. Quantum chemical calculations demonstrate that the PES

of reactions 5 and 6 bears similarity to that of the earlier studied reaction¹²



However, reactions 5 and 6 differ from the $\text{CH}_2\text{CH}_2\text{Cl}$ decomposition by the existence of saddle points between the equilibrium radical configurations and those of the shallow "departure" complexes. The potential energy surface of reaction 6 is shown in Fig. 3.

The results of quantum chemical calculations, the rate constant values obtained in the experimental study, and literature data on the reverse reactions of addition of Cl to π bonds were used to create models of reactions 5 and 6. The experimental dependences of the rate constants of the forward and the reverse reactions on temperature and pressure were reproduced in RRKM / master equation calculations. Fig. 4 illustrates the agreement between the experimental and the computational results on the rate constants of reaction -6, that of addition of Cl to allene to form 2-chloroallyl radical.

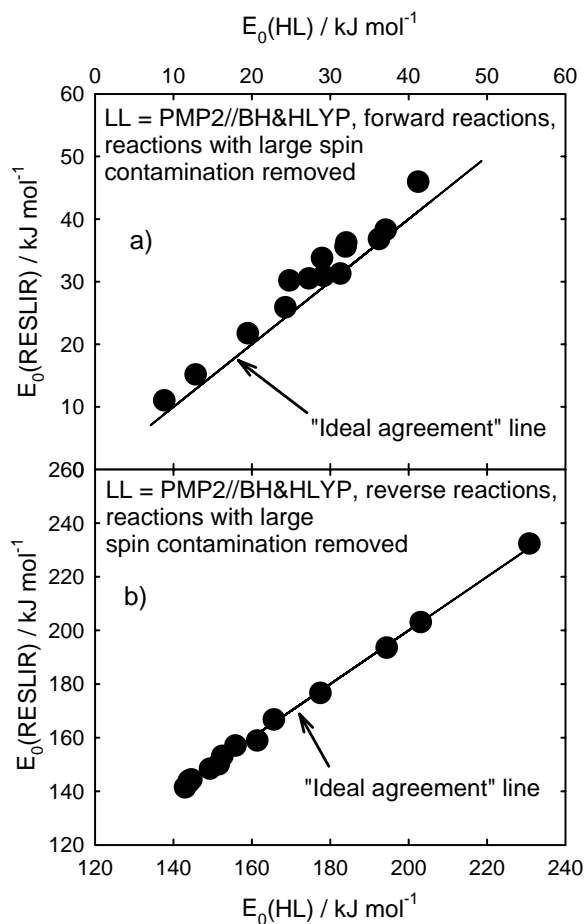


Figure 2. Extrapolative ability of the RESLIR method. Energy barriers obtained in RESLIR calculations using LL = PMP2//BH&HLYP and HL = CCSD(T)//BH&HLYP (all with the cc-pVDZ basis set) vs those obtained in HL (high-level) calculations for 20 reactions of addition of CH_3 and CF_3 to $\text{C}=\text{C}$ double bonds with six reactions significantly affected by spin contamination removed. Data are presented for the forward and the reverse reactions.

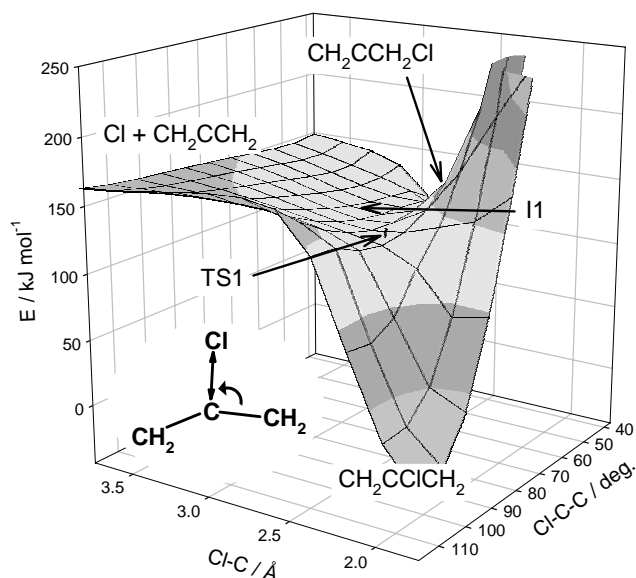


Figure 3. 3-dimensional surface plot obtained in a relaxed scan of the PES of reaction 6 using the BH&HLYP/6-311G(d,p) method. The minimum energy path of the $\text{CH}_2\text{CClCH}_2$ dissociation to $\text{Cl} + \text{CH}_2\text{CCH}_2$ proceeds from the $\text{CH}_2\text{CClCH}_2$ equilibrium structure through the saddle point TS1 (indicated by a short vertical dash) and the I1 plateau. The inset on the left shows the coordinated scanned: the C-Cl distance and the Cl-C-C angle.

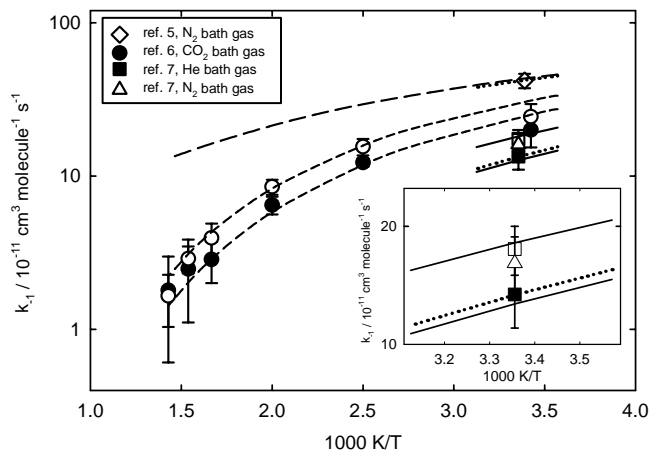
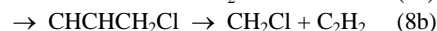


Figure 4. Experimental (symbols) and calculated (lines) rate constants of reaction -6. Experimental data are from refs 13 (diamond), 14 (filled circles, 5 Torr of CO_2 , and open circles, 10 Torr of CO_2), and 15 (filled square, 5 Torr of He, open square, 10 Torr of He, and triangle, 5 Torr of N_2). Lines are the results of modeling: long-dash dashed line, the high-pressure-limit rate constants; short-dash dashed lines, $k_1(T)$ for the conditions of ref 14 (5 and 10 Torr of the CO_2 bath gas); solid lines, $k_1(T)$ for the conditions of ref 15 in He bath gas (5 and 10 Torr); dotted lines, $k_1(T)$ for N_2 bath gas under the conditions of refs 15 (5 Torr) and 13 (760 Torr). The inset enlarges the part of the plot showing the k_1 values of ref 15 and the corresponding calculated lines.

Reactions on the PES of 1-chloroallyl radical. The reaction of decomposition of 1-chloroallyl radical



as well as the related reaction of the chloromethyl radical with acetylene



were studied computationally using quantum chemical investigations of the potential energy surfaces, RRKM, and Master Equation techniques. The results indicate that the mechanism of reaction 9 is quite different from that of its non-chlorinated analog ($\text{CH}_3 + \text{C}_2\text{H}_2 \rightarrow \text{H} + \text{C}_3\text{H}_4$)¹⁶⁻¹⁹: chemically activated isomerization of the adduct via a 1,3 Cl atom transfer is an important channel leading to the formation of the resonantly stabilized 1-chloroallyl radical. The results have implications for the pathways of aromatics and soot formation in the combustion of chlorinated hydrocarbons: chloroallyl radicals, due to their stability, are likely to accumulate in large concentrations and lead to molecular mass growth via recombination reactions. Similarly, a fraction of thermal decomposition of 1-chloroallyl radical (reaction 8) occurs via a 1,3 Cl atom shift to form CHCHCH_2Cl with subsequent dissociation into $\text{CH}_2\text{Cl} + \text{C}_2\text{H}_2$.

Acknowledgement. This research was supported by the National Science Foundation, Combustion and Thermal Plasmas Program under Grants No. CTS-9807136 and CTS-0105239, and, in part, by the Division of Chemical Sciences, Office of Basic Energy Sciences, Office of Energy Research, U.S. Department of Energy under Grant No. DE/FG02-98ER14463.

References

1. Hehre, W. J.; Ditchfield, R.; Radom, L.; Pople, J. A. *J. Am. Chem. Soc.* **1970**, *92*, 4796.
2. Knyazev, V. D. *J. Phys. Chem. A* **2002**, *106*, 11603.
3. Knyazev, V. D. *J. Phys. Chem. A* **2003**, *107*, 11082.
4. Bryukov, M. G.; Slagle, I. R.; Knyazev, V. D. *J. Phys. Chem. A* **2001**, *105*, 3107.
5. Bryukov, M. G.; Slagle, I. R.; Knyazev, V. D. *J. Phys. Chem. A* **2001**, *105*, 6900.
6. Sutherland, I. W.; Su, M.-C.; Michael, J. V. *Int. J. Chem. Kinet.* **2001**, *33*, 669.
7. Knyazev, V. D.; Bencsura, A.; Stoliarov, S. I.; Slagle, I. R. *J. Phys. Chem.* **1996**, *100*, 11346.
8. Jones, D.; Morgan, P. A.; Purnell, J. H. *J. Chem. Soc. Faraday Trans. 1* **1977**, *73*, 1311.
9. Knyazev, V. D. *J. Phys. Chem.* **2004**, *108*, on the web.
10. Bryukov, M. G.; Kostina, S. A.; Knyazev, V. D. *J. Phys. Chem. A* **2003**, *108*, 6574.
11. Shestov, A. A.; Popov, K. N.; Knyazev, V. D. *Manuscript in Preparation* **2004**.
12. Knyazev, V. D.; Kalinovski, I. J.; Slagle, I. R. *J. Phys. Chem. A* **1999**, *103*, 3216-3221.
13. Wallington, T. J.; Skewes, L. M.; Siegl, W. O. *J. Photochem. Photobiol. A* **1988**, *45*, 167.
14. Farrell, J. T.; Taatjes, C. A. *J. Phys. Chem. A* **1998**, *102*, 4846.
15. Atkinson, D. B.; Hudgens, J. W. *J. Phys. Chem. A* **2000**, *104*, 811.
16. Kislitsyn, M. N.; Slagle, I. R.; Knyazev, V. D. *Proc. Combust. Inst.* **2002**, *29*, 1237.
17. Wang, B.; Hou, H.; Gu, Y. *J. Chem. Phys.* **2000**, *112*, 8458.
18. Davis, S. G.; Law, C. K.; Wang, H. *J. Phys. Chem. A* **1999**, *103*, 5889.
19. Diau, E. W.; Lin, M. C.; Melius, C. F. *J. Chem. Phys.* **1994**, *101*, 3923.

TOWARD A SYSTEMATIC VALIDATION OF QUANTUM CHEMISTRY IN COMPUTATIONAL KINETICS

Carlos A. Gonzalez

Computational Chemistry Group
Physical and Chemical properties Division
National Institute of Standards and Technology
Gaithersburg, MD. 20899

Introduction

The use of modern computational chemistry methodologies in the prediction of molecular properties has become increasingly popular mainly due to significant improvements in the algorithms, the accuracy of the methods, and the advent of powerful computer resources. This is particularly true in the area of thermochemistry, where researchers in industry and academia perform quantum chemistry calculations on a routine basis. Despite this progress, the use of similar methodologies in computational kinetics has been slow. In fact, computational kinetics remains an obscure area being used most of the time by experts in the field. There is no doubt that the application of quantum chemistry calculations in the area of computational kinetics will have a significant impact. In order for this to happen, however, it is critical that reliable state-of-the-art methodologies be widely available to the scientific community. In order to achieve this goal, an exhaustive and systematic validation of these methodologies is necessary. However, in stark contrast to the case of thermochemistry, determining error bounds in the properties computed by quantum chemistry methods necessary for the prediction of rate constants have been found to be a daunting task. This is particularly true in the case of reaction barriers, ΔE^\ddagger , where the determination of error bounds is particularly difficult due to the impossibility of directly measuring these quantities in kinetics experiments where the only observable is a rate constant $k(T)$ that varies with temperature and sometimes with pressure.

In general, theoretical computations of rate constants involving quantum chemistry calculations require at least three phases: (1) the determination of the reaction mechanism that will provide with the reactants, pre- and post-reactive complexes if any, transition structures and products involved in the reaction (2) the calculation of the energetics (i.e. heat of reactions and reaction barriers) and (3) the calculation of the rate constants adopting a particular kinetics model. It is common practice to “validate” a particular quantum chemistry methodology by direct comparison of the computed rate constants and the corresponding experimental values. However, the computation of uncertainty in theoretical reaction barriers is a complicated process that depends on numerous factors such as the validity of the reaction mechanism adopted, the kinetics model used to compute the rate constants, the uncertainty of the experimental rate constants and the inherent uncertainty of the quantum chemistry methods used. A “good agreement” between the theoretical and experimental $k(T)$ ’s does not necessarily indicate that the computed reaction barrier is the correct one given that this agreement could be the result of fortuitous and non-systematic cancellations of errors. A popular procedure to “measure” the uncertainty of the computed barriers is the comparison of these quantities with the activation energies, E_a , extracted from fits of the temperature dependence of the rate constants obtained experimentally (Arrhenius plots). Unfortunately, this approach has no validity given that the E_a ’s experimentally obtained are just phenomenological constants that do not have any formal relation with the “actual” reaction barrier. It would appear then that the estimation of global uncertainties in the

case of theoretical ΔE^\ddagger ’s is an intractable problem, and that any attempt to compute error bounds on theoretical barriers will have to be done within the realm of a series of specific approximations and a particular kinetic model used. In this talk, the difficulties related to the validation process of quantum chemistry methods in computational kinetics will be discussed. In addition, possible strategies that could potentially lead to a systematic approach in the validation of these methodologies will also be presented.

Theoretical Approach

In this talk we will adopt the Transition State Theory¹ (TST) as the kinetic model used to compute rate constants. According to this theory, for a bimolecular reaction in gas phase, $k(T)$ is given by the following expression:

$$k(T) = \Gamma(T) \times \frac{k_B T}{h} \times \frac{Q_{TS}(T)}{Q_A(T) Q_B(T)} \times \exp\left(-\frac{E_0}{k_B T}\right) \quad (1)$$

where: $Q_A(T)$, $Q_B(T)$ and $Q_{TS}(T)$ are the total partition functions for reactants A, reactants B and transition state at temperature T ; E_0 is the barrier height computed as the difference in energies between transition states and reactants, including zero-point energy corrections ($E_0 = \Delta E^\ddagger + \Delta ZPE$; $\Delta E^\ddagger = E_{TS} - E_A - E_B$; $\Delta ZPE = ZPE_{TS} - ZPE_A - ZPE_B$); k_B is Boltzman’s constant; and h Planck’s constant. $\Gamma(T)$ in equation (1) indicates the corresponding tunneling correction² at temperature T . The calculation of the reaction rate constants using the TST formulation given by Eq. (1) requires the proper computation of the partition functions of reactants and the transition states. The total partition function $Q_X(T)$ of species X ($X = A, B$ or TS) can be cast in terms of the translational (Q_T), electronic (Q_e), rotational (Q_R) and vibrational (Q_V) partition functions:

$$Q_X(T) = Q_T^X(T) Q_e^X(T) Q_R^X(T) Q_V^X(T) \quad (2)$$

Close examination of the formal expressions for the partition functions $Q_X(T)$ and the TST rate expression given by Eq. (1) leads to the conclusion that the determination of uncertainties of the reaction barriers ΔE^\ddagger computed with a particular quantum chemistry methodology using experimental rate constants is a daunting task that is complicated by the existence of important tunneling effects and the fact that it is impossible to directly estimate the accuracy of the computed partition functions corresponding to the transition state, given that these quantities are not available from the experiments. Although these critical issues make it difficult if not impossible the determination of uncertainties in the theoretical barriers, it is possible to reduce the scope of this task by imposing constraints based on certain approximations regarding tunneling and the nature of the transition state. As an example to illustrate this point, we make use of the following approximations in this talk:

- 1.- The kinetics of the reacting system is appropriately described by TST.
- 2.- Tunneling corrections are negligible.
- 3.- The uncertainty in $Q_{TS}(T)$ is exactly the same as the uncertainty computed in the case of reactant’s partition functions.

The first approximation limits the validity of this study to cases where the three basic premises underlying TST are applicable¹: no surface re-crossing is allowed; there is no coupling between the tangent vector along the minimum reaction path and other degrees of freedom; and the dynamical bottleneck is located at the saddle point of the potential energy hypersurface. The second approximation can be satisfied if the reaction under study is not significantly affected by tunneling corrections. In this work, we have chosen a series of hydrogen-abstraction reactions at sufficiently high temperature where tunneling corrections are known to be close to unity. This is a very critical step, given that it is very difficult to consider the accuracy in

the reaction barriers if the computed rate constants depend on the model used to treat tunneling effects. The third approximation is very strong and it maybe the hardest to support in a formal manner. Given the nature of the transition structures, where bonds are partially formed and broken, it is not necessary true that the quantum methodologies currently in used will exhibit uncertainties similar to the ones obtained in the case of minima such as reactants and/or products. In particular, due to the lack of vibrational frequencies for transition states, it is impossible to determine the relative accuracy of electronic structure methodologies in the prediction of the partition functions, very important in the calculation of the partition functions. Once these three approximations are made and the appropriate set of reactions is chosen, the uncertainty in the computed reaction barriers can be obtained by comparison with the “experimentally extracted barriers”, $E_0^{\text{exp}t}$, obtained from Eq. (1) and the experimental rate constants and their standard uncertainty. This is easily done after introducing the experimental rate constants into Eq. (1) and rearranging:

$$E_0^{\text{exp}t}(\pm\sigma) = k_b \cdot T \cdot [\ln(k_b/h) + \ln T + \ln Q(T) - (1/k_b T)(\Delta ZPE) - \ln k^{\text{exp}t}(T)] \quad (3)$$

where the errors in T , $k^{\text{exp}t}(T)$, $Q(T)$, ΔZPE have been propagated and the term $Q(T)$ is given by:

$$Q(T) = \frac{Q_{\text{TS}}(T)}{Q_{\text{A}}(T)Q_{\text{B}}(T)}$$

Computational Details. In this work, all reactants, transition states and products were fully optimized with the Coupled Clusters³ in the space of single and double electron excitations (CCSD) using the double-zeta plus polarization and diffusion Pople’s basis set⁴ 6-311++G**. Harmonic frequency calculations were performed at the same level of theory (CCSD/6-311++G**). Reaction Barriers and heats of reactions were computed by performing single point calculations on the CCSD/6-311++G** geometries with Couple Clusters in the space of single and double electron excitations to which triple excitations have been added perturbatively (CCSD(T)). The same basis sets were used.

Results

As an example illustrating the principles behind the methodology proposed in this work, we show results for the simple abstraction reaction $\text{H} + \text{CH}_4 \rightarrow \text{CH}_3 + \text{H}_2$. Figure 1 depicts the temperature dependence of $k(T)$ in the high-temperature regime as measured by different researchers. Except for the recommendation by Baulch, most of the measurements seem to agree reasonably well with each other. These data sets, together with their uncertainties were used in order to extract the corresponding values of $E_0^{\text{exp}t}$ as computed by Eq. (3). The results are shown in Figure 2, where the barrier height computed by at the CCSD(T) level of theory described before is included for comparison purposes. The results shown in Figure 2 indicate that despite the reasonable agreement between the different experiments observed in Figure 1, the corresponding experimentally extracted barriers differ significantly. The most surprising observation is the marked temperature dependence of the $E_0^{\text{exp}t}$ values. As Figure 2 indicates, the results by Knyazev and Slagle as well as the results obtained by the recommended rate expressions of Baulch show a significantly smaller temperature dependence. Although the source of the temperature dependence on the experimentally reaction barrier is not well understood, this

example shows the complexities involved in the validation of quantum chemistry methodologies when computing barrier heights.

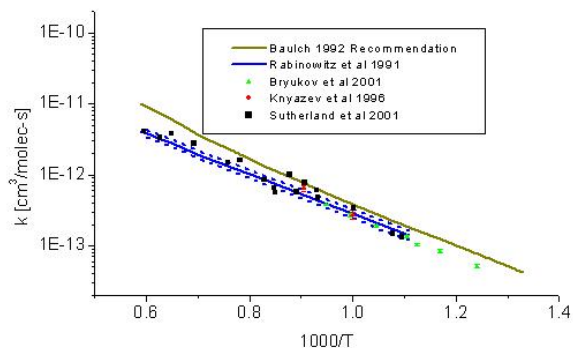


Figure 1. $k(T)$ vs T for $\text{H} + \text{CH}_4 \rightarrow \text{CH}_3 + \text{H}$ as measured by different research groups.

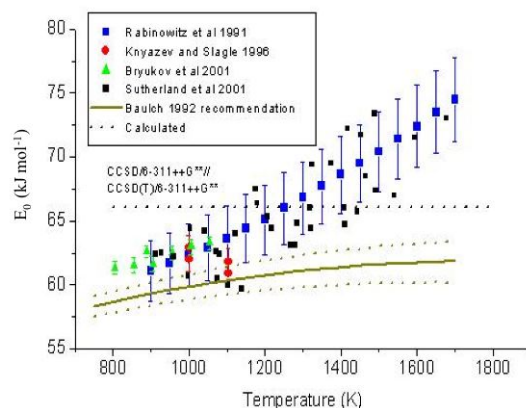


Figure 2. Experimentally extracted barrier heights for the reaction $\text{H} + \text{CH}_4 \rightarrow \text{CH}_3 + \text{H}$ using different experimentally measure rate constants..

Conclusions

In this work critical issues in the validation of quantum chemistry methodologies in the computation of reaction barrier heights and their application in computational kinetics is discussed. It is shown that contrary to the case of thermochemistry, the computation of the uncertainty of theoretical barrier heights is a daunting task due to the impossibility of measuring barrier heights. Finally, it is shown that the use of approximated procedures based on a list of reasonable assumptions could be a valuable alternative in the estimation of error bounds in the computed barriers when using a particular kinetics model.

References

- (1) (a) Johnston, H. S. *Gas Phase Reaction Rate Theory*; The Roland Press Company: New York, 1966. (b) Laidler, K.J. *Theories of Chemical Reaction Rates*, McGraw-Hill: New York, 1969. (c) Weston, R.E.; Schwartz, H.A. *Chemical Kinetics*, Prentice-Hall: New York, 1972. (d) Rapp, D. *Statistical Mechanics*, Holt,

- Reinhard, and Winston: New York, 1972. (e) Nikitin, E.E. *Theory of Elementary Atomic and Molecular Processes in Gases*, Clarendon Press: Oxford, 1974. (f) Smith, I.W.M. *Kinetics and Dynamics of Elementary Gas Reactions*, Butterworths: London, 1980. (g) Steinfeld, J.I.; Francisco, J.S.; Hase, W.L. *Chemical Kinetics and Dynamics*, Prentice-Hall: New Jersey, 1989.
- (2) See for instance (a) Garret, B.C.; Truhlar, D.G.; *J. Phys. Chem.* **1979**, 83, 2921. (b) Garret, B.C.; Truhlar, D.G. *J. Chem. Phys.* **1984**, 81, 309. (c) Skodke, R.T.; Garret, B.C.; Truhlar, D.G. *J. Phys. Chem.* **1981**, 85, 3019. (d) Skodje, R.T.; Garret, B.C.; Truhlar, D.G. *J. Chem. Phys.* **1982**, 77, 5955. (e) Garret, B.C.; Truhlar, D.G.; Grev, R.S. Magnuson, A.W. *J. Chem. Phys.* **1980**, 84, 1730. (f) Garret, B.C.; Truhlar, D.G.; Grev, R.S. Magnuson, A.W. *J. Chem. Phys.* **1983**, 87, 4554. (g) Miller, W.H.; Shi, S.-h. *J. Chem. Phys.* **1981**, 75, 2258. (h) Miller, W.H.; Smith, F.T. *Phys. Rev.* **1978**, A 17, 939. (i) Wigner, E.P. *Z. Phys. Chem.* **1932**, B19, 203.
- (3) (a) Bartlett, R.J.; Purvis, G.D. *Int.J.Quantum.Chem.* **1978**, 14, 516. (b) Cizek, J. *Adv.Chem.Phys.* **1969**, 14, 35. (c) Purvis, G.D.; Bartlett, R.J. *J.Phys.Chem.* **1982**, 76, 1910. (d) Scuseira, G.E.; Janssen, C.L.; Schaefer, H.F., III *J.Chem.Phys.* **1988**, 89, 7382. (e) Scuseira, G.E.; Schaefer, H.F., III *J.Chem.Phys.* **1989**, 90, 3700. (f) Pople, J.A.; Head-Gordon, M.; Raghavachari, K. *J.Chem.Phys.* **1987**, 87, 5968.
- (4) Descriptions of the Pople-style basis sets can be found in the following: Foresman, J.B.; Frisch, A.E. *Exploring Chemistry with Electronic Structure Methods* 2nd Ed.; Gaussian, Inc.: Pittsburgh, PA, 1996

THE NIST CHEMICAL KINETICS DATABASE AS A TOOL FOR MODELING

Thomas C. Allison

Physical and Chemical Properties Division
National Institute of Standards and Technology
100 Bureau Drive, Stop 8380
Gaithersburg, Maryland 20899-8380

Introduction

One of the most challenging aspects of creating predictive models is gathering the relevant data. Often data are hard to find or are in an inconvenient format. Reliably establishing the scientific pedigree of the data often presents a significant challenge as well. Within the chemical kinetics community, the NIST Chemical Kinetics Database is a major resource used to gather data on gas-phase chemical reactions. The data are useful for validating current models and constructing predictive models where data on elementary rate constants is needed. The advent of new computer technologies and standards offers is substantially impacting the way scientists work. NIST continues to explore new ways of delivering information in ways that make this information easily useable and targeted to users needs. In this talk an overview of the NIST Chemical Kinetics Database will be given with particular attention paid to newly developed and planned functionalities address the above concerns.

Database Overview

The NIST Chemical Kinetics Database is a collection of data on rates of gas-phase chemical reactions abstracted from the literature. This data is freely accessible at <http://kinetics.nist.gov/>. The web implementation of the database incorporates a number of useful features designed to assist the user in quickly finding the desired information. What follows is a summary of the basic functionality of the database. Information on advanced features will be presented later in this paper. One of the most important features is the search engine. Users are able to search for rate constants by specifying all or part of a chemical reaction or by searching the bibliographies on a number of criteria (e.g. author, year, words in title). Chemical species may be identified by one or more names, CAS registry number, or chemical formula. When multiple kinetics results are obtained via a search they are grouped by reaction type for easy access. Kinetics data may be viewed in summary or detailed form. The detailed form includes a table of rate constant values over the range of valid temperatures. Users have complete control over the units user to present the data. The database will convert all units as needed. Multiple rate expressions may be plotted when a graphical representation is desired.

The remainder of this paper is organized as follows. The organization of the database is described in some detail. A summary of new and planned features for the database is presented. An overview of some of the technologies employed by the database are described. The usefulness of the database for validation and model creation will be discussed with particular emphasis on new features. Finally, a number of future directions for database development are presented.

Database Organization

The design of a database is important for its overall function. In the following sections, the design and content types of various parts of the database are described. Though the data schema described here is realized in a relational database, it will be shown that these concepts will apply when the data is delivered in other formats.

The NIST Chemical Kinetics Database contains three major types of data: bibliography, chemical species, and kinetics data. The bibliography data include all of the expected fields (e.g. year, authors, journal, title, pages). The chemical species data include common and systematic names, CAS registry numbers, and chemical and semistructural formulas. The kinetics data is conveniently viewed as a collection of smaller data types: chemical reaction, rate expression, pressure dependence, rate data, metadata (descriptive information about the rate constant), and reviewer comments. Each of these data types is now discussed in more detail.

Chemical Reaction. In order to specify a chemical reaction, at least one reactant is required, though more reactants may be specified. If the product(s) of the chemical reaction is(are) known, then at least one product must be specified. In many cases, the product(s) of a chemical reaction are not known, they need not be specified. In cases where the rate constant measurement is a relative one, the relative reaction must be specified as described above. Reaction orders are collected for each reaction specified.

Rate Expression. All rate expressions are collected as coefficients of two- or three-parameter Arrhenius expressions. Uncertainties associated with individual parameters or with the overall fit and valid temperature and pressure ranges are captured as well. Data are always captured in the units used in the reference.

Pressure Dependence. The data necessary to specify the pressure dependence of a rate expression is now stored in the database. The temperature and pressure ranges for which the pressure dependent rate expression is valid are captured as well as the parameters of the particular pressure dependence equation.

Rate Data. Data on individual rate constants (at a specified temperature and pressure) is now stored in the database. Uncertainties associated with each measurement are captured.

Metadata. Each rate constant in the Chemical Kinetics Database is characterized by as many as six descriptors. Each of these descriptors has a controlled list of keywords associated with it. The six categories are data type, experimental procedure, excitation technique, time resolution, pressure dependence, and analytical technique. By using controlled keyword lists, it is possible to broadly classify a large number of abstracted data in a meaningful way.

Reviewer Comments. One of the value-added features of the Chemical Kinetics Database is that data abstracters make comments on some aspect of the paper. Frequently these provide valuable insight into key aspects of the rate constant determination.

New Features

A number of new features have been added to the database recently, and several others are planned or being implemented at this time. Each of these is discussed briefly below.

Pressure Dependence. The ability to combine low- and high-pressure limit rate expressions to provide pressure-dependent rate expressions has been added to the database recently. In the initial implementation, a constant expression, an expression due to Troe, and an expression used by the NASA data panel are allowed. Additional expressions for pressure dependence are under consideration. It is expected that this functionality will dramatically increase the usefulness of the database for many users. This data is presented in a tabular form and may also be plotted.

Rate Data. In many cases, researchers are interested in the actual data collected in an experiment or calculated by a theoretical procedure rather than a fit of Arrhenius expression parameters to the data. The capability of capturing individual data points with associated uncertainties at a specified temperature and pressure has been added to the database recently. New tools will allow users of

the database to refit the data or combine it with other data to obtain a new rate expression for a particular chemical reaction.

Collections. The concept of a collection is similar to that of the "shopping cart" when purchasing items online. The NIST Chemical Kinetics Database allows users to create collections of data while using the database. Items in the collection may be viewed, plotted, printed, or output in several formats. The collection may be expanded or reduced as needed.

Output Formats. To facilitate easy use of data obtained from the NIST Chemical Kinetics Database, output may be obtained in several new formats. Individual (or a collection of) rate constants may be output in the familiar "NASA polynomial" format for direct import into modeling or other codes which accept this format. Collections of rate constants may also be saved in a spreadsheet format for further analysis. Collections of bibliographic data may be output in a format suitable for import to several popular citation software packages.

Print Layout. New stylesheets designed specifically for printing database results have been added to the database. This allows users to print a high-quality copy of their results for archival or other use.

Speed. The database schema and code have been redesigned to return results faster than ever. Previous performance was very acceptable, but the latest release of the database should provide an even more satisfying user experience.

Technologies

The NIST Chemical Kinetics Database has been built on a foundation of modern web tools. Among the design goals for the database were ease-of-use, portability, reliability, and speed. We have attempted to select tools which meet each of these needs. There are many such tools available, and it is often difficult to select the combination which best addresses the problem at hand. Nevertheless, certain tools and design practices have emerged and are considered "best practices" for web development. The development of the database on the web has followed these "best practices" to the greatest extent possible. In the following sections, certain products will be mentioned. This does not constitute an endorsement by the National Institute of Standards and Technology. Other products may be as good or better for the intended purpose.

The database server has several distinct parts. The "back-end" is the database server. We are currently using the MySQL relational database system. The requirement is simply a database server which understands SQL, and there are many such database systems available. The choice of SQL for database communication allows considerable flexibility for future applications of the database.

The web pages are served by the Apache HTTP server which is widely used around the world. This provides with a robust and secure platform for the web site. Nevertheless, there are many other web servers available which could be used for the same purpose.

The software which implements the database features is written in Java. This decision was made largely for portability and because of the tight integration of Java to web technologies. Using Java in a web application requires some type of container. The current implementation of the database uses the Tomcat servlet container. Web pages are created using Java Server Pages (JSP) and Java Servlet technologies. The Java code is coupled to the database using Java Database Connectivity (JDBC) software.

The software described above implements a great deal of functionality of the database and serves as a solid foundation for the integration of new technologies which, in turn, enable exciting new functionalities. Perhaps the most important enabling technology for the Chemical Kinetics Database as its functionality is extended is the

extensible markup language (XML). XML has emerged as one of the best technologies for data exchange.

A number of tools for using and translating XML exist. The database code makes use of the Xerces XML parser and the Xalan XLST codes from the Apache Jakarta project to support various document operations.

The simple object access protocol (SOAP) is used for machine-to-machine communication between an agent on the user's computer and the database server. The SOAP implementation provided by the Apache Jakarta project, Axis, is used.

Modeling

To this point, a great deal of architecture has been described. How do the design goals and considerations and the host of web technologies work for the users of the database? What can a user accomplish now that was difficult or impossible a few years ago?

Proprietary data formats have presented and continue to present a considerable barrier to getting work done. Considerable time on many projects is spent converting data from one form to another. Each time a new format is encountered, one must spend time and effort learning how to retrieve the data before it can be used. The NIST Chemical Kinetics Database has the capability of returning any data record as an XML file. This file is completely described by an XML schema which is a formal description of the document content. Data returned by the database in this XML format may be validated as a quality assurance measure.

By retrieving XML content from the database, the modeler has a means of archiving data in a format which is readily understood by a large number of tools and can be readily manipulated and converted to the appropriate format.

Use Cases. One of the primary goals of the NIST Chemical Kinetics Database development is to enhance the user experience, in particular by decreasing the opportunity for errors and decreasing the time required to obtain the results of interest. In order to see how this might be accomplished, it is helpful to examine two use cases. In the first use case, a user who wants to validate research results against the available literature values is considered. This user's interaction with the database might involve the following steps:

- The user selects a chemical reaction of interest and enters this information into an agent.
- The agent queries the database for the selected reaction and returns the available data.
- The agent plots the user's data against selected results from the query. An assessment of the similarity to previous results is generated.
- The selected data is exported to the user's spreadsheet for further analysis.
- The agent remembers the query and the user's data and is able to automatically update the assessment upon request.

In this example it is seen that the user need enter a query only once and that this query might be updated at the push of a button. It is also seen that obtaining the data in a more useful format can be easily accomplished. The benefits increase when one considers repeating the procedure outlined above for many reactions. (Note that while some of this functionality exists in the current database, the software to accomplish all of the above steps does not exist. The example merely illustrates the possibilities allowed by the database architecture.)

As a second illustration, the use case of a research constructing a model is considered. The workflow might proceed as follows:

- The user creates a list of chemical reactions of interest and enters this information into an agent.

- The agent retrieves all information on all of the chemical reactions. The user selects the specific data of interest. The agent assists in the selection process by plotting the data and comparing to other related data.
- The data is saved in the NASA polynomial format for immediate input into a kinetic modeling program.
- Six months later, 15 of the reactions have updated experimental and theoretical rate constant determinations. The agent automatically flags these reactions for review and assists the user in updating the list of selected reactions and a new set of NASA polynomials is created.

In this use case considerable savings of time and effort are realized. The agent program identifies updated information at the push of a button and assists the user in updating the data of interest. The collection may be updated at any time with relatively little effort.

The two use cases presented serve as examples of the possibilities of automatically retrieving data over the web and processing it in a useful manner. Users with a particular need could write their own software to use the data in the manner most useful to them.

Future Directions

The expense and time involved in gathering and abstracting data for the NIST Chemical Kinetics Database is considerable. The volume of work in the field is increasing each year. It is becoming clear that a new method of gathering data for the database needs to be employed. One obvious solution is to have authors abstract their data when they submit their work to a journal. This technique is being successfully employed by the NIST Thermodynamics Research Center (TRC). In this model, NIST would distribute a tool to authors which would assist in the collection of the data. This tool would include a number of features designed to reduce errors on input. When the author is satisfied with the data to be submitted, it would be submitted to NIST via the journal. NIST would run additional quality checks on the data by comparing it to similar data or other models, report any errors to the authors for correction, and ultimately make the data available via the database. In this way authors are assured an accurate representation of their work and can make their data available as soon as the paper is published.

Human intervention in data collection is time consuming. Frequently a modeler has already specified the data that is needed for a particular project. Manually collecting this data, even via a savvy web interface, is a time consuming process. Using a communication protocol such as the simple object access protocol (SOAP) with XML, this process can be automated. In this model, the user's computer communicates a request to the database server, and the server sends back its response containing the requested data in a standard format. This data is then immediately useable in a model. When new values are added or when old values are changed, the process can be repeated with no need for human intervention. In this way, models can be kept current at the touch of a button.

NIST will provide the information on how users may gain SOAP access to the database and how to make further use of it. If there is sufficient interest, tools may be provided to perform common useful tasks. These tasks might include constructing a collection of NASA polynomials from a list of specific chemical reactions, return all data on a particular chemical reaction, and maintaining a bibliographic collection on a particular chemical reaction.

Sample code to demonstrate the basic principles outlined in this paper would serve as a building block for further development by motivated users with unique data needs. Such software may be made available if there is sufficient interest.

There are many other future directions for the NIST Chemical Kinetics Database. Part of the mission of NIST is to provide a high

level of service to its customers. Feedback on the database and, in particular, suggestions for improvement and new features are welcomed. Feedback may be submitted online, via a web form at <http://kinetics.nist.gov/>.

Conclusion

The NIST Chemical Kinetics Database has been described in considerable detail with an emphasis on new features, in particular those useful for constructing and validating chemical models. The role of current and emerging technologies in facilitating the use of such data has been discussed. Given the value of the data to researchers in a wide variety of fields, the NIST Chemical Kinetics Database remains one of the most valuable tools in chemical kinetics. Newly implemented and planned features should provide even greater value to database users.

Acknowledgement. Many people have contributed to the NIST Chemical Kinetics Database over the years. The original database was created by W.G. Mallard, F. Westley, J.T. Herron, R.F. Hampson, D.H. Frizzell. The web implementation was implemented by R.E. Huie, J.A. Manion, J.W. Hudgens, D.R. Burgess Jr., A. Fahr, R.D. Levin, C.-Y. Lin, W. Tsang, and T.C. Allison.

NO_x REMOVAL FROM LEAN EXHAUST: INSIGHTS FROM THERMODYNAMICS AND KINETICS OF NO_x DECOMPOSITION AND THERMAL REDUCTION WITH NH₃

William F. Schneider

Depts. of Chemical and Biomolecular Engineering and Chemistry
University of Notre Dame, Notre Dame, Indiana, 46556

Introduction

NO_x is an unavoidable and undesirable by-product of combustion in air. While very effective methods have been developed for the catalytic removal of NO_x from stoichiometric exhaust, NO_x removal from lean exhaust remains a challenge. In this work, we explore the limitations placed by thermodynamics on the direct catalytic decomposition of NO_x in air,¹ and then explore the thermodynamics and kinetics of so-called thermal deNO_x,² or non-catalytic NO_x removal by homogeneous reaction with NH₃.

Computational

Thermodynamic free energy minimization calculations were performed using the Chemkin-III³ interface to Stanjan. Density functional theory calculations were performed using the ADF code.⁴

Results and Discussion

The equilibrium concentration of NO_x in stoichiometric exhaust is many orders of magnitude less than that required by emissions control standards. In contrast, under lean combustion conditions equilibrium NO_x concentrations can approach 1-10 ppm. Even assuming a catalyst capable of achieving 100% approach to equilibrium, these NO_x concentrations integrated over a standard drive cycle can approach or even exceed regulated limits. Thus, NO_x decomposition for lean NO_x emissions control is not a viable strategy.

In contrast, under lean conditions and in the right temperature window, NO_x is efficiently reduced to N₂ by homogeneous reaction with NH₃. NH₂ radical, formed in situ from NH₃, exhibits a pronounced selectivity for reaction with NO_x in spite of the thermodynamic preference for reaction with O₂ to produce more NO_x. The origins of this selectivity can be understood by comparison of the potential energy surfaces for the NH₂ + NO and NH₂ + O₂ reactions (Figure 1). NH₂ radical forms a strongly bound adduct with NO, and further reaction to liberate N₂ and H₂O occurs with little barrier. In contrast, NH₂ radical weakly binds to O₂ and forward reaction to products cannot compete effectively with backwards decomposition.

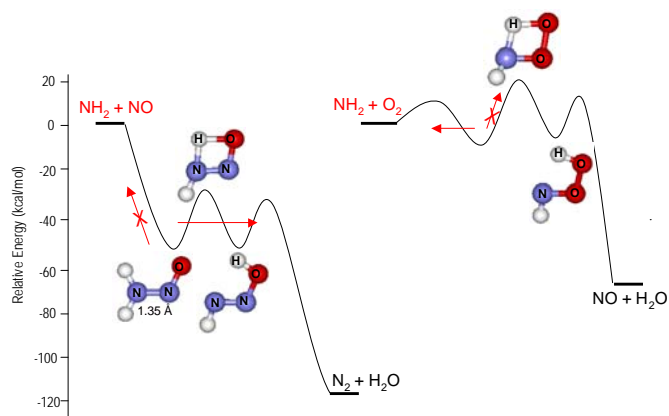


Figure 1. Comparison of BLYP-calculated potential energy surfaces for the NH₂ + NO (left) and NH₂ + O₂ (right) reactions.

The origins of these differences in bonding can be understood from comparison of the H₂NNO and H₂NOO molecular orbital diagrams. In fact, as shown in Table 1, NO and O₂ discriminate between many heteroatom radicals but exhibit similar bonding to H and C-centered radicals. The trends in reaction kinetics follow the bond energy trends.

Table 1. Comparison of radical-NO and radical-O2 bond strengths (kcal mol⁻¹)

	R-NO	R-O ₂	Δ
H	47	49	-2
CH ₃	40	33	7
<i>i</i> -C ₃ H ₇	37	37	0
CF ₃	43	37	6
HO	49	7	42
CH ₃ O	42	-4	46
F	57	13	44
Cl	38	6	33
NH ₂	48/54	0/15	~40-50

Conclusions

High selectivity towards reactions of reductant with NO_x over competing reactions with O₂ is key to catalytic lean NO_x removal. This selectivity is inherent in the homogeneous, thermal reduction of NO_x to N₂ with NH₃ reductant. Thermal deNO_x occurs at temperatures too great for many applications. Effectively catalysts need to enhance reactivity of reductants towards NO_x at lower temperatures without promoting the competing and undesirable reactions of reductant with O₂.

Acknowledgement. Several individuals, including Chris Goralski (Ford Motor), Donghai Sun (Arizona State), and Jim Adams (Arizona State) contributed many valuable ideas and results to this work.

References

- (1) Goralski, C. T. Jr.; and Schneider, W. F. *Appl. Catal. B: Environ.* **2002**, 37, 263.
- (2) Sun, D.; Adams, J. B.; Sengupta, D.; and Schneider, W. F. *J. Phys. Chem. A*, **2004**, 108, 9365.
- (3) <http://www.reactiondesign.com>.
- (4) te Velde, G.; Bickelhaupt, F. M.; Baerends, E. J.; Fonseca Guerra, C.; van Gisbergen, S. J. A.; Snijders, J.G.; and Ziegler, T. *J. Comput. Chem.* **2001**, 22, 931.

THEORETICAL INSIGHTS INTO ACID CATALYSIS OVER POLYOXOMETALATES

Matthew Neurock, Michael J. Janik, and Robert J. Davis

Departments of Chemical Engineering and Chemistry, University of Virginia, Charlottesville, VA 22904-4741

Introduction

Acid catalysis is at the heart of many hydrocarbon conversion processes including catalytic cracking, isomerization, oligomerization and alkylation. The first three of these processes are typically carried out over solid acids. Alkylation, however, is predominantly carried out using homogenous HF and H₂SO₄ which are highly corrosive and lead to waste disposal and catalyst separations issues. Despite the nearly 30 years of research, there are still no solid acid alternatives. Catalyst deactivation remains one of the foremost challenges in finding acceptable solid acid replacements. A more complete understanding of the fundamental structural and electronic catalyst features that control acidity, selectivity and the potential modes of deactivation could considerably advance our efforts toward the design of new materials. While there have been a great number of studies devoted to elucidating the mechanisms which control solid acid catalyzed conversion processes, our understanding is still fragmented and rather incomplete. Much of our understanding is based on assumed analogies with solution phase chemistry. Over the past decade, however, theoretical efforts have helped to establish fundamental concepts of solid acidity in zeolites and its influence on catalytic cracking. Herein we will review some of these general features and how they apply to alkylation over heteropolyacids. More specifically we examine potential mechanisms that control the isomerization of isobutane with *n*-butene and potential deactivation of HPAs by the loss of water.

The alkylation of isobutane and *n*-butene occurs via a complex reaction network that produces a broad distribution of products. The desired products for the alkylation of isobutane with *n*-butene are highly branched C₈ alkanes, mainly trimethylpentanes (TMPs). Competing reactions produce undesired side products which lead to catalyst deactivation. Intermolecular hydride transfer which is critical for alkylation is significantly inhibited over the deactivated catalysts. Understanding the mechanism for acid catalyzed hydride transfer has thus been proposed as “mandatory for the rational search

for improved solid catalysts” for this reaction.¹ Determination of the mechanism, including the transition state(s) for the hydride transfer step over acid catalysts will help to elucidate the requirements of the active site for hydride transfer. The relative rate of hydride transfer compared to the alkylation and isomerization steps must be considered in the rational design of effective catalytic materials.

Heteropolyacids (HPAs) are active for the alkylation of isobutane and *n*-butene but suffer from rapid catalyst deactivation.^{2,3} HPAs are proposed to be superacids,^{4,5} and their acid strength has raised hope that their deactivation during alkylation may be surmountable. Aside from acid strength, HPAs have additional advantages over zeolites. The titration of acid sites with ammonia shows that the acid sites of HPAs are of uniform strength.⁶ As hydride transfer is proposed to require a stronger acid site than the non-selective side reaction, uniformity may increase reaction selectivity. The diversity of compositions available provides for the tuning of HPA acid strength and the inclusion of redox bifunctionality. Furthermore, while the Brønsted acid sites of zeolites are restricted to an oxygen of the aluminum tetrahedron, protons are mobile over the entire exterior of the HPA structure. Researchers have speculated that multiple acid sites may be required to catalyze the hydride transfer step of alkylation.⁷ Mobility may allow for a closer proximity of acid sites in HPAs than in zeolites. Proton mobility may also allow protons to “undergo the collective influence of the environment”⁸ within the acid catalyst, thereby temporarily populating active locations which are not thermodynamically favored. Compared to zeolites, HPAs suffer from a lack of available surface area and less defined bulk structure. However, the use of HPAs on high surface area supports helps to overcome this issue in part.

Computational Methods

Quantum-chemical calculations were performed using gradient-corrected density functional theory as implemented in the Vienna ab initio Simulation Package (VASP) using plane-wave basis sets.⁹⁻¹¹ Ultrasoft pseudopotentials were used to describe electron-ion interactions.¹² Exchange and correlation energies were calculated using the Perdew-Wang (PW91) form of the generalized gradient approximation.¹³ This method has previously been shown to determine an equilibrium Keggin structure in agreement with experiment.¹⁴

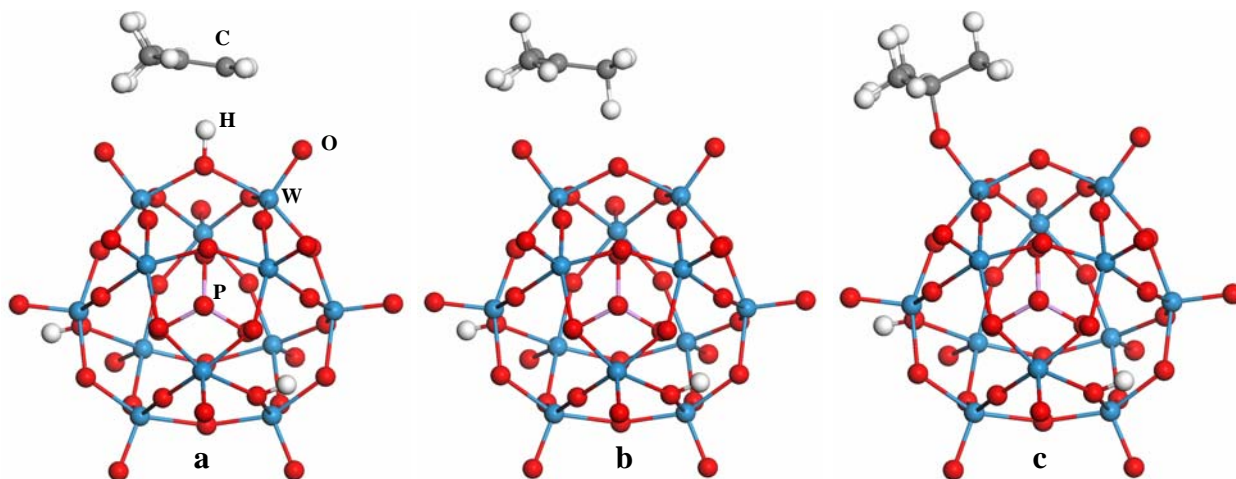


Figure 1. The steps to adsorption of isobutene on phosphotungstic acid. The three adsorbed states are: a) “physisorbed”, b) carbenium-ion intermediate, and c) “chemisorbed” alkoxy.

Results and Discussion

First principles density functional theory is used herein to calculate the proton affinity for different sites and different HPAs in order establish site distributions and their relative acid strengths. The proton affinity of phosphotungstic acid ($\text{H}_3\text{PW}_{12}\text{O}_{40}$, abbreviated HPW, Figure 1) was found to be 1080 kJ mol^{-1} , indicating that it is a substantially stronger acid than typical zeolites, which have proton affinities between $1200\text{--}1400 \text{ kJ mol}^{-1}$.¹⁵ The activation barrier for anhydrous proton-hopping is slightly lower over phosphotungstic acid than over HZSM-5,¹⁶ indicating the protons may move among oxygen atoms on the exterior of the Keggin unit structure in the reaction environment. The adsorption energies of basic probe molecules, such as ammonia and pyridine, also rank HPW as a strong acid. The calculated adsorption energy of ammonia to HPW, $130\text{--}150 \text{ kJ mol}^{-1}$, is similar, however, to that determined for adsorption to HZSM-5¹⁷ suggesting that these probes may not be quite so sensitive.

The relationship between measurements of acid strength and the energetics of hydrocarbon conversion processes over HPAs will be discussed. The energetics of the adsorption of alkenes to phosphotungstic acid is presented. Alkenes may adsorb initially through the donation of electron density from the carbon-carbon π -bond to the proton (Fig. 1a).

Transformation of this “physisorbed” state to the more strongly bound alkoxy state (Fig. 1c) occurs by the donation of the proton and formation of a covalent bond between the alkyl group and an oxygen atom of the catalyst. Both “physisorption” and “chemisorption” of propylene are more exothermic on HPW than on the zeolite chabazite¹⁸. The transition state for alkene adsorption is a carbenium ion (Fig. 1b), in which proton donation is virtually complete before the formation of the alkoxy bond. The activation barrier for this adsorption is lower over HPW than in zeolites. Higher substitution at the alkoxy carbon center leads to a lower activation barrier and stronger adsorption. A tertiary carbenium ion was identified as a stable intermediate during the adsorption of isobutene to HPW.

The reaction energetics of the individual steps in the alkylation over phosphotungstic acid ($\text{H}_3\text{PW}_{12}\text{O}_{40}$) were also determined using DFT methods. The relative rates of the coupling, isomerization, and hydride transfer steps are compared in order to predict deactivation rates due to the buildup of heavy hydrocarbons. The prospects of developing a solid acid catalyst for the alkylation of isobutane and *n*-butene will be discussed based on the reaction energetics determined for heteropolyacid catalysts. The calculations provide some insight into the requirements for an active solid acid.

References

- (1) Weitkamp, J.; Traa, Y. *Catal. Today* **1999**, *49*, 193.
- (2) Blasco, T.; Corma, A.; Martinez, A.; Martinez-Escolano, P. *J. Catal.* **1998**, *177*, 306.
- (3) Gayraud, P. Y.; Stewart, I. H.; Hamid, Derouane-Abd Hamid, S. B.; Essayem, N.; Derouane, E. G.; Viedrine, J. C. *Catal. Today* **2000**, *63*, 223.
- (4) Okuhara, T.; Nishimura, T.; Watanabe, H.; Misono, M. *J. Mol. Catal.* **1992**, *74*, 247.
- (5) Drago, R. S.; Dias, J. A.; Maier, T. O. *J. Am. Chem. Soc.* **1997**, *119*, 7702.
- (6) Bardin, B. B.; Bordawekar, S. V.; Neurock, M.; Davis, R. J. *J. Phys. Chem. B* **1998**, *102*, 10817.
- (7) Guisnet, M.; Gnep, N. S. *Appl. Catal. A* **1996**, *146*, 33.
- (8) Baba, T.; Ono, Y. *Appl. Catal. A* **1999**, *181*, 227.
- (9) Kresse, G.; Hafner, J. *Phys. Rev. B* **1993**, *47*, 558.
- (10) Kresse, G.; Furthmüller, J. *Comput. Mater. Sci.* **1996**, *6*, 15.
- (11) Kresse, G.; Furthmüller, J. *Phys. Rev. B* **1996**, *54*, 11169.
- (12) Vanderbilt, D. *Phys. Rev. B* **1990**, *41*, 7892.
- (13) Perdew, J. P.; Chevary, J. A.; Vosko, S. H.; Jackson, K. A.; Pederson, M. R.; Singh, D. J.; Fiolhais, C. *Phys. Rev. B* **1992**, *46*, 6671.

- (14) Janik, M. J.; Campbell, K. A.; Bardin, B. B.; Davis, R. J.; Neurock, M. *Appl. Catal. A* **2003**, *256*, 51.
- (15) Kramer, G. J.; van Santen, R. A. *J. Am. Chem. Soc.* **1993**, *115*, 2887.
- (16) Ryder, J. A.; Chakraborty, A. K.; Bell, A. T. *J. Phys. Chem. B* **2000**, *104*, 6998.
- (17) Kyrilidis, A.; Cook, S. J.; Chakraborty, A. K.; Bell, A. T.; Theodorou, D. N. *J. Phys. Chem.* **1995**, *99*, 1505.
- (18) Rozanska, X.; Demuth, T.; Hutschka, F.; Hafner, J.; van Santen, R. A. *J. Phys. Chem. B* **2002**, *106*, 3248.

MODELING THE FREE RADICAL CHEMISTRY OF MoS, MoCoS AND FeS CLUSTERS

James A. Franz[‡], Michel Dupuis[‡], Jerome C. Birnbaum[‡], Mikhail S. Alnajjar[‡], Thomas A. Bowden[‡] and Thomas E. Bitterwolf[†]

[‡]Pacific Northwest National Laboratory, P.O. Box 999, Richland, WA 99352

[†]Department of Chemistry, University of Idaho, Moscow, ID 83844

Introduction

Key understanding of structural transformations at hydrodesulfurization (HDS) catalyst sites can be gained with the help of electronic structure calculations. (1) In recent work (2) we presented results of a kinetic and theoretical study of the activation of the μ_2 -SH group in the complex $[\text{CpMo}(\mu\text{-S})(\mu\text{-SH})]_2$ that revealed a dramatic reduction of the S-H bond to 73 kcal/mol from 91 kcal/mol in H_2S . The function of Co and Ni in promoted MoS catalysts has been explored at near-atomic level for catalysts (3) and in a remarkable model study of Curtis and coworkers (4), who have identified reactions in which $\text{Cp}_2\text{Mo}_2\text{Co}_2\text{S}_3(\text{CO})_4$ clusters remove S atom from alkane and aromatic thiols, involving apparent reductions in C-S bond strengths from ca. 80 to as low as 20 kcal/mol. In this paper, we present results of electronic structure calculations for prototype systems containing the Mo_2S_4 , Fe_2S_2 , and CoMo_2S_4 clusters. DFT calculations reveal, that the S-H, (and by extension, C-S), bonds in $\text{Cp}_3\text{Mo}_2\text{CoS}_4\text{H}_2$ are dramatically reduced by the presence of the Co atom, demonstrating facile homolytic pathways for the cleavage of strong S-C bonds in HDS.

Electronic Structure Calculations

Density Functional theoretical electronic structure calculations were carried out using the NWChem 4.5 program. (5) Geometry optimizations were carried out using the UB3LYP method implemented with relativistic pseudo-potential (esp.) methods. Generally satisfactory geometries are achieved using the sbkjc vdz ecp basis set for metals and 6-31G(d) for CHNSO. For energy calculations, single point calculations using 6-311++G(2d,2p) basis set on CHNSO, were employed together with scaled harmonic frequencies for calculations of enthalpies at 298K. Bond dissociation enthalpies were calculated by means of isodesmic calculations, where the enthalpy change for eq. 1 is referenced to the bond dissociation enthalpy of H_2S , 91.2 kcal/mol and XS-H is the thiol of interest:



Results and Discussion

Electronic structure calculations reveal S-H bond strengths of 72 kcal/mol for $(\text{CO})_3\text{Fe}(\mu_2\text{-SH})_2\text{Fe}(\text{CO})_3$ (**1**) and 73 kcal/mol for $[\text{CpMo}(\mu\text{-S})(\mu\text{-SH})]_2$ (**2**). When a CpCo group is appended to the MoS cluster of **2**, the cobalt forms bonds with two sulfur atoms and a bonding interaction with one of the Mo atoms to form the structure **3**.

Removal of either S-H atom from **3** leads to two distinct radicals. Radical **4** results from the abstraction of the H atom of the SH adjacent to the Co center; the S-H group is predicted to exhibit a bond dissociation enthalpy of 35 kcal/mol (compared to 73 kcal/mol for **2**). Radical **5** results from the abstraction of the S-H hydrogen on the S bridge opposite from the appended Co atom. The S-H bond strength of **3** leading to **5** is found to be 54 kcal/mol. The results are summarized in Table 1. The structures of radicals **4** and **5** are depicted in Figure 1. Note that removal of the hydrogen atom from the $\text{Mo}(\mu_2\text{-SH})\text{Co}$ bridge leads to the formation of the symmetric

Mo_2S_4 cage with Co bridging two sulfur atoms. Spin density is largely localized on Co, suggesting that the sulfur-centered radical oxidizes the Co center. By contrast, abstraction of the S-H atom of **3** located at the $\text{Mo}(\mu_2\text{-SH})\text{Mo}$ bridge retains the structure of the central cluster, and the Co center exerts a smaller effect on the forming radical center. For the clusters **1** and **2**, abstraction of an S-H atom retains the core Fe_2S_2 and Mo_2S_4 geometries intact.

Table 1. Bond Dissociation Enthalpies of FeS, MoCoS, and MoS Cluster Models

Parent Thiol	Radical	BDE, kcal/mol
$[\text{CpMoS}(\text{SH})]_2$, 2	$[\text{CpMo}(\mu\text{-S})_2(\mu\text{-S}\bullet)(\mu\text{-SH})\text{MoCp}]$	73
$(\text{CO})_6\text{Fe}_2(\mu\text{-SH})_2$, 1	$(\text{CO})_6\text{Fe}_2(\mu\text{-SH})(\mu\text{-S}\bullet)$	72
$\text{Cp}_3\text{Mo}_2\text{CoS}_2(\mu\text{-SH})_2$, 3	4	35
$\text{Cp}_3\text{Mo}_2\text{CoS}_2(\mu\text{-SH})_2$, 3	5	54

Table 2. Rate Constants for Reactions of Benzyl Radical with Thiols (refs 2,6)

Parent Thiol	$k_{\text{abs}}/\text{M}^{-1}\text{s}^{-1}$ (benzene, 298 K)	BDE, kcal/mol
$\text{Cp}_3\text{Mo}_2\text{CoS}_2(\mu\text{-SH})_2$, 3 → 4	ND	35
$\text{Cp}_3\text{Mo}_2\text{CoS}_2(\mu\text{-SH})_2$, 3 → 5	ND	54
$(\text{CO})_6\text{Fe}_2(\mu\text{-SH})_2$, 1	1.2×10^7	72
$[\text{CpMoS}(\text{SH})]_2$, 2	2.6×10^6	73
Naphthalene-2-SH	1.3×10^5	77.9
<i>n</i> -C ₈ H ₁₇ SH	3×10^4	87.3
H ₂ S	2×10^4	91.2

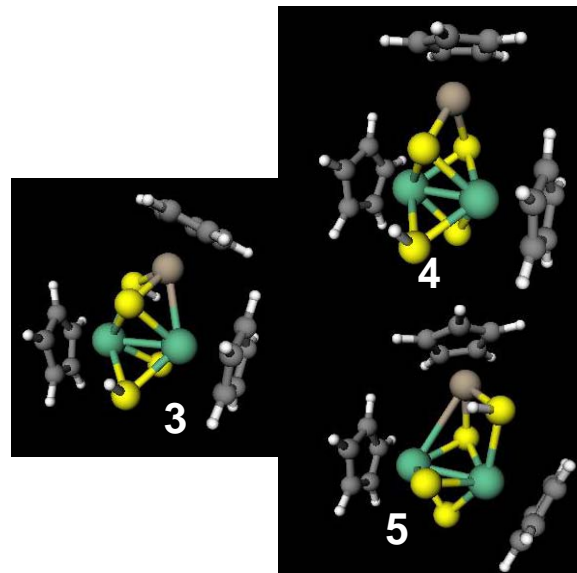
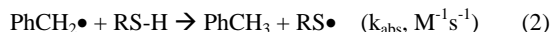


Figure 1. Abstraction of the $\text{Co}(\mu_2\text{-SH})\text{Mo}$ S-H group of cluster **3** leads to reorganization of the cluster and formation of the Co-centered radical **4** (BDE 35 kcal/mol). Abstraction of the $\text{Mo}(\mu_2\text{-SH})\text{Mo}$ S-H group to form **5** (BDE 54 kcal/mol) retains approximately the starting cluster geometry.

The reactivity of Mo₂S₄ (**2**) and FeS₂ (**1**) clusters with a carbon-centered radical, benzyl radical (eq. 2), illustrates the effect of reduced S-H bond strengths for a selection of organic thiols, and **1** and **2**. While no experimental data exist for **3**, the other clusters shown in Table 2 suggest that cluster **3**, analogous to the systems of Curtis and coworkers(4), will react with organic carbon-centered free radicals at diffusion controlled rates, and that the Mo₂CoS clusters will dissociate hydrogen atom at temperatures < 400K. Thus, the Mo₂CoS clusters provide active sources of hydrogen atom to participate in reduction reactions.



Conclusions

These calculations illustrate greatly reduced bond strengths of the S-H group (and by extension, C-S bond strengths) in the CoMo₂S₄ cluster for the models described here. An important role of the mixed metal clusters in induced cleavage of strong sulfur-carbon bonds is suggested by these results. The chemistry of the C-S bond cleavage step is better understood as a consequence of the participation of the redox metal, Co. Mechanistic steps leading to creation of coordinatively unsaturated sites at Mo and Co remain to be explored. In order to further develop theoretical approaches to HDS reactive intermediates, supporting thermochemical data is needed for model systems in order to calibrate the predictions of electronic structure calculations. No experimental S-H bond strengths have been measured for models of relevance to HDS catalysis. Finally, it is clear that model chemistry in partnership with theory and empirical catalysis studies will be necessary to establish an improved understanding on the molecular level of HDS.(7)

Acknowledgement. This work was supported by the Office of Basic Energy Sciences, Chemical Sciences, Geosciences, and Biosciences Division, U.S. Department of Energy under contract DE-ACO6-76RLO 1830.

References

- (1) Byskov, L.S.; Nørskov, J.K.; Clausen, B. S.; and Topsøe, H. J. Catalysis **1999**, *187*, 109.
- (2) Franz, J. A.; Birnbaum, J. C.; Kolwaite, D. S.; Linehan, J. C.; Camaioni, Donald M.; and Dupuis, Michel, *J. Am. Chem. Soc.* **2004**, *126*, 6680-6691.
- (3) Lauritsen, J.V.; Helveg, S.; Lægsgaard, E.; Stensgaard, I.; Clausen, B.S.; Topsøe, H.; and Besenbacher, F. *J. Catalysis* **2001**, *197*, 1.
- (4) Curtis, M.D. "Hydrodesulfurization Catalysts and Catalyst Models Based on Mo-Co-S Clusters and Exfoliated MoS₂" p 154, in Stiefel, E.I.; and Matsumoto, K., Eds., "Transition Metal Sulfur Chemistry, Biological and Industrial Significance", ACS Symposium Ser. 653, American Chemical Society, Washington, D.C. 1996.
- (5) T. P. Straatsma, E. Apra, T. L. Windus, M. Dupuis, E. J. Bylaska, W. de Jong, S. Hirata, D. M. A. Smith, M. T. Hackler, L. Pollack, R. J. Harrison, J. Nieplocha, V. Tipparaju, M. Krishnan, E. Brown, G. Cisneros, G. I. Fann, H. Fruchtl, J. Garza, K. Hirao, R. Kendall, J. A. Nichols, K. Tsemekhman, M. Valiev, K. Wolinski, J. Anchell, D. Bernholdt, P. Borowski, T. Clark, D. Clerc, H. Dachsel, M. Deegan, K. Dyll, D. Elwood, E. Glendening, M. Gutowski, A. Hess, J. Jaffe, B. Johnson, J. Ju, R. Kobayashi, R. Kutteh, Z. Lin, R. Littlefield, X. Long, B. Meng, T. Nakajima, S. Niu, M. Rosing, G. Sandrone, M. Stave, H. Taylor, G. Thomas, J. van Lenthe, A. Wong, and Z. Zhang, "NWChem, A Computational Chemistry Package for Parallel Computers, Version 4.5" (2003), Pacific Northwest National Laboratory, Richland, Washington 99352-0999, USA
- (6) J.A. Franz, Thomas A. Bowden, Thomas E. Bitterwolf, Jerome C. Birnbaum, unpublished work (H₂S and thiol **1** of Table 2). For experimental methodology for determination of abstraction rate constants for thiols and carbon-centered free radicals, see ref. 2.
- (7) Bej, S.K.; Maity, S. K.; and Turaga, U.T. *Energy & Fuels* **2004**, *18*, 1227

DENSITY FUNCTIONAL THEORY STUDY OF THE HYDROGENATION OF CARBON MONOXIDE ON FE(100) SURFACE

D. C. Sorescu

U. S. Department of Energy, National Energy Technology Laboratory, P. O. Box 10940, Pittsburgh, PA 15236.

Introduction

Understanding the interactions of carbon monoxide and hydrogen with iron surfaces is of primary importance as these systems can be involved in many catalytic processes such as methanation or Fischer-Tropsch (FT) synthesis of aliphatic hydrocarbons.^{1,2} In the particular case of FT synthesis there are several important issues that continue to receive scientific attention. Among these, achieving a chemical understanding of FT processes by identification of primary and secondary reaction steps as function of external reaction conditions is still lacking.³ In the case of iron catalysts the complexity of the mechanism is further increased due to the fact that composition and structure of the catalyst change following the initial decomposition of CO molecules. Various types of iron carbides or iron oxides in addition to metallic iron have been identified as being formed during FT synthesis process.^{4,5} Specifically, at least three types of carbon species have been proposed to exist, namely a mobile or reactive specie, an immobile species and a stable surface carbide.⁶

Several previous experimental studies attempted to provide an atomistic description of the adsorption and dissociation processes of CO and H₂ species on iron surface. Particularly, in the case of Fe(100) surface work done in Bernasek group^{7,8} indicated that below 440 K CO adsorption takes place molecularly with sequential filling of three states corresponding to three types of binding configurations of CO molecule. The most tightly bound molecular state, denoted CO(α_3), is the precursor to dissociation of CO at 440 K, and corresponds to CO adsorbed at 4-fold hollow site in a tilted configuration.⁶

Similarly, H₂ adsorption of Fe(100) surface has been analyzed in several papers from Madix group.⁹⁻¹¹ It was concluded that H₂ adsorption takes place dissociatively and that desorption spectrum presents two states, tentatively assigned as β_1 and β_2 , with the desorption temperature of β_1 state being lower than the one of the β_2 state. Based on temperature program desorption (TPD) and HREELS experiments it was determined that at low coverage, H adsorbs to a high ligancy state (β_2 state) namely the four-fold (4F) hollow site. This state converts with the increase in coverage to a state of smaller ligancy (β_1 state), tentatively assigned as a pseudo three-fold site, asymmetric within the 4F hollow site.¹¹ The interaction between CO and hydrogen has also been studied on Fe(100) surface.¹² Preadsorption of hydrogen was observed to reduce the binding energy of CO and to inhibit the dissociation of CO molecules. Despite this initial progress further detailed studies of the hydrogenation processes of C and CH_x species on Fe(100) surface are still not available.

In an attempt to clarify some of the initial elementary processes that might be involved in the FT process on iron surfaces (Fe(100)), in this work we focus on theoretical analysis of the elementary processes that take place in the initiation stage. In particular we considered both the dissociative adsorption of H₂ with formation of metal hydrides and CO adsorption and dissociation with formation of metal carbide. The resulted surface carbide is then further hydrogenated in a stepwise mechanism leading to formation of methylidyne, methylene, methyl and eventual to gaseous methane.

These computational steps will be further extended to include the coupling reactions of C₂(ad) surface species.

Computational Method

The calculations performed in this study were done using the Vienna *ab initio* simulation package (VASP).¹³⁻¹⁵ This program evaluates the total energy of periodically repeating geometries based on density-functional theory and the pseudopotential approximation. In this case the electron-ion interaction is described by fully non-local optimized ultrasoft pseudopotentials similar to those introduced by Vanderbilt.^{16,17} A plane-wave basis set has been used with a cutoff energy of 495 eV.

Calculations have been done using the spin polarized PW91 generalized gradient approximation (GGA) of Perdew *et al.*¹⁸ The sampling of the Brillouin zone was performed using a Monkhorst-Pack scheme.¹⁹

The minimum energy paths between different minima were optimized by use of the nudged elastic band (NEB) method of Jónsson and Mills.²⁰ In this approach the reaction path is "discretized", with the discrete configurations, or images, between minima being connected by elastic springs to prevent the images from sliding to the minima in the optimization.

The periodic nature of the surface was considered in the present simulations by the aid of a supercell model with periodic boundary conditions in all three directions. The majority of calculations have been done using a slab model consisting of six layers with the top two layers being allowed to relax. Additional tests have been performed for the case of supercells with seven layers and double side adsorption. In all calculations a vacuum layer of at least 10 Å has been used.

Results and Discussion

CO Adsorption and Dissociation. We have shown in our previous study²¹ that CO adsorption on top (1F), in a bridge (2F) and at a four-fold (4F) hollow sites can be identified on Fe(100) surface. Among these the most stable is adsorption at 4F site with an adsorption energy in the range 46.7 and 43.8 kcal/mol depending on the exchange-correlation functional (PW91 or RPBE) used. In this state CO molecule is tilted relative to the surface normal by 50° and the CO bond is elongated to 1.32 Å. The corresponding vibrational stretching frequency was calculated to be 1246 cm⁻¹, significantly smaller than the gas phase value of 2143 cm⁻¹. Among various local minima (i.e. 1F, 2F and 4F sites) the highest diffusion barrier of CO molecule was found to correspond to diffusion out of 4F site with a barrier of about 13 kcal/mol. The barrier for dissociation of CO bound at the 4F site has been found to have a value of 24.5 kcal/mol. The resulted C and O atoms adsorb at 4F sites with binding energies of 186 and 145 kcal/mol, respectively.

H Adsorption on Fe(100) Surface. In this work we present our results related to adsorption of H₂ on Fe(100) surface. We found that this takes place dissociatively with an activation energy of about 3.5 kcal/mol. This result agrees with previous experimental findings⁹⁻¹¹ which indicate that dissociative chemisorption of H₂ can readily take place. For the atomic H we have determined that in the case of low coverages adsorption at both 4F and 2F sites have similar binding energies of 8.0 and 7.5 kcal/mol, respectively, with respect to gas phase H₂. In the full coverage regime there is a clear distinction between 2F (E_{ads}=5.0 kcal/mol) and 4F (E_{ads}=8.9 kcal/mol) adsorption sites with a net preference for adsorption at 4F site. Moreover, we have analyzed the sequence of sites filling as function of coverage and have determined that upon filling all 4F sites occupation of 2F followed by 1F sites is possible while adsorption at nearby 2F and 1F sites leads to H-H recombination.

CH_x (x=1,4) Adsorption. The adsorption configurations of methidyne and methylene at 1F, 2F and 4F sites are indicated in Fig. 1 together with the corresponding adsorption energies. In both these two cases the adsorption at 4F site is found to be the most stable with binding energies of 161.3 and 99.5 kcal/mol for CH and CH₂ species, respectively.

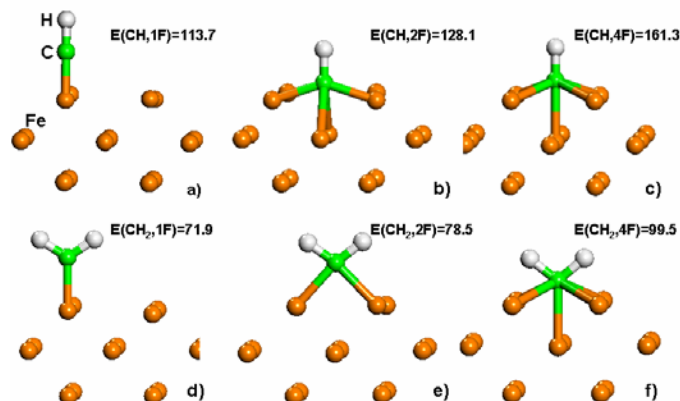


Figure 1. Adsorption configurations of CH and CH₂ species on Fe(100) surface. The corresponding binding energies in kcal/mol are also indicated.

In contradistinction, methyl adsorption (see Figures 2a and 2b) is found to be most stable at 2F site. Finally, in the case of methane adsorption we found a very weak interaction with Fe surface independent of the surface site and molecular orientation relative to the surface. In this case the calculated adsorption energies are very small with values of about 0.9 kcal/mol indicating a weakly physisorbed state.

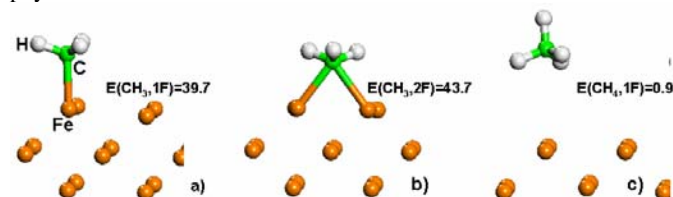


Figure 2. Adsorption configurations of CH₃ and CH₄ species on Fe(100) surface. The corresponding binding energies in kcal/mol are also indicated.

CH_x Hydrogenation Reactions. Beside characterization of the relative stabilities of various CH_x species we have analyzed based on nudged elastic band calculations the corresponding activation energies for CH_x hydrogenation reactions. The final results are summarized in Figure 3. From this figure it can be seen that the most stable species on the surface correspond to chemisorbed atomic species followed by CH species. The rate determining step of the entire process corresponds to CO dissociation.

Conclusions

The main results of our investigations can be summarized as follows:

- The 4F hollow site is the preferential adsorption site for CO, C, H, CH and CH₂ species followed by bridge (2F) site. The on-top adsorption site is the most unfavorable site.
- CH₃ species can adsorb at both 1F and 2F sites with an increased preference for the bridge site.

- For CO dissociation and CH_x (x=1,4) hydrogenation processes the rate limiting step is represented by CO dissociation step with an activation energy of about 24.5 kcal/mol.
- Adsorbed CH species are the most stable from the CH_x series.

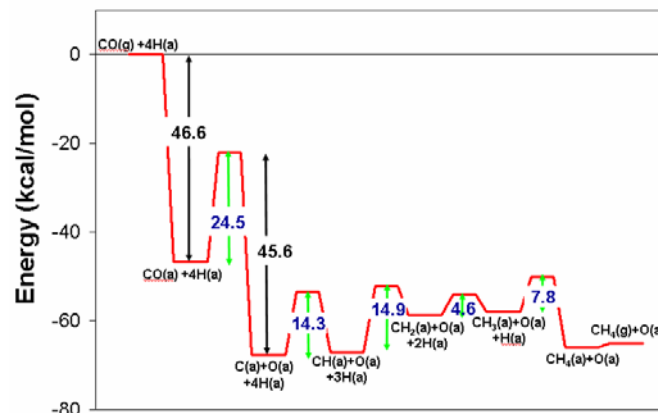


Figure 3. Energy diagram for CO dissociation and hydrogenation to CH₄ on Fe(100) surface.

Acknowledgement. We gratefully acknowledge the computational resources provided under a Challenge award received from the DOD High Performance Computing Modernization Office, and by Pittsburgh Supercomputer Center.

References

- Somorjai, G. A. In *Introduction to Surface Chemistry and Catalysis*; Wiley, New York, 1994.
- (a) Anderson, R. B. In *The Fischer-Tropsch Synthesis*; Academic, Orlando FL, 1984. (b) *Handbook of Heterogeneous Catalysis*; Ertl, G.; Knözinger H.; Weltkamp, J. Eds.; Weinheim, VCH, 1997.
- (a) Maitlis, P. M. *J. Organom. Chem.* 2004, in press. (b) Maitlis, P. M.; Quyoum, R.; Long, H. C.; Turner, M. L. *Appl. Catal. A* 1999, 186, 363.
- (a) Ridel, T.; Schulz, H.; Schaub, G.; Jun, K.W.; Hwang, J.; Lee, K. W. *Topics in Catal.* 2003, 26, 41. (b) Schulz, H.; Schaub, G.; Claeys, M. Riedel, T. *Appl. Catal. A* 1999, 186, 215.
- Roffer-DePoorter C. K. *Chem. Rev.* 1981, 81, 447.
- Lázár, K.; Schay, Z.; Gucci, L. J. *Molec. Catal.* 1982, 17, 205.
- (a) Moon, D. W.; Dwyer, D. J.; and Bernasek, S. L. *Surf. Sci.* 1985, 163, 215. (b) Moon, D.W.; Bernasek, S. L.; Lu, J.P.; Gland, J. L.; and Dwyer, D. L. *Surf. Sci.* 1987, 184, 90.
- Moon, D. W.; Cameron, S.; Zaera, F.; Eberhardt, W.; Carr, R.; Bernasek, S.L.; Gland, J. L.; Dwyer, D. J. *Surf. Sci.* 1987, 180, L123.
- Benziger, J.; Madix, R. J. *Surf. Sci.* 1980, 94, 119.
- Burke, M. L.; Madix, R. J. *Surf. Sci.* 1990, 237, 20.
- Merrill, P. B.; Madix, R. J. *Surf. Sci.* 1996, 347, 249.
- Benzinger, J.B.; Madix, R. J. *Surf. Sci.* 1982, 115, 279.
- Kresse, G.; Hafner, J. *Phys. Rev. B* 1993, 48, 13115.
- Kresse, G.; Furthmüller, J. *Comput. Mat. Sci.* 1996, 6, 15.
- Kresse, G.; Furthmüller, J. *Phys. Rev. B* 1996, 54, 11169.
- Vanderbilt, D. *Phys. Rev. B* 1990, 41, 7892.
- Kresse, G.; Hafner, J. *J. Phys. Condens. Matter* 1994, 6, 8245.
- Perdew, J. P.; Chevary, J. A.; Vosko, S. H.; Jackson, K. A.; Pedersen, M. R.; Singh, D. J. and Frolhais, C. *Phys. Rev. B* 1992, 46, 6671.
- Monkhorst, H. J.; Pack, J. D. *Phys. Rev. B* 1976, 13, 5188.
- Mills, G.; Jónsson, H.; Schenter, G. K. *Surf. Sci.* 1995, 324, 305.
- Sorescu, D. C.; Thompson, D. L.; Hurley, M. M.; Chabalowski, C. F. *Phys. Rev. B* 2002, 66, 035416.

EARLY FISCHER-TROPSCH STEPS ON Fe(110) AND Co(0001) SURFACES: COMPARATIVE DFT STUDIES

Amit A. Gokhale and Manos Mavrikakis

Department of Chemical and Biological Engineering
University of Wisconsin – Madison
Madison, WI 53706

Introduction

Fischer-Tropsch Synthesis (FTS), the production of liquid hydrocarbons from synthesis gas (CO and H₂), is a technically-proven, economically-promising technology of world-wide commercial interest for environmentally-sound production of high-quality chemicals and liquid fuels from coal, biomass, and natural gas^{1,2}. Given the large coal and natural gas reserves, and the simultaneously dwindling petroleum reserves, combined with a growing need for inexpensive, clean transportation fuels, FTS is projected to play an ever increasing role in the near future.

A number of studies, both experimental³⁻⁶ as well as theoretical^{7,8} have been conducted to understand the mechanism of this reaction^{9,10} on a variety of catalysts. In particular, Fe, Co and Ru have been identified as promising catalysts. Methane formation during FTS is undesirable as it reduces the yield of higher hydrocarbons. Accordingly, efforts have been made to reduce methane selectivity and it has been shown that promoted Fe catalysts perform better than Co in this respect⁶. Nevertheless, to understand the mechanism of the FTS reaction, it is extremely important to study methane formation in detail as this would provide insights into the mechanism of Carbon hydrogenation. More importantly, a comparative study between Fe and Co would point out the similarities and the differences in the methanation reaction mechanism on these catalysts and also help in understanding the specific role of possible promoters.

In this study, we perform a periodic, self-consistent, spin-polarized DFT investigation of methane formation from CO and H₂ on Fe(110) and Co(0001) surfaces. We examine the binding of various reaction intermediates and determine the energetics of the elementary steps such as CO dissociation, and H addition to C and its partially hydrogenated fragments. Based on these energetics we construct the thermodynamic potential energy surfaces (PESs) for methane formation on Fe(110) and Co(0001), and use these PESs to develop FTS related insights.

Methods

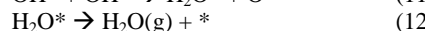
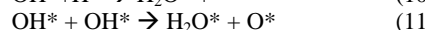
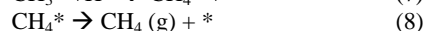
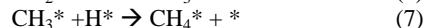
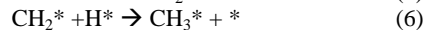
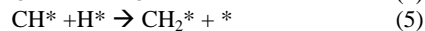
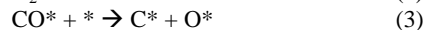
All calculations are performed using DACAPO¹¹. Adsorption is allowed on only one of the two surfaces of the slab and the electrostatic potential is adjusted accordingly. Calculations for both Fe and Co were spin-polarized. The surface is modeled by a (2×2) unit cell, which corresponds to ¼ ML coverage for the adsorbates. (110) and (0001) surfaces are used to model Fe and Co respectively. Since the Fe(110) surface is more open compared to the Co(0001) surface, surface relaxation has a significant effect on the adsorption characteristics of various species; hence Fe is modeled using a four layered slab with the top two layers relaxed. On the other hand for modeling the Co surface a 3 layer static slab is found to be sufficient.

Kohn-Sham one-electron valence states are expanded in a basis of plane waves with kinetic energies below 25 Ry. The exchange-correlation energy and potential are described by the generalized gradient approximation (GGA-PW91), and ionic cores are described by ultrasoft pseudopotentials. The surface Brillouin zone is sampled with a 4x4x1 *k* point set for Fe, and with 18 Chadi-Cohen special *k* points for Co. The calculated equilibrium PW91 lattice constant for bulk Fe is *a* = 2.85 Å, in good agreement with the experimental value

of 2.87 Å. Similarly for Co we calculate a lattice constant of 2.50 Å in good agreement with the experimental value of 2.51 Å.

Results and Discussion

The mechanism for CO hydrogenation to CH₄ can be represented as follows:



where * represents a vacant site and X* represents X adsorbed on the surface. Although alternative mechanisms involving direct hydrogenation of CO prior to its dissociation have been suggested, the mechanism outlined above is the most accepted mechanism and we have used that for making comparisons between methane formation steps on Fe and Co surfaces.

Structure and Binding of Adsorbates on Fe(110) and Co(0001). A summary of the binding energies and the preferred adsorption sites for atomic, molecular and radical adsorbates involved in methane formation is provided in Table 1. Fig. 1 depicts the top view of the Fe(110) and Co(0001) surfaces showing the different high symmetry sites at which adsorption of various species has been investigated.

Table 1. Preferred Adsorption Sites and the PW91 Binding Energies for the Intermediates involved in CH₄ Formation on Fe(110) and Co(0001). Reference Zero for Energy corresponds to gas-phase species at infinite separation from the corresponding slabs.

Species	Fe(110)		Co(0001)	
	Preferred Site	B.E. (eV)	Preferred Site	B.E. (eV)
H	three-fold	-2.99	fcc/hcp	-2.79
C	long-bridge	-7.56	hcp	-6.56
O	three-fold	-6.05	fcc/hcp	-5.35
CO	top	-1.96	fcc/hcp	-1.87
CH	long-bridge	-6.84	hcp	-6.17
CH ₂	three-fold	-4.28	fcc	-3.89
CH ₃	three-fold	-2.06	fcc/hcp	-1.87
CH ₄	fcc/hcp/top	-0.03	fcc/hcp/top	-0.04

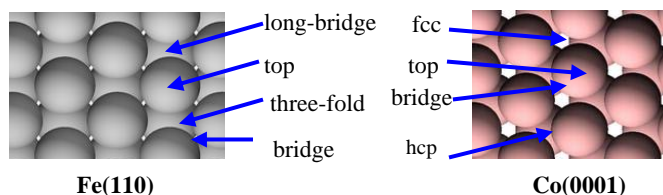


Figure 1. Top views of Fe(110) and Co(0001) surfaces showing the four high symmetry sites on each surface.

It is interesting to note that as C gets successively hydrogenated, the binding energy of the resulting species decreases significantly and CH₄ interacts only very weakly with both surfaces (see Table 1). Furthermore, all adsorbates listed in Table 1, except for CH₄, bind considerably stronger on Fe(110) than on Co(0001). One of the

reasons for this is that the Fe(110) surface is relatively more open compared to the close-packed Co(0001) surface. However our investigations on the relatively open stepped surface of Co show that even on that surface, all the species bind weaker than on Fe(110). For example on the stepped Co surface, the binding energies of H (-2.86 eV), C (-7.29 eV), and O (-5.43 eV) are considerably lower than their corresponding binding energies on the Fe(110) surface (Table 1). This suggests that the stronger binding of most species on Fe(110) is predominantly an electronic effect.

Thermochemistry of CH₄ formation on Fe(110) and Co(0001) surfaces. The knowledge of the binding energies of various species on the Fe(110) and the Co(0001) surfaces allows us to construct a *thermodynamic* PES for CH₄ formation on both surfaces (Fig. 2). These PESs give us an insight into the relative thermodynamic favorability of the various steps and also allows us to make meaningful comparisons between Fe and Co surfaces in order to understand the reactivity of these surfaces for methane formation.

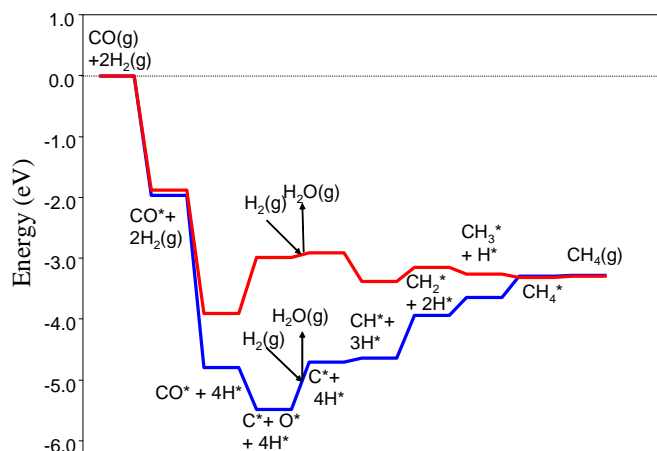


Figure 2. Thermodynamic Potential Energy Surface (PES) for CO hydrogenation to CH₄ on Fe(110) surface (blue) and Co(0001) surface (red). Energy zero corresponds to gas phase CO and 2H₂ and the corresponding slab at infinite separation.

One of the most important differences between methane formation on Fe and Co surfaces is the relative thermochemistry of CO dissociation on these surfaces: CO dissociation of Fe(110) is exothermic ($\Delta E = -0.68$ eV) whereas it is endothermic ($\Delta E = 0.92$ eV) on Co(0001), always with respect to the adsorbed CO state. Previous DFT studies have shown that simple linear correlations exist between the transition state and final state energy of simple reactions, such as CO dissociation¹². Hence the kinetics for CO dissociation are likely to be significantly more favorable on the Fe(110) surface than on the Co(0001) surface. Detailed kinetic calculations performed by us for this step show that the CO dissociation barrier on the Fe(110) surface is only 1.52 eV, whereas on the Co(0001) this barrier is 2.73 eV. A comparison of these activation barriers with the energy of CO desorption (see Table 1) suggests that CO dissociation is preferred over desorption on Fe(110), whereas CO desorption is likely to be favored against dissociation on Co(0001).

Removal of O through water formation seems to be thermodynamically easier on Co(0001) than on Fe(110). This suggests that significant coverages of O may not be expected on the Co surface under typical reaction conditions. Fe, on the other hand, may retain surface O and this could account for the formation of the Fe-oxide phase which has been suggested to play an active role in

catalyzing the water gas shift reaction on Fe catalysts under typical FTS conditions.

Hydrogenation of C to CH is almost thermoneutral on Fe(110) ($\Delta E = 0.06$ eV), whereas the same step is exothermic ($\Delta E = -0.47$ eV) on Co(0001). This suggests that the CH formation thermodynamics are considerably better on the Co surface than on the Fe surface. The subsequent hydrogenation steps to CH₂, CH₃ and CH₄ are also more favorable on the Co surface compared to the Fe surface. With no exception, all these steps are endothermic on Fe(110), whereas on the Co surface CH₂ formation is moderately endothermic ($\Delta E = 0.23$ eV) while CH₃ and CH₄ formation are mildly exothermic. The relatively flat PES of Co for C hydrogenation steps suggests that these steps are likely to be more facile on Co(0001) than on Fe(100).

The PESs for CH₄ formation shown in Fig. 2 indicate that on Fe(100), C, H and CH are likely to be the dominant surface species, whereas on Co(0001) other intermediates, such as CO, CH₂ and CH₃ are also likely to have significant coverages. Fig. 2 also shows that CH₂ is relatively more stable on the Co surface than on the Fe surface. This suggests that CH₂ may play a more important role in the C – C coupling on Co compared to Fe; whereas on the unpromoted Fe surface, one might expect that CH and C may play an active role in C – C bond formation. Detailed minimum energy path calculations are currently under way. We anticipate that additional information derived from these studies regarding the kinetics of these elementary steps will provide a more comprehensive picture of the unselective route to CH₄ formation on these two commonly used FTS catalysts.

Acknowledgements. We acknowledge partial financial support from a grant (DE-FC26-03NT41966) provided by the U.S. DOE-NETL, and fruitful discussions with Drs Cugini, Krastman, and Soreescu. Part of this work used resources at NERSC, which is supported by the Office of Science of the U.S. DOE under Contract No. DE-AC03-76SF00098. The remaining fraction of this work was pursued by using the MSCF at the William R. Wiley EMSL, which is a National Scientific user facility sponsored by the U.S. DOE Office of Biological and Environmental Research and located at the PNNL.

References

- (1) Chorkendorff, I.; Niemantsverdriet, H. *Concepts of Modern Catalysis and Kinetics*; Wiley-VCH: Weinheim, 2003.
- (2) Somorjai, G. A. *Introduction to Surface Chemistry and Catalysis*; John Wiley: New York, 1994.
- (3) Zennaro, R.; Tagliabue, M.; Bartholomew, C. H. *Catal. Today* **2000**, 58, 309.
- (4) Iglesia, E. *Appl. Catal. A : General* **1997**, 161, 59.
- (5) Xu, J.; Bartholomew, C. H.; Sudweeks, J.; Eggett, D. L. *Top. Catal.* **2003**, 26, 55.
- (6) Li, S.; Krishnamoorthy, S.; Li, A.; Meitzner, G. D.; Iglesia, E. *J. Catal.* **2002**, 206, 202.
- (7) Klink, D. J., II; Broadbelt, L. J. *Surf. Sci.* **1999**, 429, 169.
- (8) Ciobica, I. M.; Kramer, G. J.; Ge, Q.; Neurock, M.; van Santen, R. A. *J. Catal.* **2002**, 212, 136.
- (9) Anderson, R. B. *The Fischer-Tropsch Synthesis*; Academic Press: New York, 1984.
- (10) Bell, A. T. *Catal. Rev. Sci. Eng.* **1981**, 23, 203.
- (11) Hammer, B.; Hansen, L. B.; Nørskov, J. K. *Phys. Rev. B* **1999**, 59, 7413.
- (12) Nørskov, J. K.; Bligaard, T.; Logadottir, A.; Bahn, S.; Hansen, L. B.; Bollinger, M.; Bengaard, H.; Hammer, B.; Sljivancanin, Z.; Mavrikakis, M.; Xu, Y.; Dahl, S.; Jacobsen, C. J. H. *J. Catal.* **2002**, 209, 275.

MECHANISTIC STUDY OF CELLULOSE PYROLYSIS IN THE PRESENCE OF INORGANICS USING ELECTRONIC STRUCTURE METHODS

(1) Bappaditya Chatterjee, (2) Budda Reddy, (3) P. Jena, (4) S. N. Khanna and (5) B. K. Rao

(1) & (2) 4201 Commerce Road, Philip Morris USA, Richmond, VA 23234, (3), (4) & (5) Department of Physics, Virginia Commonwealth University, Richmond, VA 23284.

I. Introduction

An understanding of the role of metal atoms in carbohydrates and their polymers for biochemical processes is evolving [1]. However, the importance of their interaction and complexation for other fundamental bioinorganic degradation processes such as cellulose pyrolysis is poorly understood. A degradation process involving the study of pyrolysis of biomass material like cellulose is of prime importance for application towards the retardation of forest fuels as well as in other branches of forestry [2]. In addition, it serves as a good model system for studying tobacco chemistry in cigarettes [3].

So far there has been only one published work involving cellulose pyrolysis in the presence of transition-metal salts [4]. Despite its growing importance, neither the atomistic details of the chemistry involved in such interactions, nor the microscopic mechanisms involved are fully understood. To date, there have been no theoretical studies in this regard.

In this present work, electronic structure calculations based on hybrid density functional theory have been carried out for the first time to investigate the interaction of atomic Pd, Pd(II) and Cu(II) chloride with a cellobiose molecule which is used to model pyrolysis of cellulose.

II. Computational Details

All the calculations presented in this paper were done using Gaussian 98 using density functional theory with the B3LYP method. The main group elements were treated with a triple-zeta polarization basis, while the core-electrons of transition-metal atoms were treated using the semi-relativistic Hay-Wadt pseudopotential and associate basis sets were used to treat the valence electrons. To simulate harsh reaction conditions, as in pyrolysis, where a huge amount of energy is available to the reacting system, we have often placed reactants in extreme close proximity to each other, thus ensuring that the energy barriers are crossed. The nature of any proposed reaction-intermediate as opposed to transition-state species, used in order to elucidate any reaction mechanism, was verified by subsequent harmonic frequency calculations, which also yielded zero-point energies.

III. Results and Discussion

(1) Cellobiose In our studies of modeling the interaction of cellulose in the presence of added inorganics, we consider a single cellobiose unit. Cellobiose (Figure 1) is the smallest repeating unit of cellulose comprising of two D-glucose units linked by an oxygen atom. The intramolecular hydrogen-bonds are shown as dotted lines in Figure 1. It is to be noted that Nishiyama *et. al* [5], have obtained the values for hydrogen bonds in bulk cellulose crystals (shown in parenthesis). Our values are in very good agreement with the above and the deviations from the experimental numbers range from 1-7%. Hence, our model of cellobiose is essentially a realistic representation of the local stereochemistry of cellulose in the bulk crystal/polymeric chain. For further discussion we will follow the numbering of the atoms given in Figure 1.

(2) Interaction of Atomic Pd with Cellobiose Our attempt here is to understand if Pd in its neutral monoatomic state ($^1S_0, 4d^{10}$) interacts with a cellobiose unit. The preferential positions of the Pd atom have been investigated by allowing Pd to approach the cellobiose molecule from different directions. Pd is observed to insert into the bond between O1' and C1'. This product has a binding energy of $4.6 \text{ kcal mol}^{-1}$. This product can be viewed as modeling the binding of Pd to a terminal unit of cellulose.

As above, we also observe Pd inserts into the C1-O bond. This product is thermodynamically much more stable than the previous inserted product, with a binding energy of $11.5 \text{ kcal mol}^{-1}$.

(3) Interaction of Palladium (II) Chloride and Cellobiose The favorable direction of approach of PdCl_2 is that of it being parallel to the direction of 1-4 linkage with O axis of cellulose. This reacting system undergoes fragmentation reaction forming two fragments (F1) and (F2) (see Figure 2). The fragment F1 containing the PdCl undergoes interesting intramolecular reactions to form a levoglucosan product-complex as shown in Figure 3. Considering the structures of the reactive intermediates outlined in Figure 3, one finds that Pd has an affinity for carbon and thus acts as an 'anchoring' agent to hold the otherwise unstable fragment such that the intramolecular reactions can occur effectively, ending up in the final levoglucosan-Pd(H)Cl product-complex.

(4) Interaction of Copper (II) Chloride and Cellobiose As, opposed to its Pd counterpart, CuCl_2 interacts in a completely different way with cellobiose. The fragments are shown in Figure 4. It is observed that Cu has no affinity for carbon or insertion to a C-C bond. Hence in this case the 'anchoring' effect is not observed, resulting in the levoglucosan formation being less feasible than formation of open chain organics such as glyoxylic acid. The two possible products and their relative energies are shown in Figure 5. Lesser amounts of levoglucosan formation is indeed observed in pyrolytic processes involving Cu salts and cellulose.

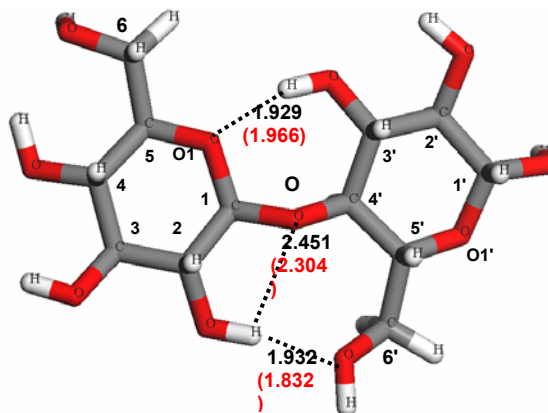


Figure 1. Cellobiose as a model for cellulose. The dotted lines represent the intramolecular hydrogen bonds.

*(COLOR CODE: grey=carbon, white=hydrogen, red=oxygen, green=chlorine, blue=palladium, brown=copper)

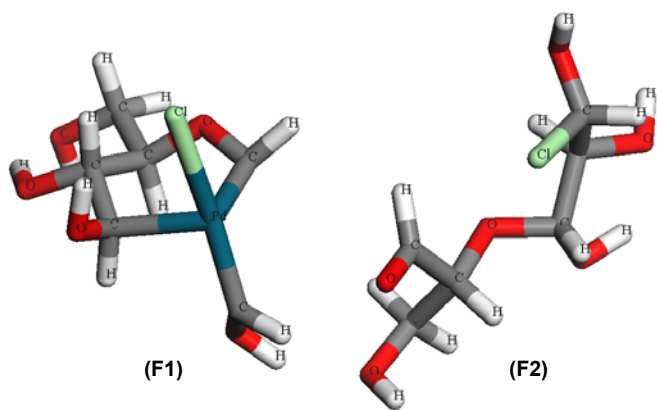


Figure 2. The fragments obtained from the interaction of PdCl_2 and cellobiose. F1 is the fragment containing the Pd atom (shown in blue).

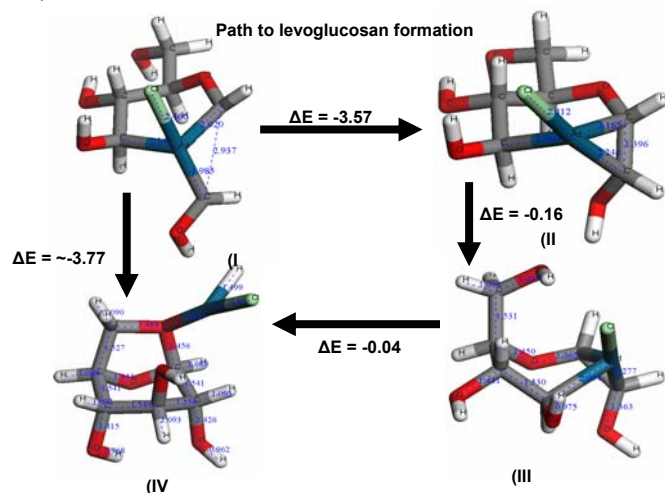


Figure 3. Proposed mechanism for levoglucosan formation.

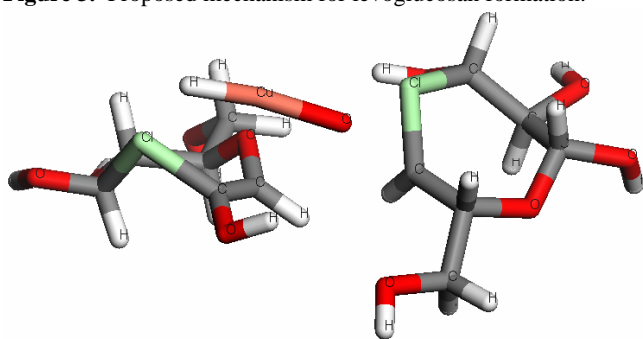


Figure 4. Fragmentation patterns from the interaction of CuCl_2 and cellobiose. Cu is denoted in brown.

IV. Conclusions

The reactions between Pd, PdCl_2 , CuCl_2 and cellobiose have been investigated in detail. Pd undergoes insertion to a C-C bond very easily. While PdCl_2 is shown to promote polymeric chain cleavage and ring rearrangements, facilitated by the 'anchoring' effect, as a result of its affinity towards carbon, on the contrary, CuCl_2 is seen to have no affinity towards carbon. This results in open chain organics to be more thermodynamically feasible products from Copper (II) chloride, as opposed to the levoglucosan formation from Palladium (II) chloride.

Acknowledgement. The authors (BC and BR) wish to thank Geoff Chan for very helpful discussions as well as Firooz Rasouli for guidance. Authors (BKR, PJ and SNK) acknowledge Philip Morris USA for financial support in this work.

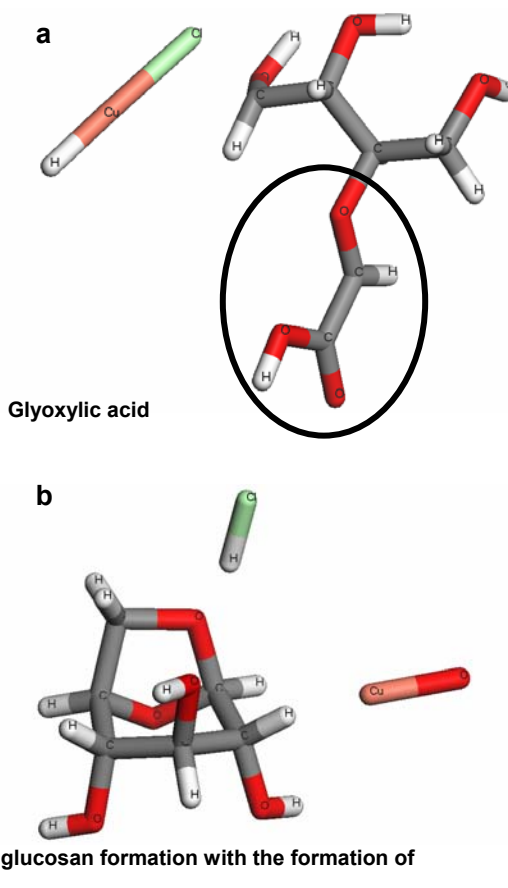


Figure 5. The two products obtained from the interaction of CuCl_2 and cellobiose. (b) is 4.02 eV higher in energy than (a).

References

1. Junicke, H.; Bruhn, C.; Kluge, R.; Serianni, A. S.; and Steinborn, D. *J. Am. Chem. Soc.*, **1999**, 121, 6232; Yang, L.; Su, Y.; Xu, Y.; Wang, Z.; Guo, Z.; Weng, S.; Yan, C.; Zhang S.; and Wu, J. *Inorg. Chem.* **2003**, 42, 5844.
2. Liodakis, S.E.; Statheropoulos, M. K.; Tzamtzis, N. E.; Pappa, A. A.; and Parissakis, G. K., *Thermochim. Acta*, **1994**, 278, 99; Essig, M. G.; Richards, G. N.; Schenck, E. M. In *Cellulose and Wood Chemistry and Technology*; Schuerch, C., Ed.; Wiley, New York, 1989; pp. 841-; Ed Schuerch, C., Shafizadeh, F. In *The Chemistry of Solid Wood*; Rowell, R., Ed.; American Chemical Society, Washington DC, 1984.
3. McGrath, T. E.; Chan, W. G.; and Hajaligol, M. *J. Anal. Pyrolysis*, **2003**, 66, 51; and references therein.; McGrath, T. E.; Hajaligol, M.; *Fuel Chemistry Division Preprints*, **2001**, 46(1), 182; and references therein.
4. Soares, S.; Ricardo, N. M. P. S.; Jones, S.; Heatley, F. *Eur. Poly. J.*, **2001**, 37, 737.
5. Nishiyama, Y.; Langan, P.; and Chanzy, H. *J. Am. Chem. Soc.*, **2002**, 124, 9074; Nishiyama, Y.; Sugiyama, J.; and Chanzy, H.; and Langan, P. *J. Am. Chem. Soc.* **2003**, 125, 14300.

SMALL SOLUTE ROTATIONAL DYNAMICS AS A PROBE OF LOCAL SOLUTION STRUCTURE IN A MIXED-SOLVENT SYSTEM

John E. Adams, Ali Siavosh-Haghighi, and Sanaa K Deshmukh

Department of Chemistry
University of Missouri-Columbia
Columbia, MO 65211-7600

Introduction

Although there have been several theoretical studies of neat supercritical (SC) solvents, both polar and non-polar, such is not the case for SC mixed solvents. Indeed, the microscopic properties of these systems remain largely uncharacterized, although there certainly are measurements of solubilities and extraction capabilities reported in the literature for the case of a polar co-solvent.¹⁻³ Previous studies^{4,5} have demonstrated that solute rotational dynamics can yield insight into local solution structure in a supercritical fluid, thus we here adopt that strategy for elucidating structure in a mixed fluid system.

Our particular interest is in CO₂ as the principal solvent component, in part due to its importance in industrial applications, but also because its solvating power can be altered significantly by the addition of a polar co-solvent. Neat CO₂, a non-dipolar solvent, is a less-than-ideal solvent for polar solutes. The addition of 5-10% water, methanol, or 2-propanol, however, increases the range of extractions and separations that can be accomplished.⁶ In the present study, we investigate the details of the local solution structure in a CO₂/5% methanol solvent, the particular solutes of interest being small, substituted benzenes. In previous work, we showed that these solutes exhibit dynamical behavior ranging from ballistic to diffusive rotational motion, depending on the time scale and the solvent density.⁷ The net dipole moments of these solutes proved less important in determining their dynamics in neat non-dipolar CO₂ than did the physical sizes of the substituent groups. One does not expect this result to obtain, though, when a solvent component is polar, and it is this expectation that prompted the present work.

Methodology

The system considered here consists of 974 CO₂ molecules, 50 methanol molecules, and a single solute molecule thermally equilibrated in a cubic cell with periodic boundary conditions in three dimensions. The *Moldy*⁸ code was used for this purpose. Potential energy functions adopted in this work are the CO₂ potential of Harris and Yung⁹, the methanol potential developed by Ferrario and co-workers¹⁰, and OPLS solute potentials as described by Jorgensen.¹¹ Intermolecular Lennard-Jones potential parameters were obtained using the conventional OPLS geometric-mean combining rules. From this equilibrated system we obtained radial distribution functions (RDFs) and “two-dimensional” density contours, the latter calculated by projecting the local density within a solvent slab centered on the solute molecule onto a plane containing the solute’s center of mass.

The dynamics of the solute molecule was characterized by calculating orientational correlation functions of the form

$$C_\ell(t) = \langle P_\ell(\mathbf{u}(0) \cdot \mathbf{u}(t)) \rangle,$$

where the average is of the ℓ th Legendre polynomial, the vector \mathbf{u} being taken in the direction of the molecule’s dipole moment. Also calculated were angular velocity correlation functions,

$$C_\omega(t) = \langle \boldsymbol{\omega}(t) \cdot \boldsymbol{\omega}(0) \rangle / \langle \omega^2(0) \rangle.$$

These calculations were carried out in the same way as in our previous neat-fluid studies.^{4,5,7}

Results and Discussion

Radial Distribution Functions. We first consider the gross solution structure as revealed by radial distribution functions. Figure 1 shows the RDFs for methanol relative to the centers of mass of four solute species.

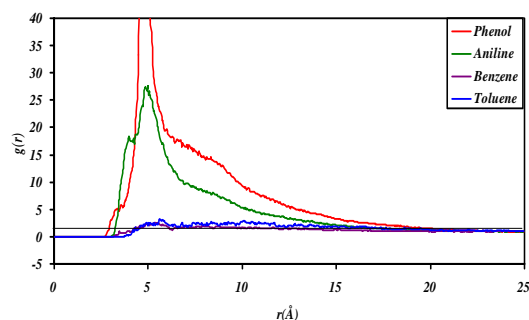


Figure 1. Solute-methanol radial distribution functions for a system bulk number density of $2.77 \times 10^{-3} \text{ Å}^{-3}$. The height of the first peak of phenol rises to 66.4, but the peak position is at 4.8 Å for all solute molecules

One immediately sees that the local concentration of methanol depends sensitively on the solute’s dipole moment, with the results for benzene ($\mu=0$) and toluene ($\mu=0.24\text{D}$) differing negligibly from one another but with significant localization of methanol being revealed about the polar aniline ($\mu=1.34\text{D}$) and phenol ($\mu=2.11\text{D}$) solutes. (The quoted dipole moments are those predicted by the OPLS potentials used in this work.¹¹) Also notable is the increased extent of the cybotactic region of a dipolar solute when the solvent includes a dipolar ($\mu=2.23\text{D}$) co-solvent.

Just as significant is the change in the distribution of CO₂ molecules as a result of the addition of methanol. This change is highlighted in Figure 2, which shows relevant RDFs for benzene and phenol with and without the inclusion of the co-solvent.

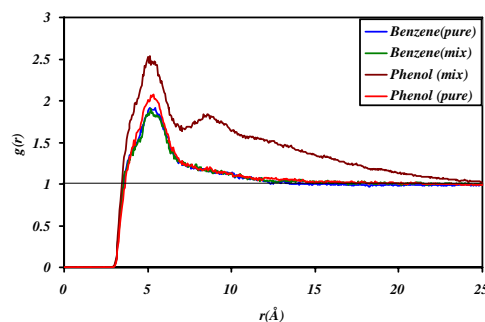


Figure 2. Radial distribution functions of CO₂ with respect to the centers of mass of benzene and phenol for the cases of mixed solvent (CO₂+5mol% MeOH) and a pure solvent (CO₂) at a bulk number density of $2.77 \times 10^{-3} \text{ Å}^{-3}$.

It is clear that the cybotactic region of non-polar benzene is unchanged upon the addition of methanol, and that there is only a minor difference observable when phenol is the solute and the solvent is neat CO₂. Quite different, though is the case of phenol dissolved in the mixed solvent system. For that case not only is there an increase in the carbon dioxide concentration in the first solvation shell, there is clear evidence of structured, enhanced CO₂ density at

longer distances as well. The conclusion suggested by both sets of RDFs is that not only does a polar co-solvent tend to concentrate in the cybotactic region of a polar solute molecule, but in addition there is an additional enhancement of the concentration of the non-polar solvent component, one that assists in the solvation of the polar co-solvent.

The particular concentration of methanol in the vicinity of the phenolic group is revealed when one examines the methanol density contours. Evident there is a selective local density enhancement resulting from the polar solute group interacting with the polar solvent component. In the case of benzene, the analogous density contours are essentially isotropic and indicative of a lesser enhancement.

Correlation Functions. The effect of the addition of a polar co-solvent is also evident in the rotational correlation functions described above. In Figures 3 and 4 are the results for phenol of the calculation of C_1 and C_ω .

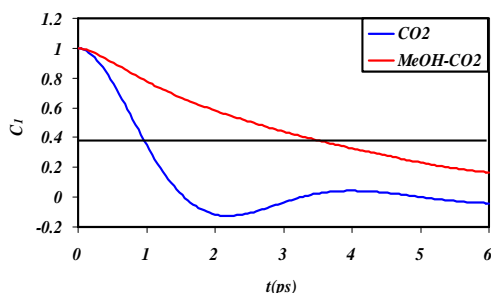


Figure 3. Orientational correlation functions for phenol dissolved in pure CO_2 solvent (blue lines) and in a CO_2 /methanol mixed-solvent (red lines). The horizontal line is at e^{-1} ; the time at which the correlation function crosses this line is the correlation time.

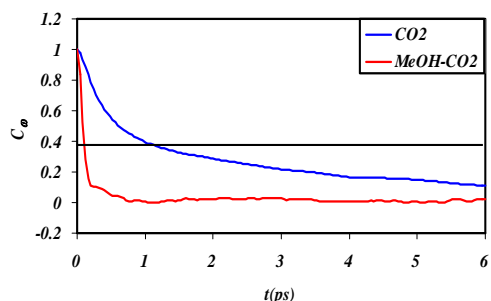


Figure 4. Angular velocity correlation functions for phenol dissolved in pure CO_2 solvent (blue lines) and in a CO_2 /methanol mixed-solvent (red lines).

Note that the presence of the methanol is associated with a slowing of the rotational reorientation of the phenol molecule, the characteristic correlation time increasing by a factor of roughly 3.5, with the orientational correlation time here being defined as the time over which the correlation function decays to a value of e^{-1} . (As noted in previous work⁵, the definition of correlation times is not unique when the rotational motion is not in the diffusive limit.) One also finds a concomitant reduction in the angular velocity correlation time, corresponding to an increase in the solute-solvent interactions leading to “scrambling” of the angular velocity. This result too is entirely consistent with the picture emerging from the RDFs.

Conclusions

We have shown through appropriate molecular simulations how the addition of a polar co-solvent alters the local solution structure of SC CO_2 in the vicinity of a polar solute. Not only is there an enhancement of the co-solvent concentration in the solute’s cybotactic region, there is also an enhancement of the CO_2 density beyond that seen in the neat-solvent case. These structural effects are manifested both in the solute-solvent RDFs and in the rotational correlation functions, effects that are absent when the solute is non-polar. Accordingly, one expects the solvating properties of a non-dipolar solvent such as carbon dioxide to be extended significantly with the addition of the co-solvent.

References

- (1) Tonthubthimthong, P.; Doublas, P. L.; Douglas, S.; Luewisutthichat, W.; Teppaitoon, W.; Pengsopa, L. *J. Supercrit. Fluid*, **2004**, *30*, 287.
- (2) Kometani, H.; Okamoto, J.; Asami, K.; Yonezawa, Y. *J. Phys.: Condens. Matter* **2002**, *14*, 11437.
- (3) Rosenthal, S. J.; Jimenez, R.; Fleming, G. R.; Kumar, P. V.; Maroncelli, M. *J. Mol. Liq.* **1994**, *60*, 25.
- (4) Siavosh-Haghighi, A.; Adams, J. E. *J. Phys. Chem. A* **2001**, *105*, 2680.
- (5) Adams, J. E.; Siavosh-Haghighi, A. *J. Phys. Chem. B* **2002**, *106*, 7973.
- (6) Chatzis, G.; Samios, J. *Chem. Phys. Lett.* **2003**, *374*, 187.
- (7) Siavosh-Haghighi, A.; Adams, J. E. *manuscript in preparation*.
- (8) Refson, K. *Moldy* 2.15 ed, **1999**.
- (9) Harris, J. G.; Yung, K. H. *J. Phys. Chem.* **1995**, *99*, 12021.
- (10) Ferrario, M.; Haughney, M.; McDonald, I. R.; Klein, M. L. *J. Chem. Phys.* **1990**, *93*, 5156.
- (11) Jorgensen, W. L.; Laird, E. R.; Nguyen, T. B.; Tirado-Rives, J. *J. Comput. Chem.* **1993**, *14*, 206.

GIBBS ENSEMBLE MONTE CARLO WITH WORK-BIAS PARTICLE INSERTIONS IN THE SIMULATION OF A PHASE DIAGRAM

Donald K. Phelps[‡] and Nicholas J. Scocozzo[†]

[‡] Air Force Research Laboratory, Propulsion Directorate,
AFRL/PRTG Bldg 490, 1790 Loop Rd N., Wright-Patterson AFB,
OH 45433; [†] Carnegie Mellon University, 5000 Forbes Ave.,
Pittsburgh, PA 15289,

Abstract

Gibb's Ensemble Monte Carlo (GEMC) is a technique which in principle can calculate the phase composition of any condensed phase for which potential parameters are available. However, the particle (molecule) insertions required for this technique are very difficult even with configurational bias methods. Here we will discuss the implementation of work-bias techniques to improve computational performance. The 2-butoxyethanol and water system has been selected for study due to its similarity to the di-ethylene glycol mono-methyl ether (DIEGME) and water system which often forms a mixture known as "apple jelly" in jet fuel storage tanks. Phase diagrams for 2-butoxyethanol-water are available for comparison making it a good test system. The phase diagram has both upper and lower consolute boundaries. This atypical behavior, also makes this system a good test of the GEMC simulation technique. Our work shows that these calculations require large amounts of computer time to converge. Predicted phase boundaries for this system have been calculated with the Towhee GEMC simulation code¹ with and without the work-bias particle insertions. Differences between calculated and experimental phase diagrams are discussed and related to the deficiencies of these calculations.

Introduction

An understanding of the complex phase properties of mixtures can enhance our ability to understand and mitigate problems with jet fuels and fuel systems. To date, experimental measurements have been the primary means by which fuel properties are determined. A few software tools have been developed which can aid in the prediction of important phase properties of fuels. The programs include SUPERTRAPP² and PPDS³. These programs have restrictions on the composition of the fuels for which they are effective. SUPERTRAPP has been parameterized to work strictly with hydrocarbons and is limited to 20 components⁴ from a list of 200 while PPDS can handle as many as 50 components selected from 1500 compounds. Neither is capable of providing predictions for an arbitrary combination of hydrocarbons. The current work is Monte Carlo simulation based and will in principle have no limitations in the number of components or in the composition of those components.[†]

The Towhee simulation code provides a means of obtaining a prediction of the composition of phase; however, currently it takes several months of cpu time to obtain information about compositions of phases of the 2-butoxyethanol-water system at a single temperature. In order to accelerate the convergence of these calculations we have introduced Athènes⁴ work-bias method to the Towhee GEMC simulation code. The work-bias method provides a

more efficient means of moving large molecules into condensed phases as described below.

Computational Method

The Monte Carlo for Complex Chemical Systems (MCCCS) program Towhee is a freely available Gibb's Ensemble Monte Carlo program developed by Marcus Martin of Sandia National Laboratories in collaboration with Prof. Ilja Siepmann and his research group at the University of Minnesota.

Panagiotopoulos introduced the Gibb's Ensemble Monte Carlo (GEMC) method in 1987⁵. In the GEMC method, each phase is set up as a separate simulation region which has its own composition and density. The separate phases are in thermodynamic equilibrium with one another but are not in physical contact. This removes the effect of interfaces from the simulation. In the course of the simulation a variety of moves of molecules in the separate simulation regions are performed: (1) random movements of particles (molecules) within the box of origin; (2) equalization of pressure through volume fluctuations in the individual simulation boxes; (3) random movements of particles (molecules) between simulation boxes. These movements allow the system to come to thermodynamic equilibrium; thus, the temperature, pressure and chemical potentials of components are the same in each of the simulation regions once the calculation has converged.⁵ More sophisticated molecule moves are available in the Towhee code and were used in the course of this study. These will be discussed briefly during the oral presentation. We have added the Athènes work-bias move to Towhee to improve computational performance and will discuss this move in detail. Briefly, a molecule is moved to a random location within one of the simulation boxes but without immediately calculating the full energy of interaction with the surrounding molecules. Instead, the potential for that molecule is slowly turned on over the course of many moves of surrounding molecules. Thus, the surroundings will relax enhancing the probability that a molecule can be transported successfully into a dense phase. Overall, on a constant cpu time basis, many more molecules are transferred between dense phases than without the work-bias move.

A variety of parameters are available for use with Towhee, including OPLS-aa, OPLS-ua⁶, TraPPE-UA⁷, TraPPE-EH⁸. We selected OPLS-aa (i.e. all-atom) parameters due to the importance of hydrogen bonding. Other potential functions were deemed likely to overlook interactions that may be important to the description of the phase behavior.

The system is comprised of three boxes. Initially box 1 contained 65 2-butoxyethanol molecules (see Figure 1 for structure), box 2 contained 500 water molecules, and box 3 contained 50 Helium atoms. The Helium is present to populate the vapor phase while 2-butoxyethanol and water are the primary components of the two liquid phases.

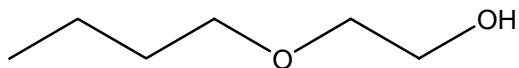


Figure 1. Structure of 2-butoxyethanol.

The system was equilibrated at 1 atm and at temperatures from 300 K to 410 K. The system is equilibrated with between 60,000,000 and 110,000,000 Monte Carlo steps.

Results and Discussion

The calculated phase diagram is shown in Figure 2 alongside the experimental data of Cox and Cretcher⁹. There are clearly some large differences between the compositions of the simulated phases

* This program will allow one of the components to be water at up to 5 mol %.

[†] This method works best for liquid and gas phases. Solid phase calculations would require the introduction of new methodology to the simulations.

and the compositions of those phases found by experiment. However, the basic shape of the curve is beginning to appear in the lower portion of the figure (Temperatures 330-350 K). There are some significant outliers (e.g. T=370 K) but the appearance of a lower phase

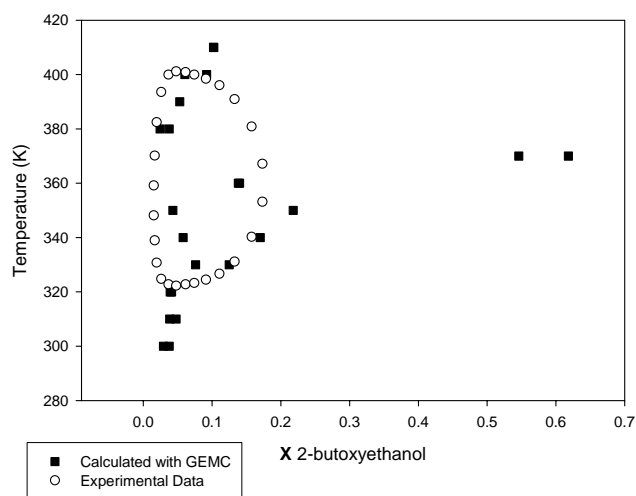


Figure 2. Phase Diagram 2-butoxyethanol – water Comparison of Calculation to Experiment.

boundary is encouraging. It appears that the water rich phase (i.e. to the left side of Figure 2) is closest to the composition found by Cox and Cretcher⁹. The other phase is quite different from the experimental data. At 410 K each of the three simulation boxes have the same mole fractions of 2-butoxyethanol and water. In addition each of the simulation boxes at 410 K has a low density indicating that the system is above its boiling temperature.

Conclusions

This system required several months of cpu time to reach the current state of convergence with Towhee. The introduction of the work-bias move has improved computational performance but it is not yet clear how much faster the calculation will be with this improved methodology. The GEMC method has the potential to solve difficult phase problems if additional improvements in speed can be accomplished. Further improvements in computational performance can likely be attained by the addition of parallelism to the calculation. The GEMC methodology shows promise for being a valuable tool in predicting phase behavior for systems of practical interest as additional improvements in methodology are made.

Acknowledgement. Computer time for these calculations was provided by the US Air Force Major Shared Resource Center (ASC/MSRC). The authors wish to thank Marcus Martin for helpful discussions concerning the Towhee code.

References

- (1) Martin, M. G.; Thompson, A. P. *Fluid Phase Equilibria* **2004**, *217*, 105.
- (2) Ely, J. F.; Huber, M. L. NIST Standard Reference Database 4s NIST Thermophysical Properties of Hydrocarbon Mixtures Database (SUPERTRAPP); 3.0 ed.; U.S. Department of Commerce: Gaithersburg, MD, 1999.
- (3) Johns, A. I.; Watson, J. T. R. *Transport Properties of Fluids* **1996**, 435.
- (4) Athenes, M. *Phys. Rev. E* **2002**, *66*, 046705/1.
- (5) Panagiotopoulos, A. Z. *Mol. Phys.* **1987**, *61*, 813.

- (6) Jorgensen, W. L.; Madura, J. D.; Swenson, C. J. *J. Am. Chem. Soc.* **1984**, *106*, 6638.
- (7) Martin, M. G.; Siepmann, J. I. *J. Phys. Chem. B* **1998**, *102*, 2569.
- (8) Chen, B.; Siepmann, J. I. *J. Phys. Chem. B* **1999**, *103*, 5370.
- (9) Cox, H. L.; Cretcher, L. H. *J. Am. Chem. Soc.* **1926**, *48*, 451.

MOLECULAR DYNAMICS SIMULATIONS OF REVERSE MICELLES IN SUPERCRITICAL CARBON DIOXIDE

Max L. Berkowitz, Sanjib Senapati and Lanyuan Lu

Department of Chemistry, University of North Carolina at Chapel Hill, Chapel Hill NC 27599

Introduction

Supercritical carbon dioxide (scCO₂) is often considered as an ideal solvent substitute because it is a nontoxic, chemically inert, cheap, highly volatile, nonflammable and potentially recyclable fluid. Unfortunately, many important classes of substances e.g. water, biomolecules, polymers exhibit low solubility in scCO₂. Recently, several experimental efforts were focused on finding suitable surfactants that are capable of stabilizing a microdispersion of aqueous phase in scCO₂. Conventional hydrocarbon surfactants used in oil/water systems are shown to exhibit low solubilities in carbon dioxide and therefore, are not capable of solubilizing a significant amount of water. Surfactants with perfluorinated chains, on the other hand, are quite soluble in scCO₂. When placed in scCO₂ a number of fluorinated surfactants are shown to form reverse micelles (RM), therefore they are promising materials for extending water in CO₂ (W/C) microemulsions to a variety of applications e.g. in selective extraction of polar compounds from aqueous solution, in emulsion polymerization schemes, or as a media for reactions between polar and nonpolar molecules.

Small-angle neutron scattering (SANS) experiments on W/C microemulsions were recently performed over a large range of pressure, temperature, and droplet volume fraction [1,2]. These studies revealed the existence of spherical water droplets of radius 2.0 – 3.5 nm dispersed in scCO₂. Various spectroscopic techniques e.g. Fourier transform infrared (FTIR), UV-vis, fluorescence, and electron paramagnetic resonance experiments demonstrated the existence of a bulk water domain in these systems. The formation of nanometer-sized microemulsions was confirmed by small-angle X-ray scattering experiments.

Although useful information about the structure of reverse micelles in microemulsions can be obtained from experiments, computer simulation methods can play a major role in developing our understanding of W/C microemulsions in a more detailed manner and in interpretation of experimental observations. Here we report on our work that uses molecular dynamics simulation technique to investigate the structural properties of the aqueous RM containing PFPECOO-NH₄⁺ surfactant in scCO₂ with a W₀ value of 8.4. Our simulation results show a very good agreement with experimental data and offer detailed information on the shape and structure of the system.

One particular issue we want to focus on is the importance of fluorine atoms in the packing of PFPE tails and related properties e.g. tail solvation. To understand this issue deeper, we performed simulations on systems where we studied a model surfactant, polyether ammonium carboxylate (PE), which is analogous to PFPE except that all fluorine atoms in the PFPE surfactant were replaced by hydrogen atoms.

Simulation Methodology

We performed two sets of molecular dynamics (MD) simulations on systems containing aqueous reverse micelles in supercritical carbon dioxide [3,4]. In the first set of simulations the micelles were pre-assembled; in the second set the micelles were self-assembled. The fluorinated polyether PFPECOO-NH₄⁺ and its non-fluorinated analog PECO-NH₄⁺ were used as surfactants in our

simulations. The consistent valence force field CVFF parameters were used to describe the intermolecular and intramolecular interactions present in the surfactant anions [5]. The CVFF force field has been successfully applied to study the rheological behavior of confined branched and linear perfluoropolyethers and hydrocarboxylic acids. The corresponding potential parameters and also the point charges for the surfactants can be found in Table I of reference [3]. The SPC/E model was chosen to describe water molecules. The OPLS set of intermolecular parameters has been used to model NH₄⁺ counterions. The five-site model of ammonium ion consists of one Lennard-Jones (LJ) site on the central N atom and five sites for point charges. The rigid EPM2 model proposed by Harris and Yung was used to describe CO₂ in the preassembled set of simulations. For reasons of computational economy, a single point model was used to describe the CO₂ molecules in simulations with self-assembly of micelles. We demonstrated previously that this model gives a good description of the scCO₂ equation of state. The cross interactions were obtained by using the Lorentz-Berthelot combining rule. The primary system we simulated contained 554 water molecules, 66 fluorinated surfactant molecules, and 6359 CO₂ molecules placed in a cubic box at 25°C and 200 bar pressure. Thus, the system contained a total of 23775 particles. The values for the temperature, pressure and W₀ are the same as the values present in the NMR studies of water transport in W/C microemulsions [6]. A large number of CO₂ molecules was taken to attain a bulk CO₂ phase and to discard any possibility of inter-droplet (inter-aggregate) interactions due to the application of periodic boundary condition.

Our simulations with preassembled micelles started from a configuration represented by an aggregate in which we distributed the surfactant molecules around the periphery of a sphere of radius 1.6 nm. Surfactant molecules pointed their headgroups inward and their tails outward in the initial configuration. The sphere of radius 1.6 nm was chosen based on the fact that an amount of 554 water molecules can be accommodated in that volume. Extensive equilibration and thermalization of this highly ordered structure was performed, keeping the carboxylate carbon atoms fixed to remove the initial strain. After that, we added water molecules and NH₄⁺ ions to the empty space inside the sphere and performed another set of minimization and thermalization runs, this time letting the carboxylate carbon atoms go free. The obtained structure was then inserted into the hole made in the middle of a cubic box containing CO₂ molecules at the density of 0.95 g/mL. The value for the density of CO₂ in the box was taken to be slightly higher than the desired value of 0.92 g/mL corresponding to the experimental density. This was done on purpose, since we expected that some carbon dioxide molecules will diffuse into the inter-tail region of the micelle and therefore will bring down the bulk density of CO₂ to a value somewhat closer to the desired value. The final set of minimization and thermalization runs was performed before a 500 ps equilibration run. To enable the volume variation, the equilibrations and production runs were performed in NPT ensemble with the thermostat and barostat relaxation times set to 0.5 ps. The configuration obtained at the end of 500 ps run provided the initial configuration for the production run of 5 ns.

The other system we simulated in the set with pre-assembled micelles contained the same number of water, CO₂ and surfactant molecules, only this time the 66 surfactant molecules were hydrogenated analogues of PFPE molecules. Again, the simulation was done at 25° C and 200 bar pressure and it was started from an aggregated configuration. A 500 ps equilibration run was then performed before a production run of 5 ns in NPT ensemble.

To understand the factors that determine micelle formation, we performed a set of self-assembling simulations starting with random configurations of all molecules in the system. In two of these

simulations, the simulation box contained 554 water molecules, 66 fluorinated surfactant molecules ($W_0=8.4$), and 6359 CO_2 molecules. These numbers of particles are exactly the same as in the simulation of preassembled micelles. In the first simulation the molecules were initially distributed randomly, and in the second, the initial positions were distributed on a regular lattice. In both simulations, we observed the evolution of the system from the initial configuration to a spherically shaped RM configuration. We also investigated the effect of different W_0 on the process of the micellar formation. Thus, we performed three more simulations on systems containing a) 66 surfactant and 1108 water molecules, b) 66 surfactant and 270 water molecules, and c) 66 surfactant and 139 water molecules.

Three dimensional periodic boundary conditions were employed in all simulations. The calculation of long-range Coulombic forces was performed using the Smooth Particle Mesh Ewald (SPME) method. The real space part of the Ewald sum and Lennard-Jones interactions were cut off at 1.0 nm.

Results and Discussion

The general structural properties of a reverse micelle can be characterized by the size and shape of its aqueous core. A useful statistical measure of the size of a micelle is the radius of its aqueous core, R_c . Our calculations resulted in a value of 1.92 nm for R_c , in a good agreement with the value of 2.0 nm extracted from experiments [6]. The time history of this aqueous core radius showed that the aggregated core was stable during the entire 5 ns of the production run in pre-assembled simulations. The measurement of eccentricity of the RM, which provides information on the shape of this micelle, showed that the fluorinated micelle remained nearly spherical in shape during the simulation time. For a visual inspection of the RM, we present a snapshot of the micellar aggregate on Figure 1. In this snapshot the solvent molecules are intentionally hidden to see the micellar aggregate clearly. As we can see from the picture, our micelle is essentially spherical. Another important structural quantity we can calculate is the surface area per headgroup (A_h) available for the interaction with water. This can be estimated by using the equation connecting the surface area A_c of the aqueous core with the number of surfactant molecules N_h ,

$$A_c = 4\pi R_c^2 = A_h N_h.$$

Using the calculated value of $R_c = 1.92$ nm and $N_h = 66$, we get $A_h = 0.70$ nm². This value of surface area is consistent with the value estimated from the experiment (0.76 nm²).

Experimental studies indicate that surfactants with fluoroalkyl or fluoroether tails exhibit high solubility in scCO_2 . We have determined the average solvation number of the surfactants by counting the number of CO_2 molecules in the first solvation shell of the surfactants. We noticed a substantial overlap between the solvation shells of two adjacent atoms in the same chain (intra-chain). A substantial overlap is also seen between the solvation shells of atoms in the adjacent chains (inter-chain). The latter is particularly true for those atoms that are closer to headgroups, since the curvature is larger in this region. Therefore, while calculating the solvation number, we counted each CO_2 molecule in the tail region just once. The average value of the solvation number we got for the fluorinated surfactant is 15.

A molecular graphics analysis shows that the interior aqueous core is somewhat exposed to CO_2 . To get a quantitative estimate of the core exposure, we calculated the core surface area exposed to CO_2 by using the method of Lee and Richards [7]. Following this method, we removed all of the CO_2 molecules from the system and rolled a probe across the surface of the micelle. The contributions to accessible area from water and ammonium counterions were summed

up to estimate the core exposure. For comparison, the area of a bare aqueous core was also calculated by removing the surfactant molecules from the system. A 0.2 nm probe was utilized to mimic the CO_2 molecules in the system. We observed that the average value of the accessible surface area for bare aqueous core is ~ 70 nm², which should be compared with the area of ~ 8.4 nm² when the surfactants are present in the system. These values show that about 12 % of the aqueous core is exposed to CO_2 . We also noticed that the calculated value of the surface area for bare aqueous core is higher than the value that can be computed using the expression that contains R_c . This is due to the fact that the surface of the micellar core is not smooth; it is rather corrugated and rough.

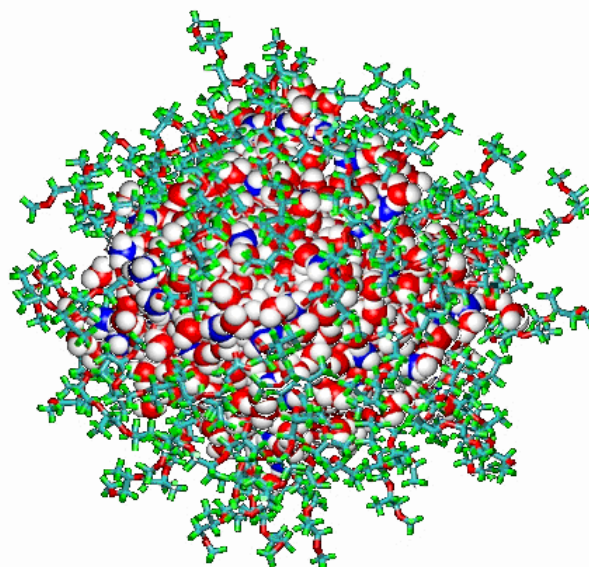


Figure 1. Snapshots of the fluorinated micelle. The solvent molecules are omitted for clarity. Color scheme: red balls, water oxygens; white balls, either water or ammonium hydrogens; blue balls, nitrogens of the ammonium cation. The surfactant anions are represented by sticks: red sticks, oxygens; cyan, carbon atoms; green sticks, fluorine atoms in the surfactant chains.

To understand the difference in the properties of RM containing surfactants with perfluorinated chains and non-fluorinated chains, we simulated an aqueous reverse micelle composed of non-fluorinated PECOONH_4^+ surfactants in scCO_2 . Since we are not aware of any experimental information about microemulsions created in systems with hydrogenated analog of PFPE, we were not able to use experimental information to set up the system. Therefore, the system we simulated (system 2) contained 554 water molecules, the same number of water molecules as in fluorinated system (system 1). Starting from an aggregated configuration, we equilibrated the system 2 for 500 ps followed by a 5 ns production run. We observed a distinct difference that existed between system 2 and the fluorinated surfactant system: the reverse micelle in system 2 had a much larger exposed aqueous core area. To obtain a quantitative

estimate of the aqueous core exposure area in system 2 we again used the method of Lee and Richards as described above. The exposed aqueous core area for the non-fluorinated system was found to be 32 % compared to 12 % in the case of fluorinated system. As a result, a larger contact between CO₂ and water molecules is established in system 2. The large exposed core area has a form of patches that can be clearly seen in Figure 2. Why do we get these patches? Since the hydrogenated surfactant is smaller in size it is expected that in an assembly of hydrogenated surfactants the area covered by headgroups is smaller. If the number of water molecules inside the micellar pool is fixed, one ends up with regions where direct contact is established between water and carbon dioxide. In experimental situation water in the interior of the micelle will be exchanged with the exterior until micelle will acquire its minimum free energy. Since we use a canonical ensemble that fixes the number and type of molecules in the system and the length of our simulations is orders of magnitude shorter than the one needed to observe the major restructuring of the micellar system, we need to look for another strategy to perform a reasonable comparison of systems containing micelles with fluorinated or hydrogenated tails. This strategy may be self-assembly (see below).

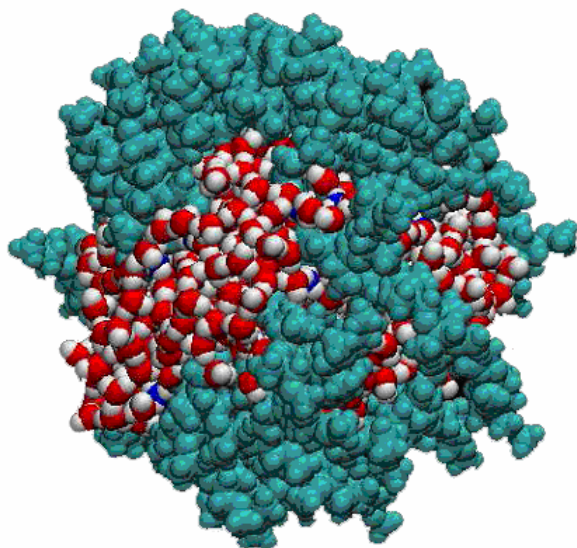


Figure 2. Exposure of the interior aqueous core in system 2. Color scheme: red balls, water oxygens; white balls, either water or ammonium hydrogens; blue balls, nitrogens of ammonium cation; cyan balls, surfactant molecules. The solvent molecules are omitted for clarity.

We determined the average solvation number for non-fluorinated surfactants by counting the number of CO₂ molecules in the first solvation shell. The average value of the solvation number we got was 10. This should be compared to 15 obtained for the fluorinated surfactant. Thus, we observed that due to clustering of hydrogenated surfactants their solubility is ~33% lower in CO₂ compared to the fluorinated analog.

In the previously described simulations the micelles were not self-assembled, but for the purpose of saving the computational time, were initially preassembled. Although micelles were in a non-equilibrium state at the beginning of the simulations, they changed their conformations during the molecular dynamics run, and

presumably reached their equilibrium state. Experimental information about micellar sizes is needed to prepare the initial micelle in these cases. If this information is unavailable, one can not pre-assemble the micelle and therefore a self-assembly has to be performed on the computer.

In general, the self-assembly of a micelle should be preferred in computational studies, since less dependence on the initial conditions (and number of particles) is expected to appear in the simulation. Computer simulation of self-assembly is a challenge for computational studies. With the increasing power of modern computers, it is now possible to study various self-assembly processes in atomic detail using MD simulations. In recent years, Marrink and co-workers [8] observed the spontaneous aggregation of direct micelles, bilayers and vesicles. In these simulations the typical time scale of self-assembly was ~10-100 ns or even longer. The self-assembly of a RM in a three component system containing water/surfactant/oil (or sCO₂) has never been simulated satisfactorily, though was attempted.

As we already mentioned it Methodology section, we performed a set of molecular dynamics simulations of RM self-assembly. To understand the factors that determine micelle formation, a series of simulations was performed. In two of the simulations, the simulation box contained 554 water molecules, 66 fluorinated surfactant molecules ($W_0=8.4$), and 6359 CO₂ molecules. These numbers of particles are exactly the same as in the previously described pre-assembled simulations. In the first simulation of self-assembled systems all the molecules were initially distributed randomly, and in the second, the initial positions were distributed on a regular lattice. In both simulations, we observed the evolution of the system from the initial configuration to a spherically shaped RM configuration. Figure 3 displays a series of snapshots illustrating this evolution. Analysis of the average distances between molecules showed that the self-assembly process was completed after ~5 ns, indicating that the process is rather fast.

From our simulation we observed that during the first stage of rearrangement (~1 ns) water molecules and surfactant molecules clustered into several small micelle-like aggregates. The fast first stage was followed by a slower process during which three or four small micelles merged into two. The final rearrangement of the last two micelles into one spherical RM was the most time consuming process. Analysis of the RM structure (we calculated the core radius, area per headgroup, eccentricity, and the fraction of gauche angles for surfactant chains) obtained after ~5 ns of self-assembly showed little difference from the pre-assembled simulations.

We investigated the effect of different W_0 on the process of the micellar formation. Thus, we performed three more simulations on systems containing a) 66 surfactant and 1108 water molecules, b) 66 surfactant and 270 water molecules, and c) 66 surfactant and 139 water molecules. In all cases we also observed self-assembly, and in cases a) and b) the micellar shape was spherical. In case c) the micelle had a worm-like shape. Although in case a) the micelle remained spherical and the surfactants were uniformly distributed over the surface of the sphere, we observed a larger contact between water and sCO₂ due to a large surface area of the water core.

We also performed a set of simulations with the PE surfactant. In the simulation containing 66 PE surfactants and 554 water molecules, we observed self-assembly into a micellar type aggregate, but with one side of this aggregate having a direct water/sCO₂ contact (See Figure 4). Such a contact increases the surface tension and therefore the free energy of the micelle, indicating that in our system, the PE surfactant is not effective for creation of a microemulsion. To see if we could create a RM micelle containing a uniform distribution of PE surfactants, we decreased the number of water molecules in few other simulations with PE. In each of these

cases we observed aggregates containing regions of direct contact between water and CO₂, like those observed in Fig. 4. When the number of water molecules became small, the aggregate had a worm-like shape.

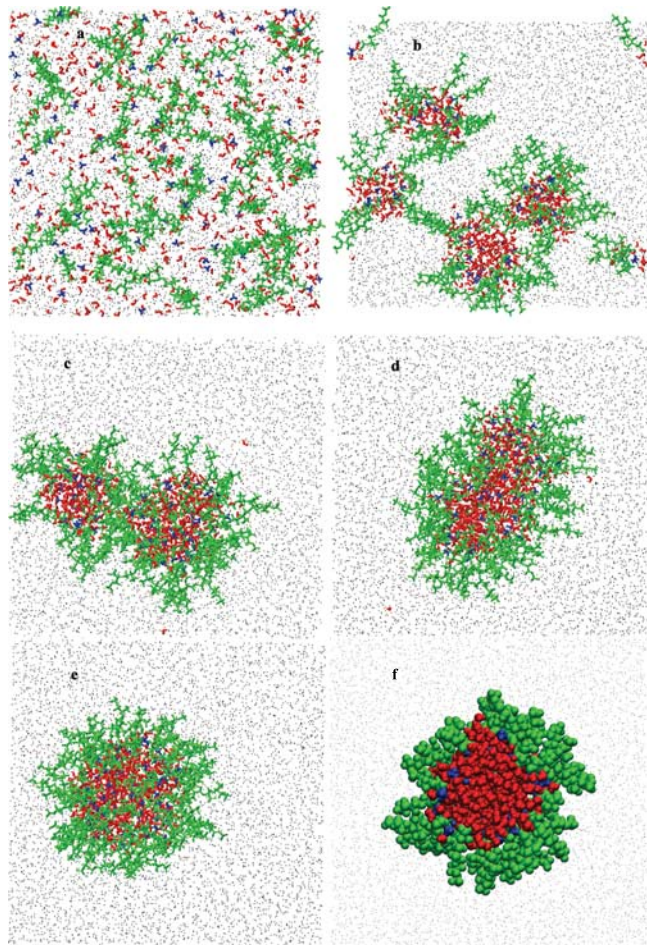


Figure 3. Snapshots of the PFPE RM self-assembly (554 water and 66 surfactants). Red, blue, and green particles are water, ammonium ions and PFPE anions, respectively. Small black dots are carbon dioxide molecules. The snapshots are taken at a. 0 ns; b. 1 ns; c. 4 ns; d. 4.4 ns; e. 5 ns; f. 50 ns; This snapshot is of a cut across the micelle to show water in the core and surfactants at the surface.

Conclusions

Molecular dynamics simulations provide a powerful tool to gain detailed molecular information about structural and dynamical properties of reverse micelles that is otherwise very difficult, even sometimes impossible, to get by means of experiments or using analytical theoretical techniques. Here we report results obtained from simulations on reverse micelles created in a ternary system: surfactant/water/supercritical carbon dioxide. In the simulation with the pre-assembled PFPE surfactant we used experimental data to determine the number of particles in the system. For this system we observed a stable spherically shaped micelle that displayed geometrical properties in pretty good agreement with experiments. When we replaced fluorine atoms in the surfactant molecules with hydrogen atoms, and preserved the value of W_0 we observed a strong increase in the direct contact between water and CO₂. This should result in an increase of the system free energy and therefore

destabilize the micelle, thus providing support to the idea that fluorinated surfactant molecules are helpful for the production of microemulsions in water/carbon dioxide systems.

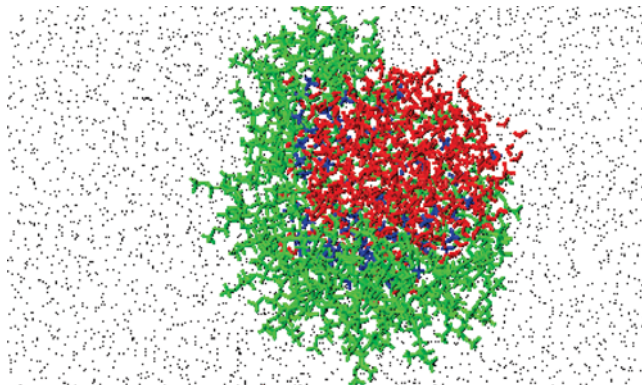


Figure 4. The equilibrated configuration of the PE system. The color scheme is the same as in Figure 3, except the surfactant anions are PE anions. The region of direct contact between water and carbon dioxide is in the upper-right corner of the aggregate.

We also showed, for the first time, that simulating a system containing three components such as water, scCO₂, and polyether surfactants on a relatively detailed atomic level, one can observe a self assembly of molecules after relatively short periods of time. When the surfactant is fluorinated (PFPE) the self assembled aggregate represents a nicely shaped RM. In this case stable RMs are observed for a wide range of W_0 . When a hydrogenated analogue of the PFPE surfactant is used, an aggregate represents a micellar-like assembly with a non-uniform distribution of surfactant molecules, thus creating a large contact area between water and CO₂, indicating that the hydrogenated analogue of PFPE is not a good agent for creating microemulsions in w/c systems. If in general, RMs are quickly assembled in computer simulations, then, with detailed descriptions of molecules, one can study these micelles in detail in their most stable states.

Acknowledgement. This work was supported by the Kenan Center for the Utilization of Carbon Dioxide in Manufacturing and the STC Program of the National Science Foundation under Agreement CHE-9876674. Conversations with Prof. DeSimone were very useful.

References

- (1) Keiper, J. S.; Simhan, R.; DeSimone, J. M.; Melnichenko, Y. B.; Wignall, G. D.; Frielinghaus, H. *J. Am. Chem. Soc.* **2002**, *124*, 1834.
- (2) Steytler, D. C.; Rumsey, E.; Thorpe, M.; Eastoe, J.; Paul, A.; Heenan, R. K. *Langmuir* **2001**, *17*, 7948.
- (3) Senapati, S.; Berkowitz, M. L. *J. Phys. Chem. B* **2003**, *107*, 12906-12916.
- (4) Lu, L.; Berkowitz, M. L. *J. Am. Chem. Soc.* **2004**, *126*, 10254-10255.
- (5) da Rocha, S. R. P.; Johnston, K. P.; Rossky, P. J. *J. Phys. Chem. B* **2002**, *106*, 13250.
- (6) Nagashima, K.; Lee, C. T.; Xu, B.; Johnston, K. P.; DeSimone, J. M.; Johnson, C. S., Jr. *J. Phys. Chem. B* **2003**, *107*, 1962.
- (7) Lee, B.; Richards, F. M. *J. Mol. Biol.* **1971**, *55*, 379.
- (8) (a) Marrink, S. J.; Tieleman, D. P.; Mark, A. E. *J. Phys. Chem. B* **2000**, *104*, 12165-12173. (b) de Vries, A.; Marrink, S. J.; Mark, A. *Biophys. J.* **2003**, *84*, 463A-463A. (c) Marrink, S. J.; Mark, A. *Biophys. J.* **2003**, *84*, 135A-135A.

STRUCTURAL AND ELECTRONIC PROPERTIES OF SULFUR ADLAYER ON Pd(111) SURFACE

Dominic R. Alfonso

National Energy Technology Laboratory, Pittsburgh, PA 15236,
USA

Parsons Project Services, Inc., South Park, PA 15129, USA

Introduction

Palladium is used as selective catalysts in a variety of processes in the chemical industry that involve the conversion of hydrocarbons. Typical large scale applications include the hydrogenation of organic fine chemicals, aromatic hydrogenations and petroleum refining.¹⁻³ Palladium has also found widespread application in the area of hydrogen storage and separation because of the high solubility of hydrogen in the metal. Palladium-based non-porous inorganic membranes capable of separating hydrogen at ppb impurity levels are reported.⁴⁻⁵ However, Pd is found to be susceptible to sulfur poisoning. It has been reported that even the presence of a small amount of sulfur compounds have negative effects on the performance of Pd catalysts and Pd-based membranes.⁶ This can lead to deactivation of these materials after prolonged operation. Considerable financial burden in the chemical and petrochemical industries as a result of uncontrollable and accidental poisoning of sulfur is well documented.⁷

The desire to minimize the negative effects of sulfur poisoning has motivated fundamental research on the interaction of atomic S on single crystal Pd surfaces. In particular, adsorption of S on the Pd(111) surface has been the focus of many experimental investigations.⁸⁻¹¹ The behavior of S on the metal surface is quite varied and depends markedly on the coverage and temperature. At very low coverage ($\Theta > 0.1$ ML), S adsorbates do not form any ordered structures on Pd(111) surface. At coverage $\Theta = 0.1$ ML – 0.33 ML and at room temperature up to ~ 400 K, S adlayer with predominantly $(\sqrt{3} \times \sqrt{3})$ symmetry is identified by low-energy electron diffraction (LEED). From the LEED analysis, the adsorption site of S in $(\sqrt{3} \times \sqrt{3})$ pattern was determined as the three-fold fcc hollow site.¹¹ There is also experimental evidence that Pd(111) surface can support higher concentration of S ($\Theta > 0.5$ ML). Photoemission results show that atomic S is not the only species present on the surface.¹¹ Clearly, the behavior of S on the metal surface as a function of coverage is quite complex. However, there is little fundamental understanding of coverage dependence of the physical and chemical properties of S adsorption on Pd(111).

In the present work, a systematic theoretical study of the physical and chemical properties of S adsorption on Pd(111) as a function of coverage is reported. In order to accomplish this, we performed Density Functional Theory (DFT) calculations for S adlayer on Pd(111) at various coverage. One particular aim is to analyze trends in adsorption energies and provide understanding of the quantum chemical nature of the adsorbate-surface bond in these systems.

Computational Details

First-principles DFT total energy calculations were performed using the Vienna *Ab Initio* Simulation Package (VASP) code.¹² The Perdew-Wang (PW91) generalized gradient approximation (GGA) functional was employed to calculate the exchange-correlation energy.¹³ Core orbitals were described by non-local reciprocal space ultra-soft pseudo-potentials in the Vanderbilt form.¹⁴ The Kohn-Sham one electron valence eigenstates were expanded in terms of plane wave basis sets with cutoff energy below 236 eV. We performed several calculations with larger energy cutoffs and our

results indicate that computed structures and energetics are relatively insensitive to further expansion of the basis set. The Pd(111) surface was modeled by a five-layer slab with periodic boundary conditions in the two directions parallel to the surface (infinite in two dimensions), and separated by a 15 Å thick vacuum region. The lattice constant was fixed to the value obtained from optimizing this constant with DFT for the bulk Pd. The calculated lattice constant for bulk Pd is 3.965 Å, in good agreement with experiment (3.883 Å).¹⁵ To simulate sulfur adsorption on the surface, adsorbates were placed on one side of the slab. The positions of the top three Pd layers and adsorbates were optimized until the forces on all unconstrained atoms were less than 0.02 eV/Å.

Calculations were carried out for coverages ranging from $\Theta = 0.11$ to $\Theta = 1.0$ ML (we define Θ as the ratio of the number of adsorbed atoms to the number of the atoms in the top surface layer). Coverages $\Theta = 0.11, 0.25, 0.33$ and 1.0 ML were calculated utilizing (3×3) , (2×2) , $(\sqrt{3} \times \sqrt{3})$ and (1×1) surface unit cells, respectively (each containing one S atom). For coverage $\Theta = 0.50$ and 0.75 ML, calculations were carried out using (2×2) surface unit cell containing two and three S atoms, respectively. A $(\sqrt{3} \times \sqrt{3})$ unit cell containing two S atoms were employed for coverage $\Theta = 0.66$ ML. The k -point sampling of the two-dimensional electronic Brillouin zone of the periodic supercells was accomplished using Monkhorst-Pack scheme.¹⁶ The density of the Monkhorst-Pack k -point mesh ($13 \times 13 \times 1$, $7 \times 7 \times 1$, $5 \times 5 \times 1$ and $3 \times 3 \times 1$ grids for the (1×1) , $(\sqrt{3} \times \sqrt{3})$, (2×2) and (3×3) surface unit cells, respectively) were chosen high enough to ensure the convergence of the calculated structures and energetics. A Methfessel-Paxton smearing of $\sigma = 0.2$ eV was utilized to improve convergence and the corrected energy for $\sigma \rightarrow 0$ was employed.

Results and Discussion

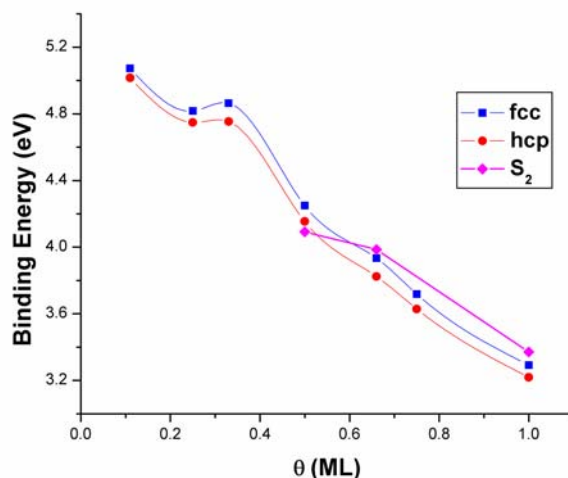


Figure 1. Variation of S binding energy on fcc and hcp sites of Pd(111) surface as a function of sulfur coverage. The results for S₂ species were also included for comparison.

The binding energies for sulfur on the Pd(111) surface in the fcc and hcp hollow sites, with respect to atomic sulfur, are plotted in Fig.1. The fcc site, which is the hollow adsorption site without a second layer atom directly beneath the hollow, was found to be more energetically favorable compared to the hcp site. However, the difference in the binding energy is small (< 0.11 eV/atom) for the

whole coverage range. Adsorption on the other two high symmetry sites (top and bridge sites) was also considered. However, these sites were found to be notably less favorable than the fcc and hcp hollow sites. A repulsive interaction between adsorbates occurs for the coverage range 0.11-0.25 ML, while it switches to attractive when the coverage varies from 0.25 ML to 0.33 ML (see Fig. 1). This attractive interaction indicates island formation with a $(\sqrt{3} \times \sqrt{3})$ structure.

It was observed from STM and LEED experiments that at an average coverage of $\Theta \leq 0.33$ ML, sulfur islands of $(\sqrt{3} \times \sqrt{3})$ symmetry form and merge on a Pd(111) surface, leaving surface areas of palladium unoccupied.⁸⁻¹⁰ Our results are in agreement with these studies. Moreover, according to a number of LEED studies, the preferred adsorption sites for the $(\sqrt{3} \times \sqrt{3})$ S overlayer on Pd(111) are the fcc sites.¹¹ Again, our results are in agreement with these investigations. The sulfur-metal bond length observed in our calculations is 2.27 Å. This is comparable to the values of 2.23-2.28 Å obtained from LEED studies.¹¹ Very similar bond lengths were reported by Rodriguez *et al.* (with *ab initio* approach using 12-atom cluster model of Pd(111)) and by Graviil and Toulhoat (using DFT supercell approach).^{11,17}

The situation changes at higher coverage. As the coverage increases, there is a significant and linear drop in the relative stability of the fcc and hcp sites. This indicates that a repulsive interaction between adsorbates builds up at coverage coverage $\Theta > 0.50$ ML. We also considered the situation in which the S adsorbates form S₂ aggregates on the surface at higher coverage. To simulate S₂ formation on the surface containing 0.50 and 0.66 ML of S initially, we geometrically optimized S₂ molecule on a (2×2) (A) and a $(\sqrt{3} \times \sqrt{3})$ (B) slabs, respectively. For a system containing 1.0 ML of S initially, we optimized a (2×2) slab (C) containing two S₂ molecules. The calculated binding energies (*with respect to atomic sulfur*) are plotted in Fig.1. We found that for coverage $\Theta = 0.66$ and 1.0 ML of S, S₂ and not atomic S is the more stable species on the surface. The most stable configuration of S₂ molecule in systems A and B are above a bridge and a top sites (Fig. 2a). In system C, the molecule is bonded to two neighboring top sites (Fig. 2b). The calculated S-S distance (2.03 – 2.13 Å) is larger in comparison to that found for free S₂ (1.90 Å).

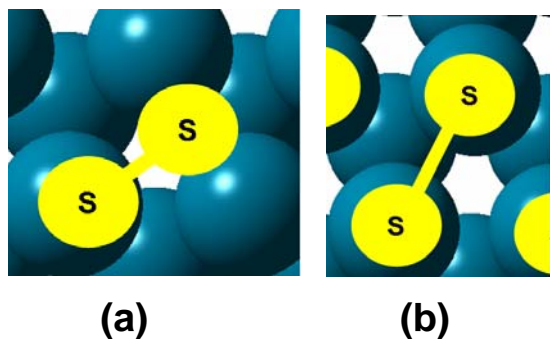


Figure 2. S₂ molecule on (a) (2×2) (0.5 ML S), $(\sqrt{3} \times \sqrt{3})$ (0.66 ML S) and (b) (2×2) (1.0 ML S) Pd(111) slabs.

To gain insight into the nature of bonding in the Pd-S interface, we calculate the change in the work-function change (ΔW) and surface dipole moment ($\Delta \mu$) for all the systems considered here. The work-function W is defined as $W = \Phi(\infty) + E_{N-1} - E_N$. The terms $\Phi(\infty)$, E_{N-1} , and E_N represent the total electrostatic potential far from the surface, ground state energy of a singly ionized crystal, and

ground state energy of a neutral N-electron crystal, respectively. The surface dipole moment, μ , on the other hand, is obtained using the Helmholtz relation.¹⁸ The calculated work-function for the bare Pd(111) surface is 5.34 eV, in good agreement with the experimental value of 5.6 eV. The calculated ΔW and $\Delta \mu$ for all the systems considered here are essentially zero. This result implies the absence of electron transfer from the substrate to the sulfur adlayer. Thus, the bonding in the Pd-S interface is predominantly covalent in nature. This is in contrast with Pd(111)+O system which shows linear increase in ΔW and $\Delta \mu$ with coverage.¹⁹ This implies, that ionic bonding becomes more important for Pd(111)+O with increasing coverage. The result for the Pd(111)+S system may be attributed to the small difference in electronegativity between sulfur and Pd.

Conclusions

The interaction of sulfur with Pd(111) surface was investigated using Density Functional Theory. The stability of the adlayer is presented and the electronic properties of the relaxed structures are analyzed. A complex behavior of the Pd-S interface as a function of coverage was found. At small coverages (0.11 – 0.50 ML), the adsorption of atomic S on the fcc hollow sites is the most stable. There is an attractive interaction between sulfur in the coverage range 0.25-0.33 ML which leads to island formation with a $(\sqrt{3} \times \sqrt{3})$ structure in agreement with experiment. At sulfur coverages above 0.50 ML, S₂ and not atomic S is predicted to be the most stable species on the surface. The change in the calculated work-function and surface dipole moment as a function of coverage is essentially zero. These results imply that the bonding in the Pd-S interface is predominantly covalent in nature.

Acknowledgement. We thank Dan Sorescu and Anthony Cugini for helpful comments. Computations were performed on a computer cluster at the National Energy Technology Laboratory.

References

- (1) Forbes, J. G.; Gellmann, A. J.; Dunphy, J. C.; Salmeron, M.; *Surf. Sci.* **1992**, 279, 68.
- (2) Gentle, T. M.; Muttarties, T. L.; *J. Phys. Chem.* **1983**, 87, 2469.
- (3) Hunka, D. E.; Picciotto, T.; Jaramillo, D. M.; Land, D. P.; *Surf. Sci.* **1999**, 421, L166.
- (4) Shu, J.; Grandjean, B.; Van Neste, A.; Kaliaguine, S.; *Can. J. Chem. Eng.* **1991**, 69, 1036.
- (5) Uemiyu, S.; *Sep. Purif. Methods* **1999**, 28, 51.
- (6) Lee, J.; Rhee, H.; *J. Catal.* **1998**, 177, 208.
- (7) Rodriguez, J. A.; Hrebek, J.; *Acc. Chem. Res.* **1999**, 32, 719.
- (8) Dhanak, V. R.; Shard, A. G.; Cowie, B. C. C.; Santoni, A.; *Surf. Sci.* **1998**, 410, 321.
- (9) Speller, S.; Rauch, T.; Postnikov, A.; Heiland, W.; *Phys. Rev. B* **2000**, 61, 7297.
- (10) Börmann, J.; Huck, M.; Kuntze, J.; Rauch, T.; Speller, S.; Heiland, W.; *Surf. Sci.* **1996**, 357-358, 849.
- (11) Rodriguez, J. A.; Chatuverdi, S.; Sirsak, T.; *Chem. Phys. Lett.* **1998**, 296, 421.
- (12) Kresse, G.; Hafner, J.; *Phys. Rev. B* **1994**, 49, 14251.
- (13) Perdew, J. P.; Wang, Y.; *Phys. Rev. B* **1986**, 33, 8800.
- (14) Vanderbilt, D. H.; *Phys. Rev. B* **1990**, 41, 7892.
- (15) Coles, B. R.; *J. Inst. Metals* **1956**, 84, 346.
- (16) Monkhorst, H. J.; Pack, J. D.; *Phys. Rev. B* **1976**, 13, 5188.
- (17) Graviil, P. A.; Toulhoat, H.; *Surf. Sci.* **1999**, 430, 176.
- (18) Swanson, L. W.; Strayer, R. W.; *J. Chem. Phys.* **1968**, 48, 2421.
- (19) Todorova, M.; Reuter, M.; Scheffler, M.; submitted to *J. Phys. Chem.*

ONSET OF SUBCRITICAL DAMPED OSCILLATIONS IN SMALL SLAB, CYLINDER AND SPHERE DURING WAVE DIFFUSION, REACTION AND RELAXATION

Dr. Kal Renganathan Sharma PE

Formerly Principal, Sakthi Engineering College
Anna University Affiliated, Oragadam
Kancheepuram, Tamil Nadu, India
Email: jyoti_kalpika@yahoo.com

Abstract

The transient concentration profile during simultaneous diffusion, relaxation and reaction using Cattaneo and Vernotte non-Fick hyperbolic damped wave finite speed diffusion and relaxation equation is obtained by the method of separation of variables. For small width of the slab, $a < \pi \sqrt{D\tau_r}/|1 - k^*|$, the transient concentration is found to be subcritical damped oscillatory. An exact well bounded solution is derived for other values of a . For a cylinder, the transient portion of the solution is bifurcated. For small width of the pellet the time domain portion of the solution is subcritical damped oscillatory. This was found for $R < \sqrt{D\tau_r}(4.8096)/|1 - k^*|$. Exact solutions are derived for other values of R as well as for the small values as a infinite Fourier Bessel series. The Fourier series Bessel solution to the Fick's parabolic diffusion equation is found to be augmented by an expression in exponential decay in time. The steady state portion of the solution is given by a expression containing modified Bessel function of the first kind. For a sphere, the solution is presented as a sum of steady state and transient parts. For $R < 2\pi \sqrt{D\tau_r}/|1 - k^*|$, even from the term $n=1$ in the infinite series there is cosinus contribution in the time domain solution.

Introduction

Fick's law of mass diffusion does not fully describe the transient processes. This can become significant during simultaneous fast reaction and diffusion. Physically, there exists a time where the linear mass diffusion relationship is not valid. This is because the Fick's law implicitly assumes an infinite speed of propagation of mass in any media. In reality, mass travels at a large but finite velocity. Maxwell [1] was the first to propose the relaxation concept and used it to predict the Visco elasticity of materials. Cattaneo [2] and Vernotte [3] provided an augmented expression for heat conduction as equation which when combined with the energy balance results in hyperbolic damped wave partial differential equation. By analogy the Cattaneo and Vernotte non-Fick diffusion and relaxation equation can be written as;

$$J = -D\partial C/\partial x - \tau_r \partial J/\partial t \quad (1)$$

The theoretical study of the Cattaneo and Vernotte equation to describe heat conduction and relaxation was reviewed by Osizik and Tzou [4], Joseph and Preziosi [5,6]. Recent Experimental evidence for hyperbolic wave propagative and relaxation heat equation report a relaxation time of the order of 20 – 30 seconds by Mitra, Kumar, Vedavarz and Moellami [7]. Very little work is reported in the implications of wave propagation in diffusion and simultaneous reaction studies. In this study a analytical solution is developed for the hyperbolic wave diffusion and relaxation

problem for different geometries such as the finite slab, cylinder and sphere.

Analysis

Finite Slab at Constant Wall Concentration. Consider a finite slab of width $2a$ with an initial concentration at C_0 . The sides of the slab are maintained at constant concentration C_s . The governing equation can be obtained by eliminating J_x between Eqs. (1) and the equation from mass balance, $-\partial J/\partial x - k''C = \partial C/\partial t$, where k'' is the simple first order reaction rate constant. This is achieved by differentiating Eq.(1) with respect to x and the balance equation with respect to t and eliminating the second cross derivative of J with respect to x and time. Thus,

$$\tau_r \partial^2 C/\partial t^2 + (1 + k^*)\partial C/\partial t + k''C = D \partial^2 C/\partial x^2 \quad (2)$$

$$\text{Let } \tau = t/\tau_r; X = x/\sqrt{D\tau_r}; k^* = (k''\tau_r) \quad (3)$$

The governing equation in the dimensionless form is then ;

$$k^* C + \partial C/\partial \tau (1 + k^*) + \partial^2 C/\partial \tau^2 = \partial^2 C/\partial X^2 \quad (4)$$

The solution can be assumed to consist of a steady state part and a transient part, i.e., $C = C^t + C^{ss}$. The steady state part and boundary conditions can be selected in such a fashion that the transient portion becomes homogeneous.

$$\partial^2 C^{ss}/\partial X^2 = k^* C^{ss} \quad (5)$$

The Boundary Conditions are

$$X = 0, \partial C^{ss}/\partial X = 0 \quad (6)$$

$$X = \pm a/\sqrt{D\tau_r}, C^{ss} = C_s \quad (7)$$

The solution for Eq. (5) can be written in terms of the hyperbolic sine and cosine functions as;

$$C^{ss} = A_1 \sinh((k^*)^{1/2}X) + A_2 \cosh((k^*)^{1/2}X) \quad (8)$$

Applying the boundary condition given in Eq. (6) it can be seen that $A_1 = 0$. Solving for A_2 from Eq. (8).

$$C^{ss}/C_s = \cosh((k^*)^{1/2}X) / \cosh((k^*)^{1/2}X_a) \quad (9)$$

The equation and time and space conditions for the transient portion of the solution can be written as;

$$\partial^2 C^t/\partial \tau^2 + (1 + k^*)\partial C^t/\partial \tau + k''C^t = D \partial^2 C^t/\partial X^2 \quad (10)$$

$$\text{Initial Condition : } \tau = 0, C^t = C_0$$

$$\text{Final Condition: } \tau = \infty, C^t = 0 \quad (12)$$

The Boundary Conditions are now homogeneous after the expression of the result as a sum of steady state and transient parts and are;

$$\partial C^t/\partial X = 0, X = 0 \quad (13)$$

$$X = X_a, C^t = 0 \quad (14)$$

The solution is obtained by the method of separation of variables. Initially the damping term is eliminated using a

substitution such as $C^t = W \exp(-n\tau)$. Eq. (10) then becomes at $n = 1/2 (1 + k^*)$

$$W_{xx} = -(1 - k^*)^2 W/4 + W_{\tau\tau} \quad (15)$$

Eq. (15) can be solved by the method of separation of variables.

$$\text{Let } W = g(\tau) \phi(X) \quad (16)$$

Eq. (15) becomes,

$$g(\tau) \phi''(X) = -(1 - k^*)^2 g(\tau) \phi(X)/4 + g''(\tau) \phi(X) \quad (17)$$

$$\text{Or } \phi''(X)/\phi(X) = -(1 - k^*)^2/4 + g''(\tau)/g(\tau) = -\lambda_n^2 \quad (18)$$

The space domain solution is;

$$\phi(X) = c_1 \sin(\lambda_n X) + c_2 \cos(\lambda_n X) \quad (19)$$

From the boundary conditions,

$$\text{At } X = 0, \partial\phi/\partial X = 0, \text{ it can be seen that } c_1 = 0 \quad (20)$$

$$\phi(X) = c_1 \cos(\lambda_n X) \quad (21)$$

From the boundary Condition given by Eq. (13),

$$0 = c_1 \cos(\lambda_n X_a) \quad (22)$$

$$(n + 1/2)\pi = \lambda_n X_a$$

$$\lambda_n = (n + 1/2)\pi \sqrt{D\tau_r}/a, \quad n = 0, 1, 2, 3, \dots \quad (23)$$

The time domain solution would be,

$$g = c_3 \exp(\sqrt{-(1 - k^*)^2/4 - \lambda_n^2} \tau) + c_4 \exp(-\sqrt{-(1 - k^*)^2/4 - \lambda_n^2} \tau) \quad (24)$$

From the FINAL condition given by Eq.(12), not only the transient concentration has to decay out to 0 but also the wave concentration. As, $W = C^t \exp(\tau/2)$, at time infinity the transient concentration is zero and as any number multiplied by zero is zero even if it is infinity, $W = 0$ at the final condition. Applying this condition in the solution Eq.(24) it can be seen that $c_3 = 0$. Thus,

$$C^t = \sum_{n=0}^{\infty} C_0 2(-1)^n / (n + 1/2)\pi \exp(-\tau/2) \exp(-\sqrt{-(1 - k^*)^2/4 - \lambda_n^2} \tau) \cos(\lambda_n X) \quad (25)$$

λ_n is described by Eq. (23). C_n can be derived using the orthogonality property and can be shown to be $C_0 2(-1)^n / (n + 1/2)\pi$. It can be seen that the model solutions given by Eq. (25) is bifurcated, i.e., the characteristics of the function change considerably when a parameter such as the width of the slab is varied. Here a decaying exponential becomes exponentially damped cosinus. This is referred to as subcritical damped oscillatory behavior. For $a < \pi \sqrt{D\tau_r} / (1 - k^*)$ even for $n=1$, all the terms in the infinite series will pulsate. This when the argument within the square root sign in the exponentiated time domain expression becomes negative and the result becomes imaginary. Using Demovrie's theorem and taking real part for small width of the slab,

$$C^t = \sum_{n=0}^{\infty} c_n \exp(-\tau/2) \cos(\sqrt{(\lambda_n^2 - (1 - k^*)^2/4)\tau}) \cos(\lambda_n X) \quad (26)$$

Finite Cylinder at Constant Wall Concentration. Consider a finite cylinder of radius R with a initial concentration of C_0 . The sides of the cylinder are maintained at a finite concentration of C_s . The governing equation from mass balance which is, $(-1/r \partial(rJ)/\partial r - k^* C = \partial C/\partial t)$ is achieved by differentiating Eq.(1) with respect to r and the balance equation with respect to t and eliminating the second cross derivative of J with respect to r and time. Then the equation is non-dimensionalized to give;

$$\partial^2 C/\partial \tau^2 + (1 + k^*) \partial C/\partial \tau + k^* C = (\partial^2 C/\partial X^2 + 1/X \partial C/\partial X) \quad (27)$$

$$\text{where } \tau = t/\tau_r; \quad X = r/\sqrt{D\tau_r}; \quad k^* = k^* \tau_r \quad (28)$$

The initial condition

$$\tau = 0, \quad \forall r, \quad C = C_0 \quad (29)$$

$$\tau > 0, \quad X = 0, \quad \partial C/\partial X = 0 \quad (30)$$

$$\tau > 0, \quad X = R/\sqrt{D\tau_r}, \quad C = C_s \quad (31)$$

The solution can be expressed as a sum of a steady state part and a transient part. i.e., $C = C^{ss} + C^t$.

The steady state part is given by;

$$k^* C^{ss} = (\partial^2 C^{ss}/\partial X^2 + 1/X \partial C^{ss}/\partial X) \quad (32)$$

This can be recognized as a modified Bessel differential equation of the zeroth order;

$$C^{ss}/C_s = I_0(k^{*1/2} X) / I_0(k^{*1/2} X_s) \quad (33)$$

The transient portion of the concentration is governed by;

$$\partial^2 C^t/\partial \tau^2 + (1 + k^*) \partial C^t/\partial \tau + k^* C^t = (\partial^2 C^t/\partial X^2 + 1/X \partial C^t/\partial X) \quad (34)$$

The solution is obtained by the method of separation of variables. Initially the damping term is removed using a $C^t = W \exp(-n\tau)$ substitution. Eq. (34) becomes at $n = (1 + k^*)/2$

$$W_{xx} + W_X/X = W(- (1 - k^*)^2/4) + W_{\tau\tau} \quad (35)$$

The solution to equation (35) is obtained by the method of separation of variables.

$$\text{Let } W = g(\tau) \phi(X) \quad (36)$$

$$\text{Then, } (\phi'' + \phi'/X)/\phi = g''/g - (1 - k^*)^2/4 = -\lambda_n^2 \quad (37)$$

$$\text{Or } X^2 \phi'' + X \phi' + X^2 \lambda_n^2 \phi = 0 \quad (38)$$

This can be recognized as the Bessel equation:

$$V = c_1 J_0(\lambda_n X) \quad (39)$$

c_2 can be seen to be zero as ϕ is finite at $X = 0$ from boundary condition given by Eq. (30). From the boundary condition given by equation (31) with the non-homogeneity attributed to the steady state portion of the solution;

$$C^t = 0 = c_1 J_0(\lambda_n R/\sqrt{D\tau_r}) \quad (40)$$

$$\text{or } \lambda_n = \sqrt{D\tau_r}/R(2.4048 + (n-1)\pi), \quad \text{where } n = 1, 2, 3, \dots \quad (41)$$

$$\text{Now, } \phi''/\phi = (1 - k^*)^2/4 - \lambda_n^2 \quad (42)$$

or

$$\phi = A \exp(-\sqrt{(1-k^*)^2/4 - \lambda_n^2} \tau) + B \exp(+\sqrt{(1-k^*)^2/4 - \lambda_n^2} \tau) \quad (43)$$

B can be seen to be zero as the system decays to steady state. $W = C^t \exp(1+k^*)\tau/2$. At infinite time the value of the transient concentration is zero and the product of 0 and infinity, is zero and hence W is zero and so B has to be set to 0.

$$\text{For } |1 - k^*/2| < \lambda_n \quad (44)$$

$$\text{Or } R < \sqrt{(D \tau_r)} (4.8096)/|1 - k^*| \quad (45)$$

When equation (44) is satisfied the solution in time domain becomes periodic. Thus the general solution is bifurcated depending on the value of R with respect to the binary diffusivity and relaxation time.

$$C^t = \sum_{l=0}^{\infty} A_n \exp(-1/2 - \sqrt{(1-k^*)^2/4 - \lambda_n^2} \tau) J_0(\lambda_n X) \quad (46)$$

Where A_n can be obtained from the principle of orthogonality and the initial condition

$$A_n = C_0 \int_0^{X_R} J_0(\lambda_n X) dX / \int_0^{X_R} J_0^2(\lambda_n X) dX \quad (47)$$

The nature of Eq. (46) is bifurcated. For values of $R < \sqrt{(D \tau_r)} (4.8096)/|1 - k^*|$.

$$C^t = C_0 \sum_{l=0}^{\infty} A_n \exp(-1/2 \tau) \cos(\sqrt{(\lambda_n^2 - (1-k^*)^2/4)} \tau) J_0(\lambda_n X) \quad (48)$$

where A_n is given by equation (47) and λ_n given by equation (41).

Finite Sphere with Constant Wall Concentration. Consider a finite sphere of radius R with a initial concentration of C_0 . The sides of the sphere are maintained at a finite concentration of C_s . The governing mass balance equation from mass balance and the constitutive relation for wave diffusion and relaxation which can be written after non-dimensionalization as;

$$X^2 \partial^2 C / \partial X^2 + 2X \partial C / \partial X - k^* C = \partial^2 C / \partial \tau^2 + (1+k^*) \partial C / \partial \tau \quad (49)$$

$$\text{Where, } \tau = t/\tau_r; X = r/\sqrt{(D \tau_r)}; k^* = (k'''\tau_r) \quad (50)$$

The four conditions in space and time are;

$$\tau = 0, \forall r, C = C_0 \quad (51)$$

$$\tau > 0, X = 0, \partial C / \partial X = 0 \quad (52)$$

$$\tau > 0, X = R/\sqrt{(D \tau_r)}, C = C_s \quad (53)$$

$$\tau \rightarrow \infty, C = C_s \quad (54)$$

The solution to the concentration can be expressed as a sum of a transient portion and a steady state portion in order to ensure that the transient boundary values are homogeneous.

$$\text{Let, } C = C^t + C^{ss}$$

The steady state part and boundary conditions can be selected in such a fashion that the transient portion becomes homogeneous.

The steady state portion of the concentration and the boundary Conditions are;

$$X^2 \partial^2 C^{ss} / \partial X^2 + 2X \partial C^{ss} / \partial X - k^* C^{ss} = 0 \quad (55)$$

$$X = 0, \partial C^{ss} / \partial X = 0 \quad (56)$$

$$X = R/\sqrt{(D \tau_r)}, C^{ss} = C_s \quad (57)$$

Eq. (55) can be recognized as a Bessel differential equation. The solution is;

$$C^{ss} = c_1 I_{1/2}(X k^{*1/2})/X^{1/2} + c_2 I_{-1/2}(X k^{*1/2})/X^{1/2} \quad (58)$$

Since the concentration is finite at $X = 0$, c_2 is set to zero. Solving for c_1 from the boundary condition given in Eq.(57) the solution at steady state is;

$$C^{ss}/C_s = X_R^{1/2} I_{1/2}(X k^{*1/2}) / I_{1/2}(X_R k^{*1/2}) X^{1/2} \quad (59)$$

The solution of the transient part is the rest of the problem:

$$(1+k^*) \partial C^t / \partial \tau + \partial^2 C^t / \partial \tau^2 + k^* C^t = \partial^2 C^t / \partial X^2 + 2/X \partial C^t / \partial X \quad (60)$$

The four conditions become;

$$\text{Initial Condition : } C^t = C_0 \quad (61)$$

$$\text{Final Condition : } C^t = 0 \quad (62)$$

$$X = 0, C^t = \text{finite} \quad (63)$$

$$X = X_R, C^t = 0 \quad (64)$$

The solution is obtained by the method of separation of variables. Initially the damping term is removed using a $C^t = W \exp(-n\tau)$ substitution. Eq. (60) becomes at $n = (1+k^*)/2$

$$W_{xx} + 2W_x/X = W(- (1-k^*)^2/4) + W_{\tau\tau} \quad (65)$$

The solution to equation (65) can be obtained by the method of separation of variables.

$$\text{Let } W = g(\tau) \phi(X) \quad (66)$$

$$\text{Then, } (\phi'' + 2\phi'/X)/\phi = g''/g - |1 - k^*|^2/4 = -\lambda_n^2 \quad (67)$$

$$\text{Or } X^2 \phi'' + 2X \phi' + X^2 \lambda_n^2 \phi = 0 \quad (68)$$

This can be recognized as the Bessel equation of the 1/2th order:

$$V = c_1 X^{-1/2} J_{1/2}(\lambda_n X) \quad (69)$$

c_2 can be seen to be zero as ϕ is finite at $X = 0$ from boundary condition given in Eq. (63).

$$0 = c_1 J_{1/2}(\lambda_n R/\sqrt{(D \tau_r)})/X^{1/2} \quad (70)$$

$$\text{or } \lambda_n = n\pi \sqrt{(D \tau_r)}/R \quad \text{where } n = 0, 1, 2, 3, \dots \quad (71)$$

$$\text{Now, } \phi''/\phi = |1 - k^*|^2/4 - \lambda_n^2 \quad (72)$$

$$\text{or } \phi = A \exp(-\sqrt{(1-k^*)^2/4 - \lambda_n^2} \tau) + B \exp(\sqrt{(1-k^*)^2/4 - \lambda_n^2} \tau) \quad (73)$$

B can be seen to be zero as the system decays to steady state from the FINAL condition given in equation (54). $W = u \exp(1+k^*)\tau/2$. At infinite time the value of u is zero and the

product of 0 and infinity, is zero and hence W is zero and so B has to be set to 0.

$$C^t = \sum_{n=0}^{\infty} A_n \exp(-(1+k^*)/2 - \sqrt{((1-k^*)^2/4 - \lambda_n^2)}\tau) J_{1/2}(\lambda_n X)/X^{1/2} \quad (74)$$

Where A_n can be obtained from the principle of orthogonality at the initial condition.

$$C_0 = \sum_{n=0}^{\infty} A_n J_{1/2}(\lambda_n X)/\sqrt{X} \quad (75)$$

Multiplying both sides of the equation by $J_{1/2}(\lambda_m X)$ and integrating between the limits of 0 and $R/\sqrt{D\tau_r}$ and using the principle of orthogonality;

$$A_n = (C_0) \int_0^{XR} J_{1/2}(\lambda_n X)/\sqrt{X} dX / \int_0^{XR} J_{1/2}^2(\lambda_n X)/\sqrt{X} dX \quad (76)$$

For terms in the infinite series where the $(\lambda_n > |1 - k^*|/2)$ the exponentiated time domain terms become negative within the square root and using the De Moivre's theorem the real part gives the $\cos((\lambda_n^2 - (|1 - k^*|)^2/4)^{1/2}\tau)$.

Nomenclature

a	width (m)
C	concentration (mole/cu.m)
D	diffusivity (sq.m/s)
J	mass flux (mole/sq.m/s)
$k^{''}$	first order reaction rate constant (sec ⁻¹)
k^*	$(k^{''}\tau_r)$
τ	t/τ_r
X	$x/\sqrt{D\tau_r}$
τ_r	Relaxation Time (s)

Subscript

0	initial
i	integration constant i, i = 1,2,3,4.
k	indice.
r	relaxation time
s	surface

Superscript

ss	steady state
t	transient state

References

1. I.C. Maxwell, A Treatise On Electricity And Magnetism, Oxford University Press, UK, (1873).
2. C. Cattaneo, Comptes Rendus, **247**, 431 (1958).
3. P. Vernotte, Les paradoxes de la theorie continue de l'equation de la chaleur, C. R. Hebd. Seanc. Acad. Sci. Paris, **246**, 22, 3154 (1958).
4. M. N. Ozisik and D. Y. Tzou, ASME Journal of Heat Transfer, **116**, 526 (1994).
5. D. D. Joseph and L. Preziosi, Reviews of Modern Physics, **61**, 41 (1989).
6. D. D. Joseph and L. Preziosi, Reviews of Modern Physics, **62**, 375 (1989).
7. K. Mitra, S. Kumar, A. Vedavarz, A and M. K. Moallemi, ASME Journal Of Heat Transfer, **117**, 568 (1995).